Control of Electrons through Patterning of Superstructures in Sodium Cobaltate

Daniel Graham Porter

Royal Holloway College
University of London

A dissertation submitted to the University of London
for the degree of Doctor of Philosophy

May 2012

Declaration of Authorship

I Daniel Graham Porter hereby declare that this thesis and the work presented in it is entirely my own. Where I have consulted the work of others, this is always clearly stated.

Signed: ____________________

Date: ____________________

Abstract

Sodium Cobaltate (Na_xCoO_2) has emerged as a material of exceptional scientific and technological interest since it is among the best P-type thermoelectric materials. The superstructures in pure Na_xCoO_2 templates the Coulomb landscape on the Co layers and is found to control the physical properties. The combination of the high electrical conductivity in the Co layers with the low thermal conductivity due to the rattling of sodium ions in cages, are the precise conditions for thermoelectric materials with high figures of merit. Replacing Na by divalent ions was reported to lead to a dramatic improvement in thermoelectric performance. The superstructures of $Na_xCa_yCoO_2$ and $Na_xSr_yCoO_2$ have been determined by Laue diffraction using neutrons on SXD at ISIS and x-rays at Royal Holloway. Reverse Monte-Carlo methods were used to determine Na ion patterning including the locations of the divalent ions. Co and O displacements were also determined that show buckling following the Na structure. In the doped systems we find completely new multi-vacancy clusters. Di-vacancies form in Ca doped systems where the divalent ion sits at the central site. In the Sr doped systems two new superlattices are observed, explained by the clustering of separated Sr ions with associated vacancies. Multiple valence states have been detected by NMR, which is a local probe, but spatial charge ordering in the cobalt layer has not previously been observed. We report new measurements using Resonant X-ray Scattering on the Materials and Magnetism beamline I16 at Diamond. We find resonant x-ray scattering with the same periodicity as the sodium superstructure, directly demonstrating that the electronic ordering in these cobalt layers is controlled by the sodium ordering. We are able to reproduce the energy, polarisation and azimuthal dependencies of the resonant x-ray scattering in calculations using the FDMNES code.

Acknowledgments

Well, it's been a frantic three and a half years (a little over now!) but the end is in sight and the mountain that is the PhD is almost defeated.

My time as PhD student has taken me all over Europe and has shown me the true extent of experimental condensed matter physics - with all its highs and lows, trials and tribulations. My guide through this wonderful world has been my supervisor, Jon Goff, who has guided me along this rocky road of research with so much patience and insight, and even a few nice dance moves at my wedding. My thanks also goes to Michel Roger, whose brilliant ideas and advice have helped me in almost every aspect of my research.

In order to do any of this research, we had to have the best crystals of Sodium Cobaltate ever grown. And we had them thanks to Sivaperumal Uthayakumar, or Uthay from Royal Holloway and Prabhakaran Dharmalingam from Oxford. I have always said that growing crystals seems like black magic to me, but this is just my way of acknowledging the incredible amount of effort and patience that goes into making our crystals.

I am very lucky to have had a lot of beam time at the large neutron and x-ray facilities, but without the help of the instrument scientists, we would still be looking for our first Bragg peak! At ISIS, Matthias Gutmann helped us tirelessly during SXD experiments, and at the ILL, Mechthild Enderle guided us expertly on IN20. In the ever winding pathways of Diamond Light Source, the I16 team of Steve Collins, Carlo Vecchini and Gareth Nisbet slogged away at our samples with us through all the long nights. Likewise, Raymond Fan kept a cool head when everything got confusing at Diamond.

Back at Royal Holloway, I would like to thank the other PhD students in the group; Manoj, Giovanni and David who all kept me on my toes and provided much entertainment when I had to explain how structural refinements work for the um-teenth time! I would also like to thank the undergraduate summer students, Francesca and Andre, who both managed to make a good impact in only a few weeks.

I certainly could not have gotten this far without the traditional 3pm tea time with Chris. I may have only rarely beaten him at cylindrical chess and 3D Connect-4, but I do owe my thanks to him for instructing me on the use of the PPMS, as well as most other basic physics.

Finally I would like to add a huge thanks to my wife Susan, who has tirelessly (but not always quietly) put up with my experiments, my time out of the country and all the little quirks I've started acquiring like a good physicist. I would certainly never have gotten here today though without the love and support from my parents and family. Everything I do, I do to make you all proud.

Contents

List of Figures

List of Tables

Chapter 1

Background

A corner stone of modern scientific investigation is the hunt for novel materials that could be scientifically interesting and technologically important. The discovery of the high temperature superconductor $YBa_2Cu_3O_{7-x}$, also called ‘YBCO’, in 1986 [1] and its use in medical imaging applications is such an example of an important scientific discovery in material properties that can have a profound effect on society. As well as slowly increasing superconducting transition temperatures, these new materials have exhibited a vast range of other interesting phenomena, such as complex magnetic states and metal-insulator transitions. Some ‘wonder’ materials gave remarkable enhancement of their various properties, which can be of outstanding technological value, allowing for faster and more advanced computers, or more efficient and environmentally friendly devices. Multiferroic materials combine multiple types of long range order such as antiferromagnetism and ferroelectricity in $BiFeO_3$ and can be used to produce environmentally friendly piezoelectric devices or to increase the storage space in hard drives [2, 3]. The spintronic manganite materials exhibit an effect called colossal magnetoresistance, where the resistivity of the material can be radically altered in the presence of a magnetic field. These materials have found uses in controlling advanced electronic devices and have been an important ingredient for the rapidly developing technology of the past few decades [4].

In order to further this trend of material and phenomena discovery, we must understand how these materials work and why it is that they can show such remarkable behaviour. Central to this understanding is the behaviour of electrons within these materials, where, unlike simple metals, their interactions are strong due to the complex atomic and electronic structures created.

Sodium Cobaltate, Na_xCoO_2, is such a material, exhibiting a range of different phenomena as the concentration of sodium, x, is varied [5, 6, 7, 8]. This system was initially studied due to its similarity to the cuprate high-temperature superconductors. It was initially found to exhibit superconductivity itself when hydrated [5], although the transition temperature of 4K was never enhanced. As the concentration of sodium is varied, a number of different phenomena can be observed, including superconductivity, a metal-insulator transition and a spin-density wave region [6, 9, 10], as illustrated in figure 1.1. The most technologically important property however, is the material's large thermopower, which is amongst the highest observed and much greater than in traditional semiconductor materials [11, 7]. This makes it an ideal candidate for devices that can harvest energy from waste heat, or efficiently cool microprocessors. This combination of features makes Sodium Cobaltate an ideal material to study, in order to enhance our fundamental understanding of complex materials and develop future technologies.

To further understand this material, neutron and x-ray scattering techniques will be combined with physical properties measurements and computational modelling to study its atomic, electronic and magnetic structures. By doping the material with divalent ions, we will observe the effects of doping on these structures and on the properties of the system, so that we might learn how to enhance the material properties further.

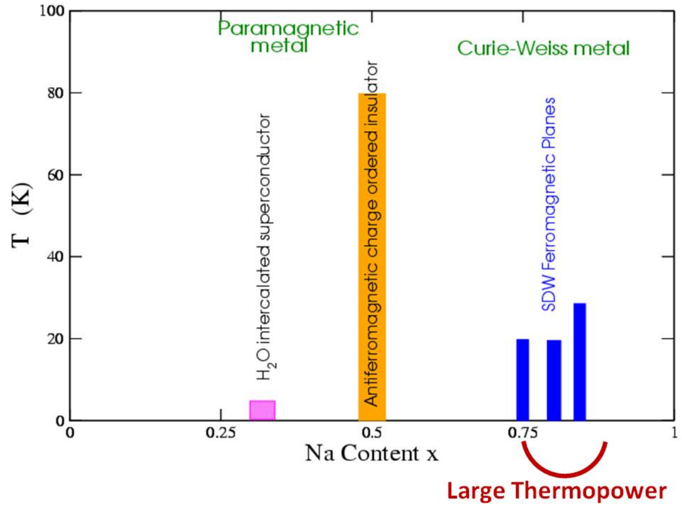

Figure 1.1: The phase diagram of Na_xCoO_2. From figure 2, ref. [6]

1.1 Thermopower

The thermoelectric effect allows the conversion between a temperature difference and an electric voltage, allowing waste heat to be converted to useful electrical energy. Alternatively a voltage can be applied that will cause a temperature difference allowing the creation of an efficient solid state cooling device. The conversion of temperature differences directly into electricity is named the Seebeck effect and can be characterised by the Seebeck coefficient, or thermopower, S:

$$S = -\frac{\Delta V}{\Delta T} \tag{1.1}$$

Conversely, generating heat or cooling by using an electrical potential is called the Peltier effect. These effects can be understood in simple materials by the diffusion of charge carriers across a temperature gradient, as illustrated in figure 1.2. As a temperature difference is established across a material, the electrons (or holes) move faster in the hot region and slower in the cold region. This leads to diffusion of the charge carriers from the hot region to the cold region, whereby a build up of charge will occur, creating a potential difference. In most metals, this effect is countered by thermal excitations, or phonons moving against the thermal gradient, reducing the effect. A good thermoelectric material must have high electrical conductivity to allow the charge carriers to diffuse, but low thermal conductivity so that phonons cannot dissipate the temperature difference.

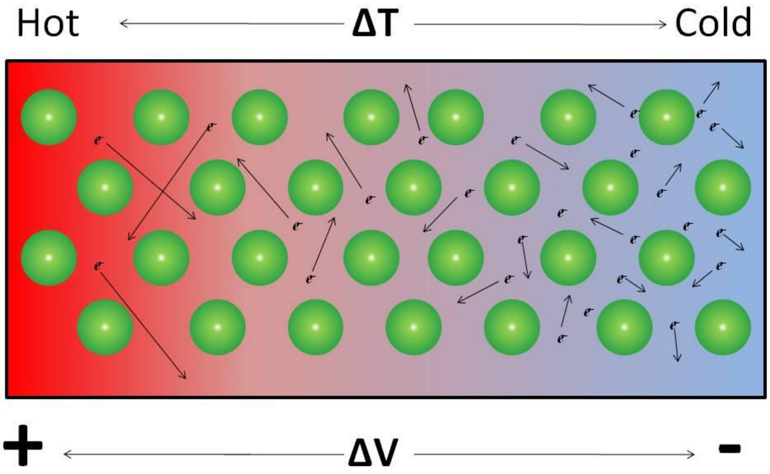

Figure 1.2: The Thermoelectric effect. Electrons move faster in the high temperature region leading to diffusion of charge from the high temperature to the low temperature region, building a potential difference in doing so.

1.1.1 Thermoelectric Performance

The efficiency of operation of a thermoelectric device is usually measured by its 'figure of merit' $ZT = \frac{\sigma T S^2}{\kappa}$, a dimensionless number proportional to the square of the Seebeck coefficient, S and to the ratio (σ/κ) of the electrical to thermal conductivities.

For power generation, the maximum efficiency is:

$$\eta = \eta_c \frac{[(ZT_m + 1)^{\frac{1}{2}} - 1]}{[(ZT_m + 1)^{\frac{1}{2}} + T_C/T_H]} \tag{1.2}$$

where T_C and T_H are the cold and hot source temperatures with mean value T_m, and $\eta_c = (1 - T_C/T_H)$ is the Carnot efficiency. The efficiency reaches its limiting value η_c at large ZT [12].

For Peltier cooling, the maximum heat flux pumping power of a thermoelectric material of thickness l is:

$$Q_{max} = \left[\frac{1}{2}\sigma S^2 T_C^2 - \kappa(T_H - T_C)\right]/l \tag{1.3}$$

which implies maximisation of the 'Power factor', $PF = S^2\sigma$ and minimisation of κ. The maximum achievable temperature difference is:

$$\Delta T = (T_H - T_C) = (ZT_C)(\frac{T_C}{2}) \tag{1.4}$$

therefore, both the power factor, PF, and the figure of merit, ZT, must be optimised.

The thermal conductivity is the sum of an electric and a lattice contribution ($\kappa = \kappa_{el} + \kappa_{ph}$). When κ_{el} is dominant, the ratio (σ/κ) is a constant, which is the so-called Wiedemann-Franz law and holds for many simple materials.

For ordinary metals, S is only a few $\mu V/K$ and ZT is of order 10^{-4} at room temperature, making them useless for applications. Instead, semiconductors are traditionally employed in thermoelectric devices due to their relatively large $S \approx 100\mu V/K$. The state-of-the-art for semiconductor thermoelectrics with heavy elements is a maximum $ZT \approx 1$. However, if we avoid materials that are extremely scarce or contain poisonous elements, the performance of oxides is already close to that of the only abundant, harmless Si_xGe_{1-x} doped semiconductor. A modest enhancement of ZT for oxides would create huge potential for ecologically friendly applications for cooling and energy harvesting.

1.1.2 Strong Correlations

Let us consider the effect of strong correlations on the Seebeck coefficient, S. For an interacting Fermi liquid, linear response theory and the Boltzmann equation give [13]:

$$S = \frac{\pi^2}{3}\frac{k_B^2 T}{e}\left[\frac{\delta \ln \sigma(\epsilon)}{\delta \epsilon}\right]_{\epsilon=\epsilon_f} \tag{1.5}$$

where the energy-dependent conductivity, $\sigma(\epsilon)$, means the electrical conductivity which one would calculate if the Fermi energy ϵ_f, of the metal were ϵ. An approximate expression for $\sigma(\epsilon)$ is given by:

$$\sigma(\epsilon) = \frac{e^2 \lambda A}{12\pi^3 \hbar} \tag{1.6}$$

where λ is the electron mean free path and A is the Fermi surface area. We therefore deduce the relation:

$$\frac{\delta \ln \sigma(\epsilon)}{\delta \epsilon} = \frac{\delta \ln \lambda(\epsilon)}{\delta \epsilon} + \frac{\delta \ln A(\epsilon)}{\delta \epsilon} \tag{1.7}$$

In a 3D isotropic Fermi liquid, A is directly proportional to ϵ. Hence the contribution to S from the second term in the equation above is:

$$S_A = \frac{\pi^2}{3}\frac{k_B^2 T}{e}\left(\frac{1}{\epsilon_f}\right) \tag{1.8}$$

and since

$$\epsilon_f = \frac{\hbar^2}{2m^*}(3\pi^2 n)^{\frac{2}{3}} \tag{1.9}$$

the contribution to the second term S_A is directly proportional to the electron's effective mass m^*. Hence, for a strongly correlated thermoelectric, increasing the correlations and therefore m^* is a means to increase S. Since ZT depends on S^2, increasing the correlations is potentially a very sensitive way to improve thermoelectric performance.

1.2 Crystals & Crystallography

1.2.1 What is a crystal?

All materials on Earth can be classified by their chemical composition and basic atomic structure. One particular class is of real importance to physics, where the atoms making up the material are ordered in repeating patterns similar to a three dimensional wall paper, these materials are known as crystals. Any crystal material can be explained by a repeating pattern of identical units. A single unit, called the crystal basis, involves a unit cell of atoms sitting in a particular arrangement, where any arrangement can be chosen as long as it repeats itself symmetrically throughout the crystal. The basis repeats in all directions, sitting on every point of a crystal lattice, which is a series of points in space. The combination of the basis at every point on the lattice makes a crystal when the number of lattice points essentially becomes infinite (the basis containing only a few atoms compared to the vast number in a typical crystal) [14, 15].

The composition and arrangement of atoms or ions within the basis controls all of the important fundamental properties of the material, especially its electronic and magnetic properties. This is because the location of atoms determines the interactions of electrons within the material, defining the electron band structure that controls electronic, optical and thermal properties. For this reason it is very important to fully understand the arrangement of atoms within the crystal basis, as without this information, an understanding of complex material phenomena such as superconductivity or the thermoelectric effect would be futile.

Many materials, especially metals, have very simple crystal structures whereby atoms simply attempt to sit as close to their neighbours as possible. Such structures are defined by a simple stacking sequence for packing hard spheres, where the first two dimensional layer of closely packed atoms A has a second layer B of atoms sitting in the gaps of the first layer. The third layer then has a choice, being able to sit either above the atoms of layer A or in the second set of gaps not above other atoms. This gives two different types of stacking for simple crystals, either ABA or ABC, where in each case the stacking sequence is repeated indefinitely. A visual explanation of this stacking is given in figure 1.3.

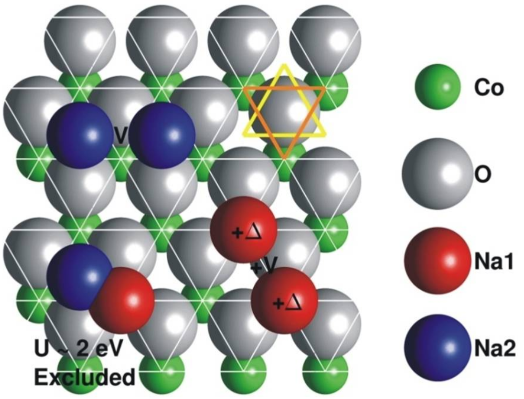

Figure 1.3: Atomic stacking of hard spheres. Co atoms sit at site A, O atoms at site B, in the third stacking step, two sites are possible for stacking, A or C, however in the case of Na_xCoO_2, it is more energetically favourable to sit at position C.

Sodium Cobaltate is not quite so simple however, due to the combination of different types of atom. The basis of Sodium Cobaltate (and its compounds) is made up of sheets of cobalt, where each sheet is covered above and below by layers of oxygen, which sit at opposing locations so that an oxygen ion above the cobalt sheet is not above an oxygen ion below. These cobalt-oxygen layers are separated by 3.4Å, allowing a sheet of sodium with atomic radius 1.9Å to sit between successive layers. The sodium ions cannot sit directly above oxygen and indeed it is energetically unfavourable to sit above cobalt, therefore sodium occupies the C position which is the same positions as the oxygen ions below the cobalt sheet. The unit cell contains two instances of cobalt-oxygen layers and intercalated sodium sheets, where the second instance is a reflection of the first. This gives Sodium Cobaltate the stacking sequence ABCBACBC, where the cobalt sheet is layer A, as described in figure 1.4.

1.2.2 Crystallographic Notation

Crystallography is the science of the arrangement of atoms in crystals and makes use primarily of diffraction techniques. The International Tables of Crystallography [16] is a compendium of much of the knowledge in this field and sets out a rigorous methodology for the study of crystals and the determination of the atomic structures that make them. In crystallography, crystal structures are defined by their fundamental symmetry, which identifies symmetry operations that leave the basis unchanged, including translation (which is fundamental to all crystal systems and defines the lattice), rotation, reflection, glide planes and screw axes. A glide plane is the translation of a reflection in a plane and a screw axis defines an axis in which atomic positions can be rotated about or translated along to remain identical. The mathematical understanding of these basic symmetries lead to a number of constraints on the arrangements of atoms in crystals. For instance the unit cell that defines the shape of the basis can only be one of 14 symmetrical shapes, called Bravais lattices. The atoms must arrange themselves within these unit cells in particular ways, leading to the 230 space groups that define all possible types of ordering in crystal systems [17]. The structure of pure Sodium Cobaltate is given in the international tables notation in the table 1.1. The structure is defined by the space group $P6_3/mmc$ (No. 194 in the international tables of crystallography). This notation, called the HermannMauguin notation, defines the main symmetries of the structure, where P describes a primitive lattice, $6_3/m$ is a 6-fold screw axis and mirror plane along the c-direction, m is a mirror plane in the a-direction and c is a glide plane involving the c-direction and the a-b directions.

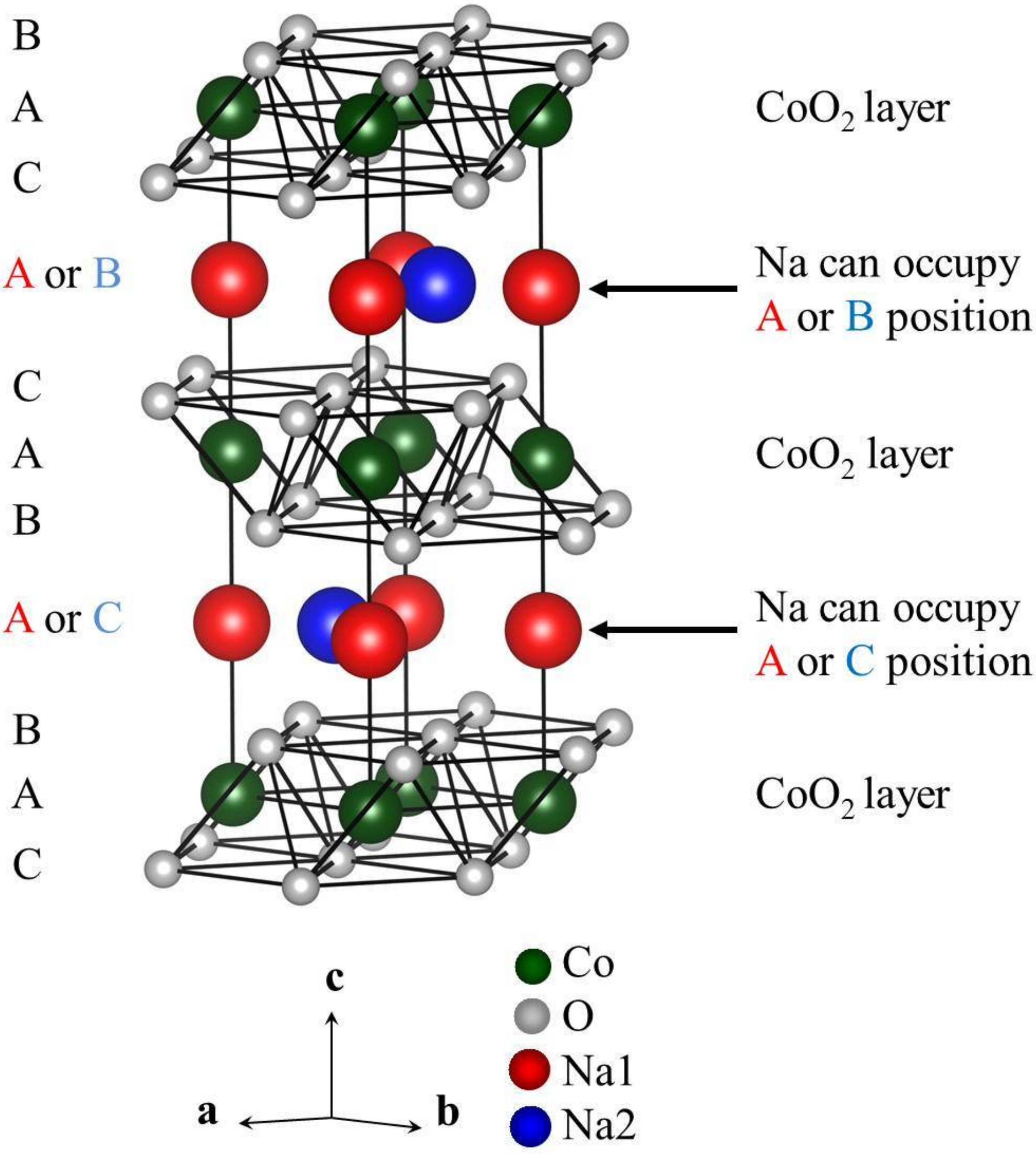

Figure 1.4: Na_xCoO_2 Crystal Structure

Atom	Position			Site
Co	0	0	0	2a
O	1/3	2/3	0.0908	4f
Na1	0	0	1/4	2b
Na2	2/3	1/3	1/4	2d

Table 1.1: Crystal structure of Na_xCoO_2. Position coordinates are given as fractional values along the $\underline{a}$, $\underline{b}$ and $\underline{c}$ directions. The site labels show the Wyckoff positions for this space group, defining the symmetry and number of positions in each site.

1.3 Basic Electronic Structure

Since the discovery of the electron and the subsequent understanding of the basic structure of atoms, physicists have attempted to understand the behaviour of electrons in materials in order to explain their differences in properties, such as why some materials conduct but others are insulating and more recently to explain emergent phenomena such as conventional or unconventional superconductivity [18].

Electrons surround a positive atomic nucleus in quantum mechanical wavestates at different energies, or orbitals, which are defined by 4 quantum numbers: n (energy, integer number from 1), l (angular momentum, from 1 to n and denoted as s,p,d,f), m (angular momentum direction, from -l to l) and s (spin, ± 1). Electrons occupy these orbitals, from lowest energy first, according to the Pauli exclusion principle, which states that no two electrons in the same atom can have the same 4 quantum numbers. For instance, in neutral cobalt the configuration of orbitals is:

$$Co^{27} : 1s^2 2s^2 2p^6 3s^2 3p^6 3d^9$$

Different orbitals occupy different regions of space around the atom and in different shapes. This leads to different orbitals possessing different bonding and interaction characteristics for the atom. The d orbitals that are unfilled in transition metals such as cobalt have been found to play important roles in complex materials

[19]. In Na_xCoO_2, cobalt exists as Co^{3+} or Co^{4+} depending on the concentration of sodium ions, where electrons have been removed from the $3d$ orbital [7, 20]. Co^{3+} is insulating because all the electrons in this shell are paired, however Co^{4+} has an unpaired electron and is magnetic. The locations and interactions of these magnetic atoms within Na_xCoO_2 will determine the electronic properties of the material.

Chapter 2

Experimental Techniques

2.1 Diffraction

Observing the basis of a crystal and therefore its crystal structure is a problem that would become very difficult if it were not for phenomenon of diffraction, caused by the interference of scattered radiation from atomically separated atoms. X-ray diffraction first showed that electromagnetic radiation would diffract through the gaps between planes of atoms in simple materials, and that the diffraction pattern attained could be used to study and determine the structure of crystals [21]. When radiation travels through a crystal, the reflection from successive planes of atoms causes the radiation to interfere, leading to diffraction patterns of scattered light, where bright spots are produced by constructive interference and absences by destructive interference. This effect was explained by William Lawrence Bragg in 1913 using the famous Bragg equation [22]:

$$n\lambda = 2d\sin(\theta) \tag{2.1}$$

Where d is the separation of the atomic planes, θ is the angle between the incident wavevector and the lattice planes, λ is the wavelength of the incident radiation and n is the order of diffraction.

The spatial distribution of the pattern of spots created by diffraction is fundamentally linked to the symmetry of the atoms within the crystal, and can be used to understand the shape of the basis and the separation of lattice points. To do this we must first make a mathematical model of our crystal system, allowing us to make a simple transformation into the observed diffraction pattern.

2.1.1 The Crystal Lattice

A crystal lattice is made up of lattice points and a basis [17]. The lattice points are an infinitely repeating pattern of points described by a set of 3 non-parallel vectors $(\underline{\mathbf{a}}, \underline{\mathbf{b}}, \underline{\mathbf{c}})$, where any addition of these vectors will give a lattice point. The lattice points can be described by:

$$\underline{\mathbf{R}} = u\underline{\mathbf{a}} + v\underline{\mathbf{b}} + w\underline{\mathbf{c}} \tag{2.2}$$

where (uvw) are any integer values. On each lattice point there is a basis of atoms, where the arrangement of these atoms is defined by the point group. For pure Sodium Cobaltate, the basis comprises 8 atoms. The location of each basis atom is described in units of the basis vectors for each atom j by:

$$\underline{\mathbf{r}}_j = u_j\underline{\mathbf{a}} + v_j\underline{\mathbf{b}} + w_j\underline{\mathbf{c}} \tag{2.3}$$

where (uvw) are all less than 1. Convolving the basis of atoms with the lattice points will create the crystal lattice.

2.1.2 The Reciprocal Lattice

When studying diffraction images, the spots that can be seen are points that lie on the reciprocal lattice, τ:

$$\underline{\tau} = h\underline{\mathbf{a}}^{*} + k\underline{\mathbf{b}}^{*} + l\underline{\mathbf{c}}^{*} \tag{2.4}$$

and the reciprocal lattice is related to the real lattice via the transformation of basis vectors:

$$\underline{\mathbf{a}}^{*} = \frac{2\pi\underline{\mathbf{b}} \times \underline{\mathbf{c}}}{\underline{\mathbf{a}} \cdot (\underline{\mathbf{b}} \times \underline{\mathbf{c}})} \quad \underline{\mathbf{b}}^{*} = \frac{2\pi\underline{\mathbf{c}} \times \underline{\mathbf{a}}}{\underline{\mathbf{a}} \cdot (\underline{\mathbf{b}} \times \underline{\mathbf{c}})} \quad \underline{\mathbf{c}}^{*} = \frac{2\pi\underline{\mathbf{a}} \times \underline{\mathbf{b}}}{\underline{\mathbf{a}} \cdot (\underline{\mathbf{b}} \times \underline{\mathbf{c}})} \tag{2.5}$$

The integer values (hkl) define a position on the lattice in reciprocal space and are called the Miller indices. These are useful to define positions, directions or planes in reciprocal space and distinguish different families, $\{hkl\}$, of diffraction spots.

2.1.3 Conditions for Diffraction

While the Bragg equation determines the locations of specular reflections from a regularly spaced lattice, a more general approach was determined by Max von Laue [21]. In the case of elastic scattering, when the energy of incident ($\underline{\mathbf{k}}_i$) and scattered ($\underline{\mathbf{k}}_f$) waves are the same, $|k_i| = |k_f|$, the Laue equation states that the conditions for constructive interference (a diffraction spot) will be met when the difference, $\underline{\mathbf{Q}}$, between incident and scattered wavevectors is equal to a position on the reciprocal lattice:

$$\underline{\mathbf{Q}} = \underline{\mathbf{k}}_f - \underline{\mathbf{k}}_i = \underline{\tau} \tag{2.6}$$

To a first approximation therefore, diffraction spots will occur at the reciprocal points of the crystal lattice as defined by an integer addition of reciprocal lattice vectors. In most situations however, the diffraction data is slightly more complicated than just spots at the reciprocal lattice points, as spots can be missing or have varying intensities. These differences are a result of the basis of atoms at each real lattice point, as the difference in scattering power between different atoms can lead to systematic extinctions of certain spots.

In elastic diffraction experiments, the intensity of a diffraction spot is measured using the differential cross-section, defined as the number of hits on the detector per unit flux and solid angle. In the kinematic approximation [23], it has the general form:

$$\frac{d\sigma}{d\Omega} = N\frac{(2\pi)^3}{V}\sum_{\tau}|F(\underline{\mathbf{Q}})|^2\delta(\underline{\mathbf{Q}} - \underline{\tau}) \qquad (2.7)$$

where N is the number of unit cells scattered from and V is the volume of each cell. The delta function, $\delta(\underline{\mathbf{Q}} - \underline{\tau})$ ensures diffracted intensity is only found at the reciprocal lattice positions, following the Laue condition for diffraction. $F(\underline{\mathbf{Q}})$ is the structure factor, which describes a Fourier transform of the crystal basis:

$$F(\underline{\mathbf{Q}}) = \sum_{j} f_j e^{-i\underline{\mathbf{Q}}_{hkl}\cdot\underline{\mathbf{r}}_j} \qquad (2.8)$$

where $\underline{\mathbf{Q}}_{hkl}$ is the wavevector transfer of a point (hkl) on the reciprocal lattice, $\underline{\mathbf{r}}_j$ is the real space vector and f_j defines the scattering power of each atom j in the basis. The form of f_j is dependent on the radiation used. A full derivation of the differential cross section can be found for neutrons in [24] or for x-rays in [23].

2.1.4 Superlattices

In systems such as $Na_{x<1}CoO_2$, vacancies can order at long range within the crystal, making a larger pattern than the basic or average structure. The resulting structure can be dealt with in the same way as a normal crystal lattice, however, we call this lattice a superlattice, and the basis of atoms is called a superstructure, which is composed of an integer number of basic unit cells. We generate the superlattice by an integer addition of supercell, or propagation vectors, where each supercell vector is an integer addition of unit cell vectors:

$$\begin{aligned}\underline{\mathbf{a}}' &= n_1\underline{\mathbf{a}} + m_1\underline{\mathbf{b}} + o_1\underline{\mathbf{c}} \\ \underline{\mathbf{b}}' &= n_2\underline{\mathbf{a}} + m_2\underline{\mathbf{b}} + o_2\underline{\mathbf{c}} \\ \underline{\mathbf{c}}' &= n_3\underline{\mathbf{a}} + m_3\underline{\mathbf{b}} + o_3\underline{\mathbf{c}}\end{aligned} \tag{2.9}$$

These can be used to define the superlattice:

$$\underline{\mathbf{R}}' = u\underline{\mathbf{a}}' + v\underline{\mathbf{b}}' + w\underline{\mathbf{c}}' \tag{2.10}$$

In real space the superlattice spacing is larger than the normal lattice, therefore in reciprocal space the spots are closer together. In diffraction images we observe satellites or ‘Gittergeister’ (lattice ghosts) around the principal diffraction spots, which lie on the reciprocal superlattice [25].

The intensities of these superlattice peaks can be used to infer the ordering of ions within the superstructure. This has been found to be a very useful technique in the study of Sodium Cobaltate, where vacancies from sodium ions order into vacancy clusters, and these clusters form long range patterns in the material as illustrated in figure 2.1.

2.1.5 Symmetry Domains

For any crystal system there are a defined number of symmetry operations, dependent on the system’s space group. In a crystal system with a superlattice, this means that the superlattice will be formed in all symmetric orientations dependent on the underlying structure. Sodium Cobaltate is a hexagonal system with space group $P6_3/mmc$ (see section 1.2.2), so there are 6 rotations and 4 reflections within the plane perpendicular to (001), giving a maximum of 24 different orientations in

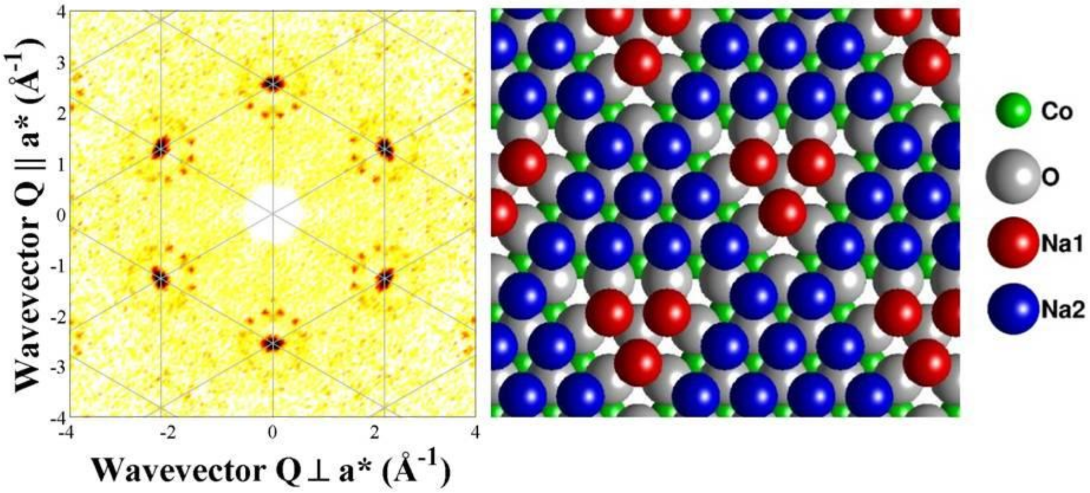

Figure 2.1: Diffraction pattern with satellite peaks and associated sodium ordering in $Na_{0.8}CoO_2$.

which the superlattice can form. In a real crystal, the superlattice will form domains in all of these orientations, so any scattering from the crystal is an average over all domains.

2.1.6 Correction Factors

The diffracted intensity for a given (hkl) reflection is directly proportional to the square of the modulus of the structure factor, F, which is ultimately what we want to calculate in order to solve the structure. There are various factors for single crystal data that, when evaluated, allow us to correct the measured intensity to determine $|F|$, according to the equation below:

$$I_{hkl} = cL(\theta)P(\theta)A(\theta)E(\theta)|F_{hkl}|^2 \tag{2.11}$$

These corrections are used both in neutron and x-ray diffraction analysis. The Lorentz correction, $L(\theta)$, accounts for the shape of the Ewald sphere in real space, as some reflections are measured for marginally longer than others depending on their angle. The absorption $A(\theta)$ and extinction $E(\theta)$ corrections are sample dependent and account for the radiation being absorbed by the sample (absorption) or a loss of intensity due to the radiation scattering multiple times from different lattice planes (extinction). The polarisation correction, $P(\theta)$, accounts for any polarisation of the beam by the monochromator or by the sample. In the former case, the extent of polarisation depends specifically on the set up of the instrument, whereas in the latter case, the polarisation is dependent on the value on 2θ and is given by $P = (1 + \cos^2 2\theta)/2$. The factor c is an arbitrary constant called the scaling factor [26, 27].

2.2 Techniques with neutrons

Neutrons are an ideal type of radiation to study the atomic structure of crystals, as the lack of any charge on the neutron means it can scatter directly from the nucleus of an atom, meaning the atomic positions can be measured in a very clean manner. The neutron does, however, have one way of interacting with the surrounding electrons of an atom, which uses to the neutron's magnetic moment. The interaction between the neutron and electron spin states is a very powerful method of determining the magnetic properties and structure of materials. [The key disadvantage with neutrons is the difficulty in producing them, leading to neutron techniques being flux-limited, meaning counting times must be very long in order to produce reliable statistics.

The structure factor for neutron scattering $F_Q^{neutron}$ is split into nuclear (N_Q) and magnetic (M_Q) components:

$$F_Q^{neutron} = N_Q + M_Q \tag{2.12}$$

2.2.1 Nuclear scattering

The neutron interacts with the nucleus via the strong force. This interaction is difficult to model, however scattering from thermal neutrons (with an energy equivalent to 300K) can be approximated by short-ranged pseudo-potentials, leading to a scattering length b_j dependent on isotope [24]. Scattering lengths are generally determined experimentally and are well tabulated [28]. Because the scattering length is dependent on isotope there are variations on the scattering length throughout a crystal. If we assume that all these scattering lengths are the same, we can use the coherent cross section that depends on the correlations between different nuclei at different times causing interference effects such as diffraction. However in a real system there is variation to the scattering lengths from different isotopes of the same element, and this variation leads to the incoherent scattering cross section. Incoherent scattering arises from the correlation between the positions of the same nucleus at different times and does not cause interference, therefore providing a flat background. In this work we are primarily interested in crystal structures and therefore the interference patterns generated, as such we will use only the coherent scattering here.

The simplicity of this model allows for simple calculations of nuclear structure factor:

$$N_Q = \sum_j b_j e^{-i\underline{\mathbf{Q}}_{hkl}\cdot\underline{\mathbf{r}}_j} \tag{2.13}$$

Because the neutron scattering lengths are dependent on nuclear properties, such as the binding energies and other complex properties, there is no general trend to the scattering lengths with the atomic number as there is in x-ray scattering. This gives neutron scattering several advantages for certain materials, especially in materials involving light elements such as hydrogen or lithium, where the scattering interaction is comparatively much stronger compared to x-ray techniques. When determining crystal structures using diffraction techniques, it is the contrast between the scattering power of different atoms within the basis that allows their exact locations to be determined, due to the increased difference in scattered intensities produced. Therefore, the combination of both neutron and x-ray techniques will always lead to the best determination of a given structure, because the different techniques will almost always have different scattering contrasts between the various elements in the system under study.

2.2.2 Magnetic scattering

By interacting with the spin states of electrons around an atom, neutrons can scatter from long range magnetic ordering and are sensitive to magnetic excitations. The treatment of the magnetic scattering of neutrons is based on the interaction potential, $\underline{\sigma}_n \cdot \underline{\mathbf{B}}$, between the neutron, of magnetic moment $\underline{\sigma}_n$, and the magnetic field $\underline{\mathbf{B}}$ within the solid, arising from the atomic magnetic moments.

The magnetic component of the structure factor is dependent on the direction of the incident neutron moment, $\underline{\sigma}_n$:

$$M_Q = p\underline{\mathbf{M}}_{\perp Q} \cdot \underline{\sigma}_n \quad (p = 0.2695 \times 10^{-12} cm/\mu_B) \tag{2.14}$$

meaning the interaction is sensitive to the orientations of spins in the system. The magnetic structure factor $\underline{\mathbf{M}}_{\perp Q}$ is given by:

$$\underline{\mathbf{M}}_{\perp Q} = \sum_m f_m(Q) e^{-i\underline{\mathbf{Q}} \cdot \underline{\mathbf{r}}_m} [\underline{\mathbf{M}}_m - (\underline{\hat{\mathbf{Q}}} \cdot \underline{\mathbf{M}}_m)\underline{\hat{\mathbf{Q}}}] \tag{2.15}$$

where $f_m(Q)$ is the magnetic form factor, r_m is the position and $\underline{\mathbf{M}}_m$ is the local magnetic moment in μ_B of the magnetic atom m [29]. The magnetic cross section for neutron scattering is often comparable in magnitude to the nuclear cross section, meaning that diffracted magnetic intensities are usually large enough to observe easily, even when there is nuclear scattering in the system. This distribution of electrons around an atom gives the magnetic scattering a form factor, which leads to a fall off in intensity when moving further out in reciprocal space. The additional term in the magnetic structure factor demonstrates that magnetic neutron scattering is only sensitive to magnetic moments in a sample with a moment perpendicular to the wavevector, $\underline{\mathbf{Q}}$ [24].

The interaction between the neutron and electron is dependent on their relative spin orientation. Polarisation analysis can be used to control the direction of spin of the incident neutron and measure the spin direction of the scattered neutron, allowing the spin directions of the material's electrons to be determined. The rotation of a neutron's spin through a material will infer the magnetic structure within the material. There are two important modes of polarised neutron scattering:

- Non-Spin-Flip (NSF) - the measured polarisation is in the same direction as the incident neutron polarisation.
- Spin-Flip (SF) - the measured polarisation is in the opposite direction to the incident neutron polarisation.

Structural scattering occurs only in the NSF channels. Magnetic scattering has components in both the NSF and SF channels, however we are only sensitive to the magnetic moments perpendicular to $\underline{\mathbf{Q}}$. The NSF scattering is sensitive to components of the magnetic moment that are parallel to the polarisation direction and SF scattering is sensitive to components perpendicular to the polarisation direction [30].

By measuring and combining counting statistics from several different polarisation directions, it is possible to calculate the individual components of the system's magnetic moment [31, 30]. The diagonal components require only the three single direction spin flip channels, given by $\sigma^{i\bar{i}}$, where i is the polarisation direction. The standard notation for polarisation directions is to have $\underline{\mathbf{x}}$ pointed along $\underline{\mathbf{Q}}$, $\underline{\mathbf{y}}$ will be at 90° to this, within the scattering plane (the plane with $\underline{\mathbf{k}}_i$, $\underline{\mathbf{k}}_f$ and $\underline{\mathbf{Q}}$ in) and $\underline{\mathbf{z}}$ will be orthogonal to $\underline{\mathbf{x}}$ and $\underline{\mathbf{y}}$. The magnetic cross section perpendicular to $\underline{\mathbf{Q}}$ is given by the relation:

$$M_\perp^* \cdot M_\perp = (\sigma^{x\bar{x}} + \sigma^{\bar{x}x}) - \frac{1}{2}(\sigma^{y\bar{y}} + \sigma^{\bar{y}y} + \sigma^{z\bar{z}} + \sigma^{\bar{z}z}) \tag{2.16}$$

with the component in the scattering plane:

$$M_\perp^{y*} \cdot M_\perp^{y} = \frac{1}{2}(\sigma^{x\bar{x}} + \sigma^{\bar{x}x}) - \frac{1}{2}(\sigma^{y\bar{y}} + \sigma^{\bar{y}y}) \tag{2.17}$$

and the component perpendicular to the scattering plane:

$$M_\perp^{z*} \cdot M_\perp^{z} = \frac{1}{2}(\sigma^{x\bar{x}} + \sigma^{\bar{x}x}) - \frac{1}{2}(\sigma^{z\bar{z}} + \sigma^{\bar{z}z}) \tag{2.18}$$

Off-diagonal components of the tensor can be calculated where the scattered polarisation direction is different to the incident direction. A chiral term can be obtained by using:

$$i\hat{x}(M_\perp^* \times M_\perp) = \frac{1}{2}(\sigma^{xy} - \sigma^{\bar{x}\bar{y}} + \sigma^{x\bar{y}} - \sigma^{\bar{x}y}) \tag{2.19}$$

This is useful for twisting magnetic structures, such as spirals and cyclical structures. The nuclear-magnetic cross terms can be obtained from the relations:

$$N^* \cdot M_\perp^{y} + N \cdot M_\perp^{y*} = \frac{1}{2}(\sigma^{xy} - \sigma^{\bar{x}\bar{y}} - \sigma^{x\bar{y}} + \sigma^{\bar{x}y}) \tag{2.20}$$

$$N^* \cdot M_\perp^{z} + N \cdot M_\perp^{z*} = \frac{1}{2}(\sigma^{xz} - \sigma^{\bar{x}\bar{z}} - \sigma^{x\bar{z}} + \sigma^{\bar{x}z}) \tag{2.21}$$

These terms are likely to be significant in systems where the magnetic and structural periodicities are the same and, in come cases, they may give enhanced sensitivity to the magnetism. Explanations of the above cross sections can be found in references [31] and [30].

2.2.3 Generation of neutrons

Neutrons can be produced for scientific purposes in one of two ways, either in a reactor where an enriched uranium core will undergo a fast fission process (uranium atoms are split into smaller isotopes and neutrons are emitted in the process), or by the spallation method, where protons are accelerated and shot at a heavy metal target, causing a controlled fission reaction.

At ISIS, the spallation method is used, using an 800 MeV proton accelerator to collide high energy protons with a tungsten target 50 times per second [32]. The spallation process occurs within the target and fast neutrons are produced, which are slowed using a hydrogenous moderator (hydrogen has a similar mass to a neutron and therefore will take much of a neutrons energy during a collision, slowing them down to useful speeds). This process allows neutrons to be produced in pulses, meaning sensitive timing equipment can be used to accurately determine the energy of neutrons during an experiment in a process called ‘time-of-flight’. This has advantages for designing particular types of instrument such as SXD, where the energy of the neutron hitting the sample must be known.

The ILL uses a high-flux reactor to produce a continuous neutron flux [33]. The ILL is currently the most intense neutron source in the world, and this makes the instruments here ideal for measuring weak scattering from inelastic processes or complex magnetic materials.

2.2.4 SXD at ISIS

SXD stands for Single crystal Diffractometer, the instrument consists of a large sample space (with the ability to add an assortment of sample environments such as cryostats or the furnace) surrounded by 11 large area detectors. The instrument works from the time-of-flight principle, as neutrons are created at a specific time when protons hit the spallation source, and then separate according to their energy (velocity). Assuming no energy is lost in scattering through the sample, the time at which they hit the detector relative to their start time will give the neutron energy, and with a full spectrum of neutron energies incident on the sample, much larger portions of reciprocal space are observable [34].

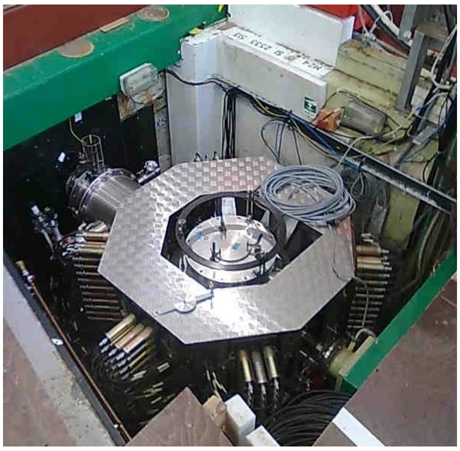

Figure 2.2: SXD at ISIS

The coverage of reciprocal space on SXD is best described using the Ewald sphere construction in figure 2.3. The diagram illustrates that for a range of incident neutron wavelengths, between $\lambda_{min} = 2\pi/\kappa_{max}$ and $\lambda_{max} = 2\pi/\kappa_{min}$, and with large angular coverage of scattered reflections, a large area of the wavevector transfer, $\underline{\mathbf{Q}}$, can be obtained, allowing a large number of reciprocal lattice points to be measured simultaneously. During an experiment, large volumes of reciprocal space are covered, which is ideal for locating superlattice reflections.

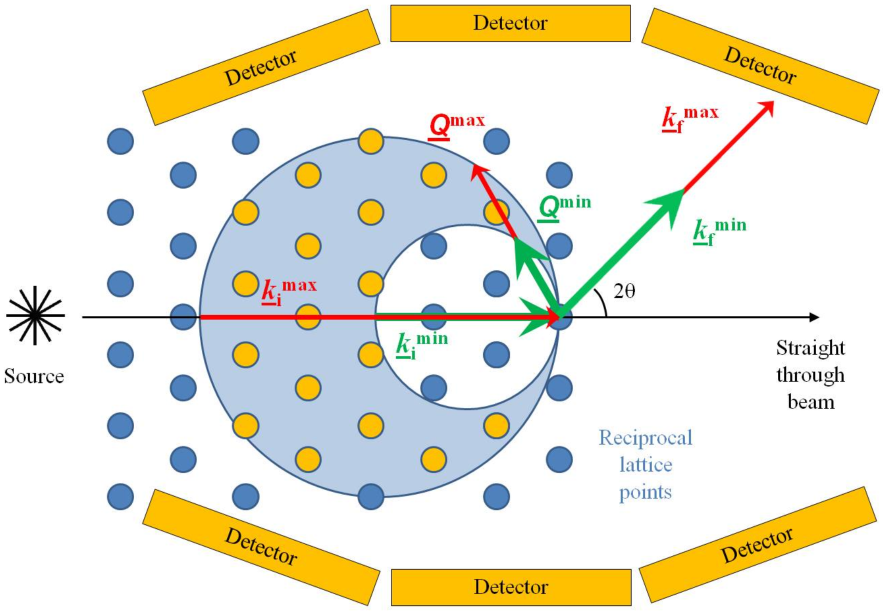

Figure 2.3: Ewald sphere construction for SXD. A pulse of neutrons is incident on the sample with wavelengths between $\lambda_{min} = 2\pi/\kappa_{max}$ and $\lambda_{max} = 2\pi/\kappa_{min}$, these neutrons are scattered from the sample into one of the 11 area detectors. Any reciprocal lattice points within the wavevector transfer volume, $\underline{\mathbf{Q}} = \underline{\mathbf{k}}_f - \underline{\mathbf{k}}_i$ will be observed in the detectors. The observed lattice points are shown in yellow.

2.2.5 IN20 at ILL

The beamline IN20 is situated within the main reactor building of the ILL, very close to the reactor core. This gives IN20 a very large neutron flux, which is ideal for magnetic and inelastic scattering experiments. IN20 is a triple-axis spectrometer, meaning that the instrument has 3 specific components, all of which can rotate about their own axis. The monochromater crystal is the first component and this selects a single wavelength of neutrons from the white beam emitted by the core, in the same way that a prism refracts different wavelengths of light. The sample sits at the second axis, allowing a single plane of diffraction. At the final axis is an analyser crystal, which sits in the diffracted beam and selects the outgoing wavelength, allowing inelastic measurements, where the neutron can lose or gain energy during scattering. After the analyser sits a detector, which uses helium-3 to accurately count the number of neutrons diffracted from the crystal (at the wavelength determined by the analyser crystal).

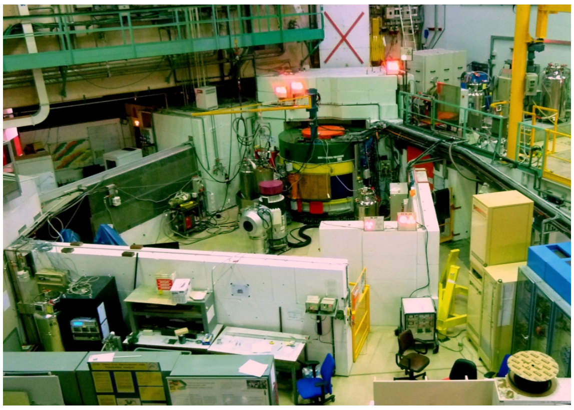

Figure 2.4: IN20 with CRYOPAD at ILL

Controlling the neutron polarisation through the sample is possible on IN20. This is a difficult task, however, as the spin will precess in an external field. Guide fields were initially fitted to experiments to guide the neutron spin orientation, though this limits the components of polarisation that can be measured [35]. Zero-field polarimetry is a relatively new technique used to achieve zero field at the sample position and allow full control of the neutron polarisation [36]. This additional control is useful for particularly complex magnetic structures, such as non-collinear magnetic structures [37]. CRYOPAD on IN20 is a pioneering device for this technique [29].

CRYOPAD uses two cylindrical low-temperature niobium Meissner magnetic shields to remove any stray magnetic fields around the sample, illustrated in figure 2.5. The shields are transparent to neutrons and their polarisation, and the transition between the guide-field and zero-field regions is non-adiabatic. Incident neutrons have their moments aligned using a guide-field, then a particular polarisation direction is chosen using nutator coils before the zero-field region. A second nutator selects what scattered polarisation direction to measure. The polarisation direction at either stage can be oriented along the scattering vector (x), perpendicular to this but within the scattering plane (y) or orthogonally out of the scattering plane (z). Counting at all combinations of these directions, including negative directions, gives 36 different cross sections. Combinations of these cross sections can be made to determine diagonal and off-diagonal components of the magnetic scattering, see above.

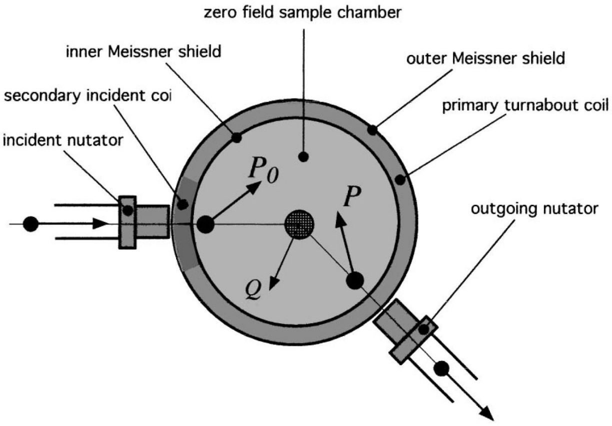

Figure 2.5: Spherical neutron polarimetry in CRYOPAD, from figure 1, Ref. [29]

2.3 Techniques with x-rays

X-ray radiation has been used to study the arrangement of atoms in crystals for almost one hundred years and are now a very well established technique in crystallography. X-rays are used to probe materials by utilising the interaction between the incident photon and the electrons in a material. The greatest density of electrons is always tightly bound around atoms, therefore in crystals where the atoms are ordered, this gives rise to diffraction. The scattering power of a single atom is dependent on the density of electrons, $\rho(\underline{\mathbf{r}})$ around that atom. The atomic form factor describes the scattering power by integrating over the electron density about a single atom:

$$f^0(Q) = \int \rho(\underline{\mathbf{r}}) e^{-i\underline{\mathbf{Q}}\cdot\underline{\mathbf{r}}} d\underline{\mathbf{r}} \tag{2.22}$$

This result does not take into account the behaviour of tightly bound electrons close to the atom centre, where absorption and emission processes can drastically change the scattering power. The full atomic form factor therefore also includes the dispersion corrections, f' and f'', dependent on the x-ray energy $\hbar\omega$:

$$f(\underline{\mathbf{Q}}, \hbar\omega) = f^0(\underline{\mathbf{Q}}) + f'(\hbar\omega) + if''(\hbar\omega) \tag{2.23}$$

The dispersion corrections assume their extremal values when the x-ray photon has an energy close to the binding energy of an inner-shell electron, leading to an increase in scattering called resonant scattering. The most tightly bound electrons are those in the K shell, and thus the resonant scattering is strongest at the K absorption edge [23].

2.3.1 Structural scattering

In the case where x-ray energies are not close to an absorption edge, the structure factor can be calculated using only the charge part of the atomic form factor:

$$F_Q^{xray} = \sum_j f_j^0(Q) e^{-i\underline{\mathbf{Q}}_{hkl}\cdot\underline{\mathbf{r}}_j} \tag{2.24}$$

The charge part of the atomic form factor can be calculated using experimentally determined parameters and the magnitude of the scattered wavevector (Q):

$$f^0(Q) = \sum_{i=1}^{4} a_i e^{-b_i Q^2/(16\pi^2)} + c \tag{2.25}$$

The parameters a_i, b_i and c are given in the International Tables of Crystallography [38]. The scattering power of an atom will increase with the number of electrons surrounding the nucleus and therefore the atomic number Z (indeed when Q is equal to zero, $f^0(0) \rightarrow Z$). This means light atoms scatter very weakly whereas heavy atoms such as cobalt dominate the diffracted intensities.

2.3.2 Resonant scattering

When an incident x-ray photon interacts with the electrons around an atom with an energy close to the binding energy of the electrons, absorption or re-emission can occur, see figure 2.6. In this case the dispersion corrections, f' and f'' take their extremal values, where f'' is negative, leading to absorption, as illustrated in 2.7. The dispersion corrections are primarily dependent on the energy of the photon so measurements at a synchrotron can observe the resonant enhancement of these terms by varying the x-ray energy. The technique was originally developed to study the anisotropy of unoccupied electronic states [39] but can also be used to measure charge and orbital ordering [40], due to the sensitivity to the electronic structure.

Resonant scattering is also sensitive to the magnetic ordering within a material and has been observed in nickel and holmium [41, 42].

Scattering from anisotropic ordering such as magnetism or orbital ordering can lead to changes in the polarisation of scattered photons. Polarisation analysis in resonant x-ray scattering experiments therefore allows an additional tool to distinguish between types of scattering. Polarisation analysis notation for resonant scattering is defined relative to the scattering plane, where σ is the parallel to the scattering plane and π is perpendicular to it. The resonant x-ray scattering theory was reformulated for this notation, assigning cross sections to the various electric and magnetic transitions [43]. An electric dipole transition (E1) will give the largest cross section and therefore dominate the resonant scattering. Quadrupole transitions (E2) are usually small but can become significant, producing pre-edge peaks in an energy scan. The type of transition can be determined by calculating the cross sections and comparing to experimental data, this can give information on the electronic states in a material.

During an experiment, scans of the incident x-ray energy are performed around the electron binding energies. The sharp increase in absorption at this energy is why this energy is called an absorption edge. The principal absorption energy for cobalt is called the Co-K absorption edge and is at 7.71keV. The absorbed x-ray photons are re-emitted as a fluorescent background in all directions around the material, and the energy dependence of this background can be used to study the electronic structure of the system.

In special cases where there is ordering of the electronic structure, resonant scattering can occur at a material's absorption energy causing an increase in intensity at the diffracted Bragg peak. This resonant scattering can be caused by a number of phenomena:

- Charge Ordering - charged ions arrange themselves into ordered patterns

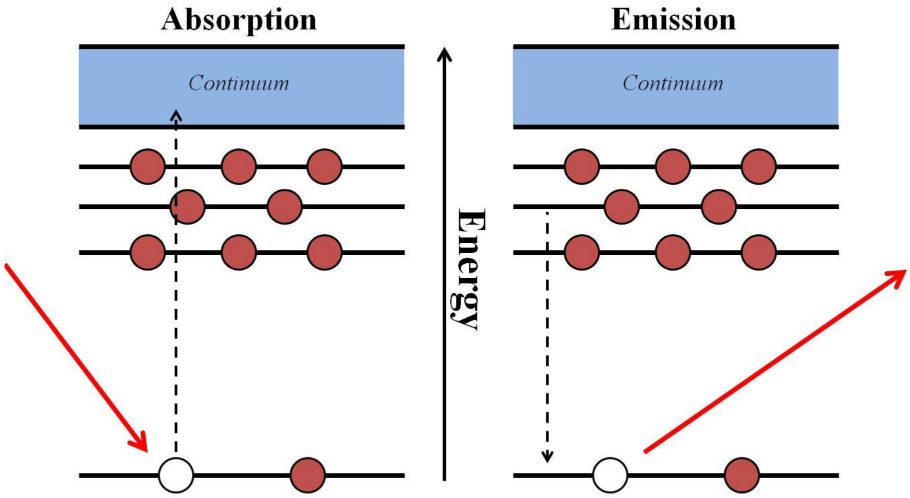

Figure 2.6: An x-ray (red line) can be absorbed in an atom when an electron (red ball) is promoted from a core energy level to a state in the continuum, becoming a photoelectron. The core level can then be reoccupied by an electron from an outer shell, emitting a photon in the process.

- Magnetic Ordering - magnetic ions arrange themselves into ordered patterns
- Orbital Ordering - the electronic orbitals around an atom arrange themselves into ordered patterns
- Jahn-Teller Distortions - distortions in the cobalt-oxygen bond length arrange themselves into ordered patterns

Using a variety of different techniques and procedures, the cause of resonant scattering can usually be determined experimentally. By controlling the polarisation of incident and reflected x-rays, it is possible to sort between isotropic electronic scattering (from charge ordering) or anisotropic scattering (from the others). Keeping the incident and scattered wavevectors constant but rotating the sample through the azimuthal angle (the rotation about the vector $\underline{Q}$) will determine the shape of the electronic scattering and also help distinguish between the different types of scattering. Magnetic ordering can be determined by looking at a number of dif-

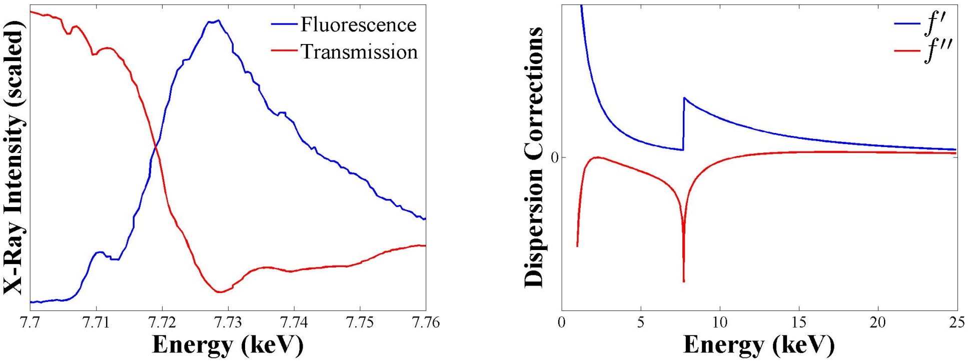

Figure 2.7: Changes in scattering at x-ray absorption edges. Transmission of x-rays through cobalt reduces significantly at $\approx 7.71keV$, but a fluorescent background is emitted (intensities are scaled for visual aide). At this energy, the dispersion corrections for cobalt show a sharp drop in f' and a rise in f''.

ferent Bragg reflections, where resonant magnetic scattering will occur at specific positions depending on the magnetic structure. It is often required, however, to use sophisticated modelling software to infer additional information about the electronic structure of a material by comparing experimental and calculated energy and azimuthal dependences.

Resonant x-ray diffraction is a relatively new technique but the ability to measure complex magnetic and electronic ordering with x-rays has many advantages, such as requiring smaller samples and shorter counting times than neutrons. The technique has been successful in investigating many complex materials, for example the observation of charge order at the metal-insulator transition in $NdNiO_3$ films [44]. The technique has also been successful in combination with neutron measurements to determine the magnetic ground state of $CeFe_2$ [45].

2.3.3 Generation of x-rays

X-ray radiation can be produced in a number of ways. For typical lab based equipment, x-rays are produced by colliding high energy electrons with heavy metal targets, such as copper or molybdenum. The electrons are produced by a Cathode and are accelerated towards their target. On collision, two processes occur that produce x-rays. The first is the Bremsstrahlung (breaking) process in which a continuous spectrum of radiation is produced by electrons slowing down in the material. The second process is fluorescence which produces a sharp resonance in intensity at a particular energy, caused by the collision of the incident electron with an atom. The collision causes an atomic electron to be removed from an inner shell, creating a vacancy. An atomic electron from a higher energy shell will then relax to fill the vacancy, emitting a photon with an energy equal to the change in energy state. The greatest intensity of x-rays is produced at the K_α energy of an element, which involves a transition from the second to first electron shells. A monochromator, such as a well diffracting crystal, can be used to select only the high intensity K_α radiation from the source, which can then be collimated towards a crystal sample for diffraction.

In a synchrotron, much greater intensities of x-rays can be produced by accelerating electrons with strong magnetic fields. If electrons are held at relativistic speeds, they will emit radiation when they are accelerated in a strong magnetic field, such as in a bending magnet or undulator (which causes electrons to oscillate on a straight segment of the synchrotron ring). This produces a continuous spectrum of radiation, and a series of optics can be used to select a single wavelength. Synchrotron radiation can be used in an enormous number of different ways, and many instruments are usually set around the ring of a synchrotron to perform different types of experiment.

2.3.4 Xcalibur at Royal Holloway

The Xcalibur lab based diffractometer uses the principles of x-ray diffraction to study single crystal samples with size of the order 0.1 – 0.5mm. It is a largely automated machine with powerful software called $CrysAlis^{Pro}$ which is able to run the instrument and analyse the data. A molybdenum source produces x-rays as described above for lab sources, and a single wavelength of 0.709Å is selected by a monochromator which is then collimated directly onto the sample. The sample sits on a 4-axis goniometer capable of rotating the sample through almost any angle. X-rays are diffracted in transmission through the sample and are captured by a CCD camera via a beryllium window and scintillation screen that converts the x-rays to visible light.

Experiments on the instrument take anything from 15 minutes to 12 hours and can give full coverage of reciprocal space. The software is capable of determining the unit cell of the system, suggesting the most efficient geometries for the experiment and integrating the Bragg peaks (corrected for absorption in the sample, background and other factors). Automated structural solution and refinement is also possible for simple materials using additional refinement software.

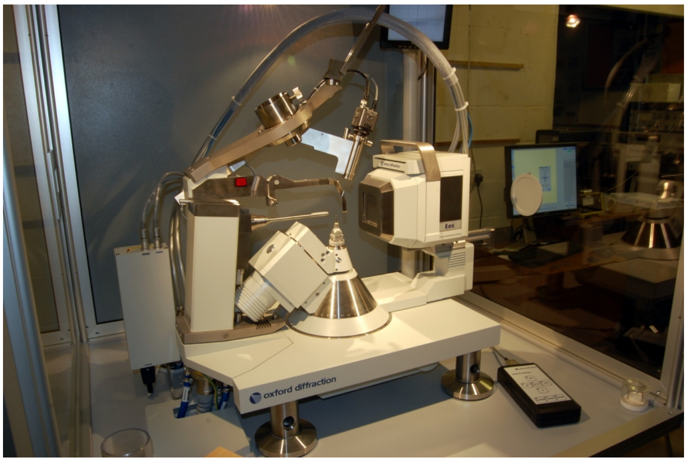

Figure 2.8: Xcalibur single crystal x-ray diffractometer at Royal Holloway

2.3.5 I16 at Diamond

I16 is a general purpose diffraction beamline at Diamond, which specialises in studying materials and magnetism. The general purpose nature of the instrument means that a large number of different options and sample environments are possible [46].

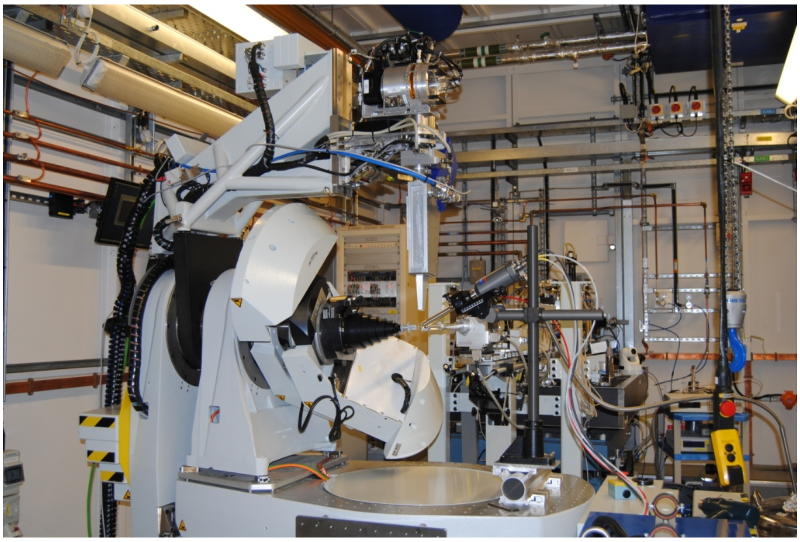

Figure 2.9: I16 Beamline at Diamond

X-rays are generated via an undulator on the synchrotron and are focused into a plane polarised, monochromatic beam in the optics hutch. The sample is mounted on the goniometer and placed in the beam. Scattered x-rays are measured using one of the components on the detector arm, such as the PILATUS area detector or the analyser crystal and point detector.

Resonant scattering experiments require control of the incident x-ray energy, x-ray polarisation, azimuthal angle and temperature. X-ray energy is controlled in the optics hutch and as described in figure 2.10, an analyser crystal and 6-axis goniometer are used to control the polarisation and azimuthal orientations. Various sample environments are available for control of temperature, such as the 6-800K cryofurnace.

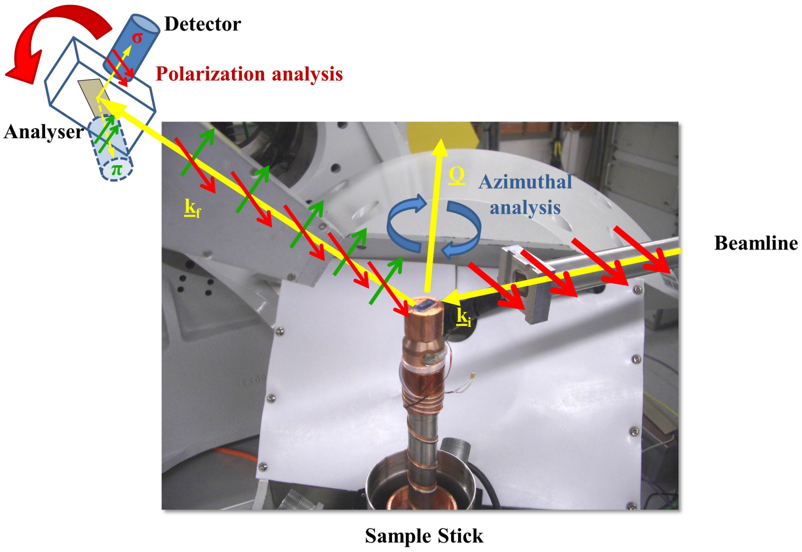

Figure 2.10: Polarisation and azimuthal control for resonant x-ray scattering on I16. Monochromatic, plane polarised x-rays are emitted from the beamline and scattered from the sample, where their polarisation can be rotated by anisotropic electronic environments within the sample. An analyser crystal is used to measure the unrotated (σ) or rotated (π) polarisation channels. Azimuthal analysis can be achieved by rotating the sample in the azimuthal plane, keeping incident and scattered positions fixed.

2.4 Other techniques

2.4.1 Crystal growth

Materials used in modern science are rarely found as natural compounds, instead they must be synthesized using special techniques and a chemical knowledge of the constituent elements. It is ideal to study these materials as crystals, where the atoms are arranged in ordered patterns throughout the entire material. However, to synthesize a material as a crystal is a difficult task, and often cannot be achieved in a simple way. Crystals can be grown from a compressed boule of powder using an image furnace, where the boule is subject to very precise conditions of heat, atmosphere and movement in order to allow a single grain of crystal to grow within the material. An image furnace uses high powered lamps to focus intense heat onto one region of the material, creating a molten zone. In the liquid state, atoms within the material are able to form bonds that will allow them to crystallize on cooling, and by moving the entire boule through the molten zone, the material will set as a large single crystal [47].

2.4.2 PPMS at Royal Holloway

A Physical Properties Measurement System (PPMS) is a work horse of condensed matter research. A sample environment is housed within a helium dewar, surrounded by a nitrogen jacket, allowing measurements of many physical properties to be taken at temperatures between room temperature and 1.8K. Various sample mountings can be used to measure resistivity, thermal conductivity, heat capacity or the Seebeck coefficient, as well as magnetic properties such as susceptibility. Measurements from the system are logged and analysed using a connected computer, allowing a standardisation of results.

At Royal Holloway there is a Quantum Design PPMS that has specific options to measure thermal transport properties in a material, including the Seebeck effect and thermoelectric figure of merit.

2.4.3 MPMS at Diamond

A Magnetic Properties Measurement System (MPMS) is an instrument similar to a PPMS, although it is designed specifically for highly sensitive measurements of magnetic properties. A MPMS uses a SQUID (Superconducting Quantum Interference Device) magnetometer, which comprises two superconducting coils that can detect incredibly small magnetic fields. The magnetic moment of a sample can be measured at a range of temperatures and external magnetic fields using one of two methods.

Either the sample is vibrated through the superconducting coils (thus inducing a current in the coils via Lenz's law) or an AC field is created inducing a varying magnetic response in the sample which can be measured by the superconducting coils.

The MPMS SQUID VSM (Vibrating Sample Magnetometer) at Diamond allows very precise measurements of the DC susceptibility of a sample at a range of temperatures. Temperature and field sweeps can be acquired and samples of less than 5mm can be mounted in different orientations.

Chapter 3

Computational Techniques

3.1 Reverse Monte Carlo

After a diffraction experiment has been performed, the standard crystallographic procedure is to run the integrated diffraction peak intensities through commercial programs that solve the crystal structure. However, Sodium Cobaltate exhibits superlattice patterns where the size of the unit cells and the complexity of the diffraction patterns mean that the commercial software does not produce reliable results.

Instead we have developed our own program to solve the superstructures of our systems, using a technique called Reverse Monte Carlo (RMC). This program allows the parameters of the system to vary freely at the beginning as if the structure was at high temperature, then instead of reducing the energy of the system, the fit to the experimental data is reduced [48]. RMC methods have been successful in determining the short range order within disordered materials [49] and also have been used to determine superstructures in Sodium Cobaltate [50]. Monte Carlo methods are used here to produce random movements throughout the lattice, and the Metropolis algorithm makes this more efficient by accepting these random moves if they make the structure more consistent with the experimental data, or with a probability that can be controlled.

Example code using this technique can be found in appendix A, however in this section I will explain the main principles of the program. The basic flow chart in figure 3.1 explains the overarching process of this technique.

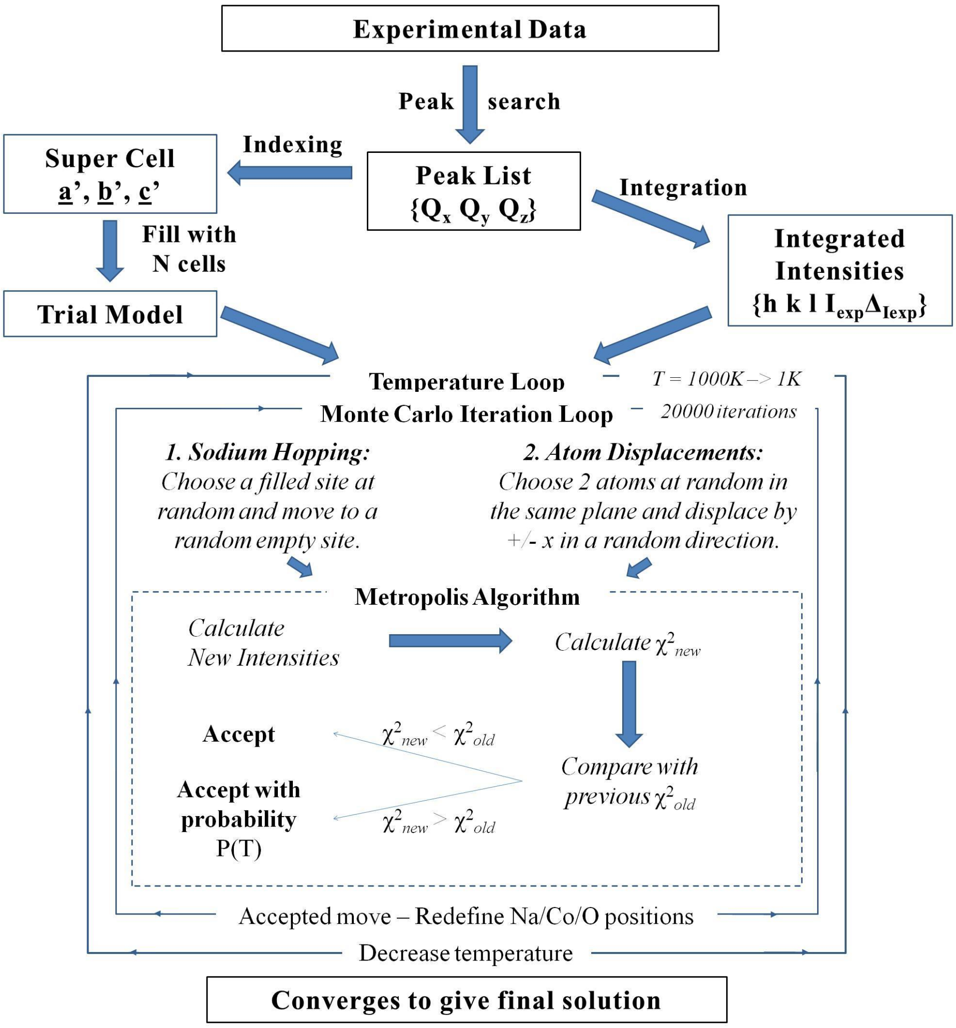

Figure 3.1: Flowchart of RMC analysis.

3.1.1 Background

The Monte-Carlo method was initially developed just after the second world war, within the "Manhattan" secret military project to improve nuclear weapons. Its aim was to use the numerical processing power of computers to simulate physical phenomena which are essentially stochastic: the interaction of neutrons, gamma rays etc... with matter. RMC modelling was developed further in the late 1980s for determining the structures of liquids and glasses [51]. In such systems, diffraction measurements provide information on the correlations between a pair of atoms at some separation r. By fixing the origin of the system to centre on an average atomic site (averaged over all atoms in the system, some atoms may be distorted away from the equilibrium position), the structure can be described in terms of a radial density function or radial distribution function. The values of these parameters (and thus the expected nuclear scattering) can be tuned by the movement of atoms until good agreement is found with the experimental data. This is the basic premise of the RMC method [48].

Since their initial application to liquids and glasses, RMC techniques have been applied to a wide range of systems including single crystals, powders, polymers [48] and magnetic materials [52]. In each of these systems, the method relies upon the movement of an atom (or in the case of magnetism, the rotation and location of spin states) and the comparison of the expected scattering with the experimental data. This is in itself no different from the procedure of a Rietveld refinement. The difference is that the motion of the atoms is random, and thus the process and its models are statistical rather than deterministic in nature.

The RMC method will produce a structural model that is not unique, however this does not mean that the model is not useful as a way of understanding the system [53]. It is not right to ask if the model is "correct" as this can never be experimentally determined, all we know it that the model generated is one possible solution that matches the data points within experimental error. This point, whist in principle true of all scientific models, has been a key complaint of the RMC method [54]. Another complaint about RMC is that the statistical nature of the process means that some level of errors will be unavoidable in the final model, which due to their random nature, cannot be readily removed, however with adequate constraints they can be suppressed [55]. The papers mentioned earlier [48, 51, 52] describe situations where the use of RMC has led to useful models that have given a better understanding of a system. It should be pointed out however that the number of non-unique models for a system such as a glass or liquid is far greater than the number of non-unique configurations in a highly symmetric crystalline system such as the system we are modelling here, increasing the potential effectiveness of RMC in this situation.

In the Canonical Ensemble (a small system exchanging energy, imposing a temperature T), the probability for the system to be in some configuration X is proportional to the Boltzmann weight

$$e^{\frac{-E(X)}{k_B T}} \tag{3.1}$$

where $E(X)$ is the energy corresponding to the configuration X (X represents all degrees of freedom, e.g. coordinates of N interacting particles in 3D). Monte-Carlo methods can sample an ensemble of configurations X_i, according to a probability proportional to the Boltzmann factor, $\exp[-E(X)/k_B T]$. Various physical quantities (mean energy, specific heat, magnetization etc...) can be obtained by simple averages over those configurations X_i. In this domain, the first–and still widely used–algorithm was published by Metropolis et al. (a participant of the Manhattan project) in 1955 [56].

The Monte-Carlo method not only deals with physical problems which are stochastic in essence. It can also be very useful in finding solutions to deterministic problems, like the calculation of a multidimensional integral, or the search for the absolute minimum of a complicated function with many variables.

Finding the absolute minimum of a many-variable function $E(x_1, x_2, \cdots, x_N)$ is a challenging problem. Steepest descent methods work well in one or two dimensions, but for $N > 10$, finding the absolute minimum of E is very difficult. One of the most efficient methods, called "Simulated Annealing", uses Monte-Carlo techniques. Let us simply consider that the function $E(x_1, x_2, \cdots, x_N)$ represents the energy of a thermodynamic system with configurations $X = \{x_1, x_2, \cdots, x_N\}$. Start a Monte-Carlo simulation in Canonical Ensemble at high temperature T, where all configuration space is explored, then decrease the temperature. If the system is ergodic (all possible configurations can be reached) and the temperature decrease sufficiently slow, you will converge at $T \rightarrow 0$ to the ground-state energy, i.e. the absolute minimum of $E(x_1, x_2, \cdots, x_N)$.

Now, in the particular case, where $E(x_1, x_2, \cdots, x_N)$ represents the mean-square deviation between an experimental Neutron or X-ray spectrum and the calculated prediction from a configuration in real-space, the generally accepted term for the minimisation of $E(x_1, \cdots, x_N)$ through Monte-Carlo simulated annealing is "Reverse Monte-Carlo".

3.1.2 Theory

It is important to have some understanding of the statistical methods that RMC modelling is built upon. In many-dimensional configuration spaces, the most efficient algorithms use Markov chains. A Markov Chain is an *ordered* infinite sequence of random variables, where a single variable is dependent only on the variable preceding it and not on the chain of variables leading to it. After a sufficiently long time, the Markov Chain will converge to a non-unique distribution (dependent on the starting conditions). If the Markov chain is ergodic (i.e. the probability of a transition between any two configurations in a finite number of steps is non-zero), we can force the converged distribution into a unique limiting law, $f(x)$, using the "microreversibility condition" (also known as the detailed balance law). We can impose the limiting law to be a probability distribution corresponding to the Canonical Ensemble by choosing

$$f(x) = e^{\frac{-E(x)}{k_B T}} \tag{3.2}$$

where $E(x)$ is a value calculated from a configuration based on the variable x.

To satisfy the microreversibility condition, Metropolis proposed the following simple algorithm, which is still widely used.

1. Start from some arbitrary configuration X of your multidimensional system and calculate the corresponding energy $E(X)$.
2. Define from X a new "trial" configuration Y and calculate $E(Y)$. It is often most efficient to take Y not "too far away" from X, for example, you can only change one or a few variables, taken at random, among the many degrees of freedom defining X.
3. If $E(Y) \leq E(X)$ accept Y as the new configuration at time $t + 1$.
4. If $E(Y) > E(X)$ accept Y as the new configuration with probability

$$P = e^{\frac{-(E(Y)-E(X))}{k_B T}} \tag{3.3}$$

To do this, simply draw at random, a real number, η, uniformly distributed between 0 and 1. Accept Y as the new configuration at time $t + 1$ if $\eta < P$, otherwise reject Y and keep X as the new configuration at time $t + 1$.

In Sodium Cobaltate systems, the number of different configurations of Sodium ions within a supercell will become extremely large very quickly (there are over 4 million configurations for a supercell comprising of 5 sodium ions per layer in a supercell of only 7 unit cells!). It is therefore important to use an efficient algorithm that can cover a large proportion of all configuration. The Metropolis algorithm, as described above, is a realistic possibility, driving the changes to the model towards a probable solution.

3.1.3 Experimental Analysis

Single crystal diffraction data can be acquired using neutrons or x-rays as described in the previous chapters, but to use this data the diffraction peaks must be integrated. Software for each instrument is able to search through the raw diffraction data and pick diffraction spots from the background. These spots will be saved in a peak table containing their position in reciprocal space. Then, using a peak table containing hundreds or thousands of positions, the instrument software will use a fitting algorithm to determine the unit cell of the crystal sample, and transform the peak positions into units of the unit cell, (hkl). In a system with a superlattice, the superlattice vectors must be defined and the positions will be indexed in units of the supercell.

Accurate estimations of the diffracted intensity can then be acquired by integrating the experimental data at the reciprocal superlattice positions. Integration can be performed in a number of ways, and for large peaks the standard method is to fit a Gaussian or similar function to the peak and calculate the area under the curve. For small peaks however, the number of pixels around a peak is small and superlattice peaks do not fit well to a Gaussian function. It is easier and more reliable to perform a much simpler analysis, where at each superlattice position, the pixels around the position are summed up after removing the background, as illustrated in figure 3.2.

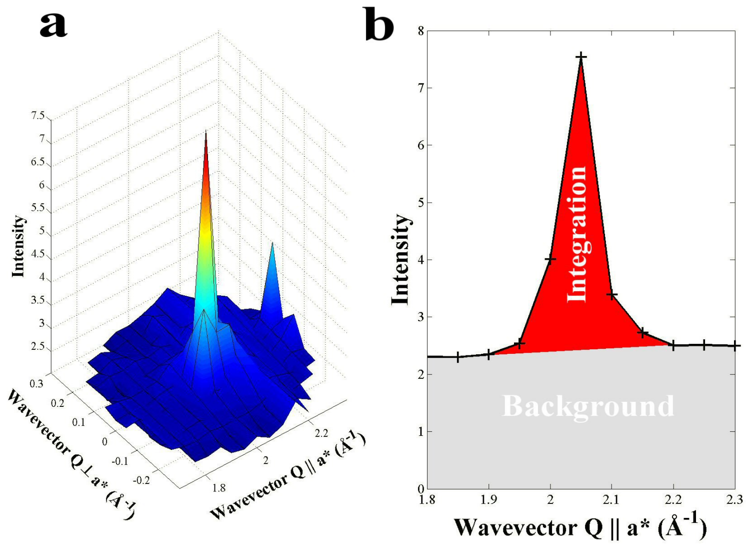

Figure 3.2: Integration of a superlattice peak. **(a)** A 2D cut through reciprocal space shows a superlattice peak. **(b)** Remove the background and sum the remaining pixels to acquire the integrated peak intensity.

Integrating every superlattice position over all of reciprocal space can give thousands of peak intensities, however it is important to check the integrated data for anomalous integrations, where impurities in the diffraction pattern have lead to an incorrect calculation of the intensity at that position. Anomalous integrations can effect the RMC calculations quite strongly and often lead the calculation to an incorrect structure.

3.1.4 Symmetry Domains

Sodium Cobaltate is a hexagonal system, and therefore has the rotation and inversion symmetries that apply to its space group. When a superlattice forms due to vacancy ordering, this ordering may have a lower symmetry than that of the average unit cell, and this means that the supercell could form in one of a number of different orientations with equal probability. These different orientations can occur simultaneously within the system, each giving their own contribution to the scattered intensity and what results is an intensity pattern that cannot be solved by only considering a single symmetric domain. To solve a structure of this type, we must calculate all of the component domain intensities that occur at each of the experimentally observed reflections, for instance a principal reflection will have a contribution from 12 different symmetrical domains but certain superlattice reflections will only have 6 contributions.

The different domains in Sodium Cobaltate systems can be modelled by applying the basic symmetries to the supercell, giving 12 different domain supercells. Each reflection can be indexed independently by each domain supercell, however not all positions will be indexed by all domain supercells. Reflections indexed with a given domain supercell will have an intensity contribution from that domain. All reflections from each domain are calculated, and for each observed reflection, all the domain contributions are summed, so that the calculated intensities, I_{calc} have the same contributions as the experimental data, I_{exp}.

3.1.5 Building a Trial Model

Using a supercell determined from the locations of diffracted satellite peaks, a basic model of the system is generated by building a lattice of enough unit cells to fill the supercell (this is always an integer number in our case). This will generate a supercell with two layers of cobalt-oxygen tetrahedra, and two layers of sodium. The sodium sites are filled at random up to the required concentrations of sodium and the dopants, where each layer is filled with the same number of atoms, but the arrangement within each layer will be different, as shown in figure 3.3.

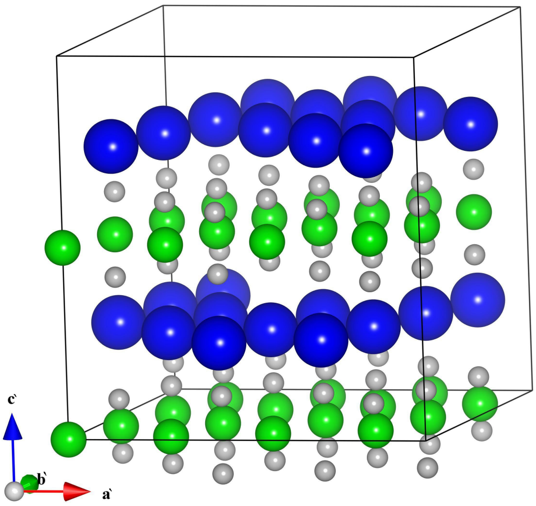

Figure 3.3: A supercell of $Na_{0.8}CoO_2$, filled with 15 Sodium Cobaltate unit cells, with random placement of sodium ions. Green balls are cobalt, grey, oxygen and blue are sodium.

This model is then used to calculate diffracted intensities at the same positions as the integrated peaks. The calculated intensity is then normalised against the experimental data by matching the total sum of the dataset:

$$I_{norm} = I_{calc}\sqrt{\frac{\sum I^2_{exp}}{\sum I^2_{calc}}} \tag{3.4}$$

3.1.6 Atomic Movements

During each iteration of the calculation, the atoms within the unit cell can move at random from their starting positions subject to several restraints. There are three programmed methods of movement, and these are described below.

Sodium hopping Sodium or dopant ions within the sodium layer can hop between different vacancy sites. They can hop to both Na1 and Na2 type positions. If a Na1 site is right next to a filled Na2 site, their separation would be closer than the ionic diameter of sodium and the short range repulsion would be large, so this move would not be allowed. Ions can hop within a layer but cannot hop between layers, keeping the concentration of each layer fixed.

Dopant switching When dopant ions are within the sodium layer, an additional movement is required that allows the swapping of scattering lengths between a sodium and dopant site. This helps prevent false minima solutions that can occur if the dopant ion cannot attempt all possible movements.

Atomic displacement Each ion in the supercell is able to make small movements away from their initial positions. Each movement is made as a small step in a random direction, however to stop a net travel of the superstructure in one direction, the movement of an ion in one layer is matched by the equal and opposite movement of an equivalent ion in a different layer, therefore keeping the centre of mass constant. The atomic displacements can be used to check for buckling in the cobalt-oxygen layers.

3.1.7 Metropolis Algorithm

After each movement type is performed, changes to the calculated intensities are determined and these are compared with the experimental values using the χ^2 distribution:

$$\chi^2 = \sum_{hkl} \frac{(I_{exp} - I_{calc})^2}{\Delta I_{exp}^2} \tag{3.5}$$

To determine whether this move has produced a better or worse fit to the experimental data, we use the Metropolis algorithm, described in general earlier and for this implementation in figure 3.4.

The new χ^2 value is compared with the previous value from the last iteration, if the new value is lower (a better fit) then the movement will be kept, and the structure will have changed. If the new χ^2 value is higher (less comparable to the experiment), then the movement is only kept with a certain probability. For this program we base our probability on a fictitious temperature, T, where the the probability that a bad movement will be kept obeys a Boltzmann distribution:

$$P_{keepmove} = e^{\frac{\chi^2_{old} - \chi^2_{new}}{k_B T}} \tag{3.6}$$

where k_B is the Boltzmann constant. Using the Metropolis algorithm means that good moves will preferentially and efficiently be taken but bad moves can still occur, allowing the model to sample many possible solutions and stopping the model from falling into a false minimum, which is an incorrect solution where no single atomic movement can improve the fit.

3.1.8 Simulated Annealing

By controlling the fictitious temperature, T, the probability of accepting a poor move can be controlled. At the start of the calculation, the temperature is high, so all movements are possible, irrespective of their effect on the fit to experimental data. After a large number of iterations (enough for a large coverage of possible solutions to be attempted), the temperature is reduced by a small factor and the movement iterations are run again. Over many temperature steps, the model anneals into the best fitting solution, similar to a molten metal cooling and setting into a crystal. If the changes in temperature are too great, then the model may anneal too quickly, causing the system to condense into a false minima.

The final model is then used to calculate two-dimensional cuts through reciprocal space that can be compared directly to experiment, as a final check of the solutions validity. Comparing the results by eye will often give more reliable results than

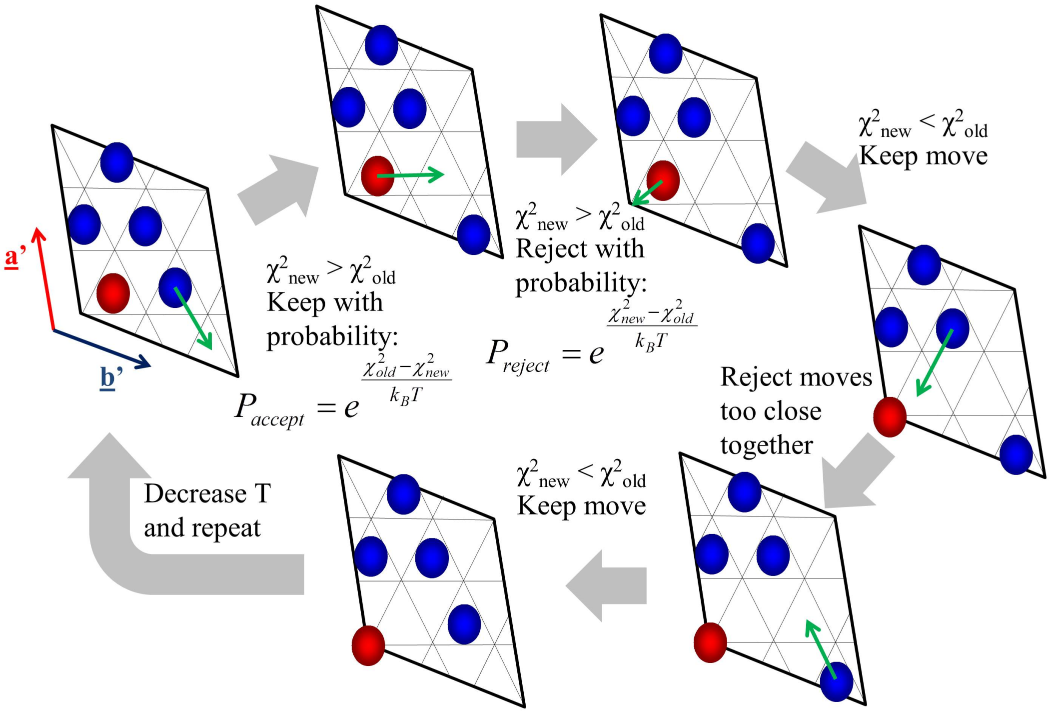

Figure 3.4: Diagram to show the Metropolis algorithm.

comparing χ^2 values, as anomalous integrations can distort them. The ratio χ^2/n_d can be used to measure the agreement between model and data, where n_d is the number of degrees of freedom (given as the data points minus the number of free parameters), and a good fit would be a value close to 1 [57]. The number of free parameters in the system can be given as $3N$, where N is the number of atoms in the system, although in practice this is not really accurate as the constraints imposed on atomic movements reduces this number. A weighted R-factor can also be calculated, which is a common alternative to the χ^2 distribution used in crystallography:

$$R_w = \sqrt{\frac{\sum \left| w \left| I_{exp} - I_{calc} \right|^2 \right|}{\sum \left| w I_{exp}^2 \right|}} \tag{3.7}$$

where the weighting factor, w, is usually $1/\Delta I_{exp}^2$. This parameter gives a percentage fit to the experimental data, where <20% would be a good fit and >70% has no correlation to the experiment.

3.1.9 Testing

The RMC code was tested by running the code on a simulated diffraction pattern. This testing was performed with the aid of David Voneshen, who performed testing as part of his undergraduate project.

A supercell of $Na_{0.8}CoO_2$ with tri-vacancy clusters in the square phase was used to calculate a set of diffracted neutron intensities. The intensities were given a Gaussian distribution to model experimental resolution and the error on each value was calculated as $\sqrt{I}$. A second model was also used that included periodic distortions in the cobalt layer. The simulated intensities were then used as the list of experimental data, I_{exp}, in the RMC code.

Solutions from the code revealed that, given enough independent reflections from the simulated model, the calculated model would reproduce both the sodium ordering and the cobalt distortions. However it was found that features such as annealing rate and the symmetry domain calculations were very important in achieving finer details such as the distortions. It was also found that running the program several times using different pools of random numbers (for random atomic movement and for the Metropolis algorithm) would allow us to asses the reliability of the solution, if different solutions appear then the solution may not be unique, though this was not usually found to be the case.

3.2 FDMNES

X-ray spectroscopy is related to the real or virtual absorption of x-rays in materials and is sensitive to the electronic and magnetic structures within the material. The cross section of x-ray scattering at energies around an absorption edge are dependent on both these degrees of freedom and on the polarisation and energy of the incident and scattered photons. The FDMNES program has been developed alongside the experimental techniques in this field and serves as an excellent tool in understanding the nature of resonant scattering from complex materials. FDMNES was written by Dr Yves Joly from Institut Néel, CNRS, Grenoble. The program is able to calculate the resonant x-ray scattering from a given crystal structure, calculating experimental observables such as the energy line shape and azimuthal dependence [58, 59].

3.2.1 Interactions of x-rays with matter

If we consider a material in a beam of x-rays, the process of anomalous scattering (a change in phase of the scattered x-ray due to absorption from the scattering atom) occurs when a photon has an energy close to the constituent chemical element's binding energy. This leads to a transition of a photoelectron from a core level to an unoccupied state. The transition can be permanent, where the photon is absorbed (measured in absorption spectroscopy) or temporary, when the excited electron will return to the core level, emitting a photon of particular energy. See figure 2.6.

Electronic transitions are dependent primarily on the binding energy, and therefore atomic number of an element, but also on the selection rules and energy states of the electronic structure of a material. The electronic states available to transitions are determined by the crystal structure and symmetry about the absorbing atom, though the polarisation of the incident photon will also vary the states available in the case of anisotropic orbitals about an atom. By describing the different scattering processes under a common formalism (in this case using multipolar operators of the photon-electron interaction), scattering amplitudes can be calculated that combine all interactions.

3.2.2 Electronic structure calculations

The calculation of the electronic structure of atoms, molecules and materials has been a rich topic of research for the past century. The difficulty in such calculations is due to the many-body nature of the problem, namely the simultaneous interaction of 10^{23} charged particles. Density Functional Theory (DFT) is a quantum mechanical modelling method used to investigate these systems, using functionals (functions of another function) of the electronic density to solve the Schröedinger equation.

DFT takes its functional roots from the Thomas-Fermi model [60, 61] and Hohenberg-Kohn theorems [62], however the modern framework is established with the Kohn-Sham equations [63]. In the Kohn-Sham framework, the intractable many-body problem of interacting electrons in a static external potential is reduced to a tractable problem of non-interacting electrons moving in an effective potential. The effective potential includes the external potential and the effects of Coulomb interactions between the electrons (exchange and correlation). Modelling the electron interactions is still difficult at this level and approximations are required to simplify their calculation. The simplest approximation is the local density approximation (LDA), which calculates the orbitals of a single electron and treats it as a uniform electron gas [64, 65].

In practice, there are a number of methods to solve the Kohn-Sham equations, with different methods being favoured for different systems. The methods used by FDMNES are the Finite Difference Method (FDM) or the multiple scattering method. In the FDM, the electronic potential for the one-electron orbital is free and does not use approximations. This method becomes too demanding for complex systems such as ours, so instead multiple scattering is used. The multiple scattering method uses the Green formalism on a muffin-tin potential, which can be less precise but much faster. The muffin-tin potential approximation is valid for dense metals with high symmetry, such as Sodium Cobaltate.

3.2.3 Calculation details

The program is split into two distinct parts:

1. The first concerns the calculation of the final state towards which the photoelectron will transit. This calculation is performed by solving, *ab initio*, the Schrödinger equation using the Finite Difference Method (FDM) or the method of multiple scattering.

2. Once all possible final states have been calculated, the transition matrices are determined between the initial and final states. These are summed to obtain the structure factors and then the scattering cross sections, allowing direct comparison with experimental data. The calculation takes into account the polarisation of the incident and scattered photon.

3.2.4 Use of the program

FDMNES can be freely downloaded as a Windows executable from the Institut Néel website [59]. The program has been developed to be simple to use, requiring only an input data file containing the crystal structure and calculation instructions. An example input file has been included in appendix B. The primary variables in the calculation are the locations of atoms within the unit cell, and the radius at which the final states are calculated, where a larger radius will provide more accurate results but be more costly of time. The program will run on most computers, with simple calculations usually taking anything from a few minutes to several days on a dual-core laptop. More complex calculations can be performed using a computer cluster and the code can run in parallel for this.

3.2.5 Comparison to experiment

As described above, FDMNES can calculate the cross sections of scattered radiation from resonant x-ray processes. This means that energy and azimuthal line spectra can be produced to compare directly to experimental data. In reality, the certain experimental calibration factors have to be employed to achieve agreement, such as a scaling factor for the intensity and a small offset in energy. The parameters of the calculation can also lead to varying results as the convergence of the final states may vary depending on what radius has been chosen.

FDMNES has been used successfully in previous experiments in helping to interpret the electronic properties of materials, most notably in oxide materials [66, 67].

Chapter 4

Crystal Structures

4.1 Abstract

Single crystal diffraction is performed on samples of Na_xCoO_2*,* $Na_xCa_yCoO_2$ *and* $Na_xSr_yCoO_2$ *using neutrons on SXD and x-rays at Royal Holloway. All three systems demonstrate previously unobserved superlattice patterns. Refinements of the principal Bragg peaks provide information on the occupancies of sodium and dopant sites, and Reverse Monte Carlo (RMC) techniques are employed to solve the sodium layer ordering and atomic displacements. RMC results for* $Na_{0.8}CoO_2$ *give ordered stripes of tri-vacancy clusters, consistent with previous modelling, and also show buckling in the Co layer that follows the patterning of sodium ions. For* $Na_{0.57}Ca_{0.14}CoO_2$ *we find a di-vacancy structure where the calcium ion sits at the central site. Two different superlattice phases were observed in* $Na_xSr_yCoO_2$*, both requiring large supercells and exhibiting intense peaks away from the principal Bragg reflections. Through a process of RMC and intensive manual modelling, these structures are shown to comprise of ordered Sr ions in large multi-vacancy clusters.*

4.2 Background

Previous diffraction studies have revealed a kaleidoscope of superlattice patterns in reciprocal space as a function of sodium concentration, x and temperature [68, 50]. These superlattice patterns were originally thought to be incommensurate due to their complex patterns [68], however it was shown by Morris et al. that the peaks would lie on a commensurate hexagonal grid of a^*/N, where N is an integer, and be caused by ordering of the sodium ions into long range superstructures [69]. Forward Monte Carlo calculations by Michel Roger from CEA, Saclay, revealed vacancy ordering in the sodium layers [70], leading to the formation of vacancy clusters, where a sodium ion would be promoted to a Na1 site (red sites in figure 1.3) and be surrounded by vacancies. Using the short range repulsion of ions and a long-range Coulomb potential to model the sodium ions and vacancies within the plane, an electrostatic theory was developed that established the formation and long range ordering of vacancy clusters. Vacancies within the sodium plane can be considered as negative charges that repel each other by Coulomb repulsion. As the concentration of vacancies increases, they are forced closer together. By promoting a sodium ion from a Na2 site (blue in diagrams) onto a less energetically favourable Na1 site (red), vacancies can move together and by reducing the total surface energy, stabilise multi-vacancy clusters as demonstrated in figure 4.1. These vacancy clusters order into long range patterns and the scattering from this long range ordering creates a superlattice of peaks in reciprocal space.

A number of these superstructures observed through diffraction techniques have now been solved, including the structure of $Na_{0.5}CoO_2$ [71] which comprises alternating stripes of Na1 and Na2 sites. In the region $0.7<x<0.85$, particularly rich superlattice patterns have been observed, including 6-fold or 12-fold rings of satellite peaks as well as the hexagon-of-hexagons structure [50, 72, 73]. Phase coexistence has also been reported between different compositions [74, 75]. Solving the

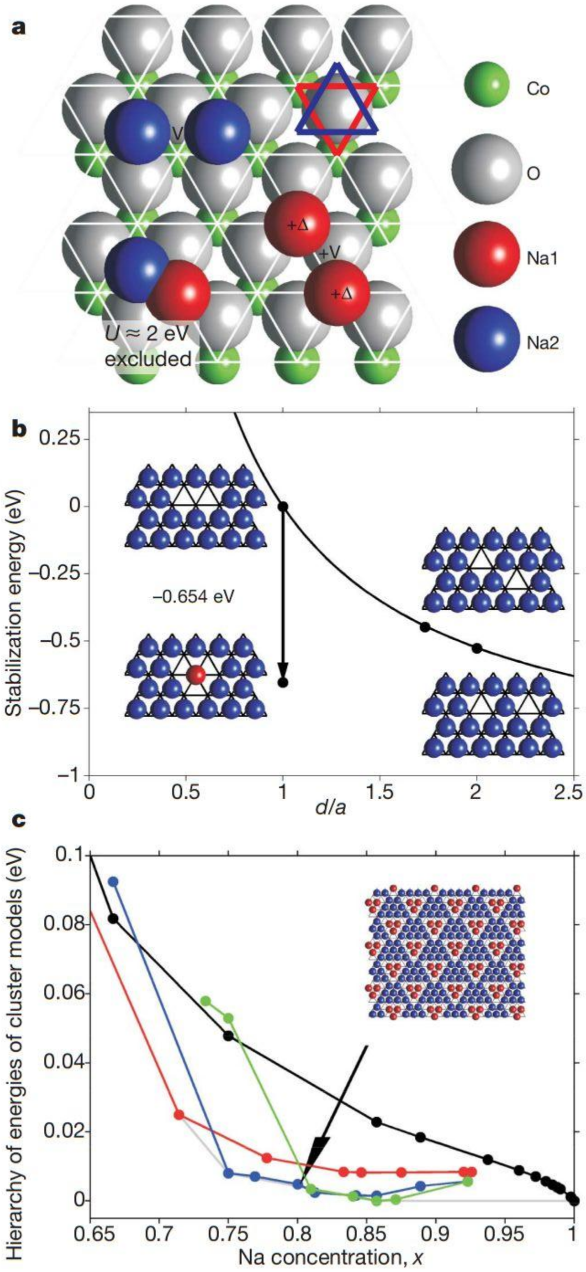

Figure 4.1: Sodium ordering principles, taken from figure 1, ref. [70]. **(a)** Sodium can sit on one of two possible sites, red sites have higher energy due to short range repulsion from cobalt. **(b)** When vacancies are next to each other, surface energy can be lowered by promoting a blue Na2 site onto a red Na1 site, stabilising the multi-vacancy cluster. **(c)** Calculations of the energy of ordered arrays of mono-vacancies (black), di-vacancies (red), tri-vacancies (blue) and quadri-vacancies (green). Co-existence between phases can occur between certain fractional fillings due to the interchanging hierarchy of energies.

structures that lead to these complex diffraction patterns has proven a particularly difficult task, with various methodologies, including theoretical works, appearing in the literature [76, 77, 73, 78, 79, 80]. Perhaps the most successful method was developed by Michel Roger, who was first to apply Reverse Monte Carlo methods to single crystal x-ray diffraction data on the high-x compositions [12].

By indexing the superlattice peaks on a commensurate grid, the size of supercell and superlattice vectors could be obtained. The intensities would then be used to generate the sodium ordering using the RMC code. In this way it was found by Morris *et al.* that the high-x structures could form in either a square or striped arrangement of tri-vacancy clusters, where conversion between the two structures requires two shear transforms, as shown in figure 4.2. The hexagon-of-hexagons structure was found to be a coexistence of these two phases, producing two separate but overlapping superlattices in reciprocal space.

However, the diffraction patterns could not be fully explained by the ordering of sodium ions. The electrostatic potential created by the vacancy clusters was found to create a distortion field that would lead to periodic buckling of the cobalt layers [70]. To obtain the best agreement with the observed modulation of intensities, especially in the high-L planes in reciprocal space, these distortions were required. The buckling of cobalt ions could be applied to a model using a single force constant, allowing a single parameter to fit the model with. This was an important factor in reproducing the diffraction patterns for the square and stripe phases mentioned above [76].

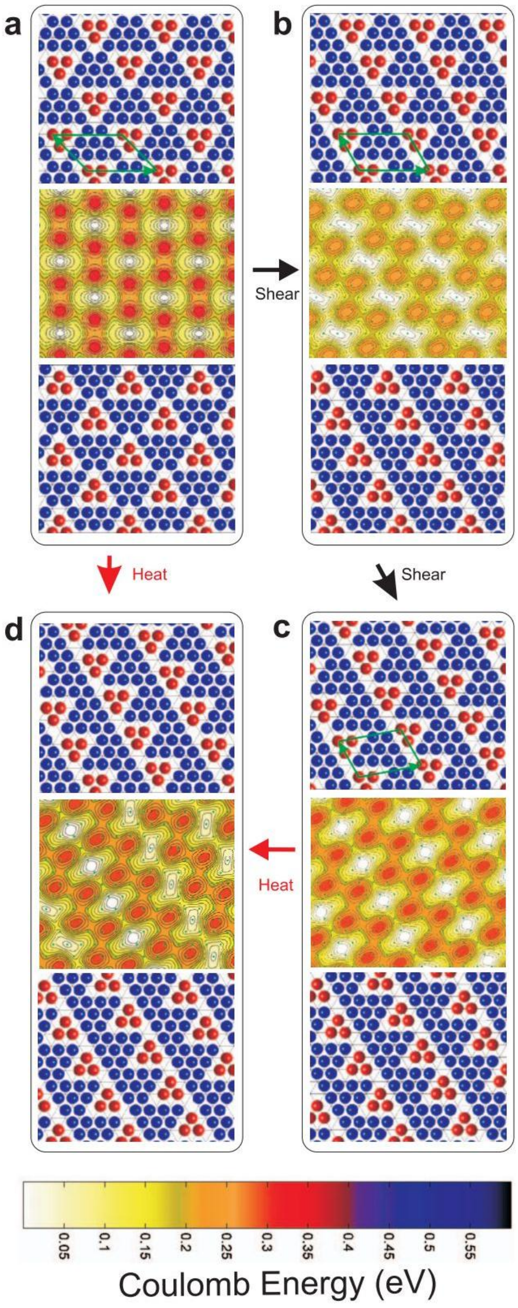

Figure 4.2: Conversion between square and stripe phase of $x = 0.80$ tri-vacancy system, from figure 2, ref. [50]. Each panel shows the ionic ordering in adjacent sodium layers, and the Coulomb landscape this ordering generates in the intervening cobalt layer. Panel **(a)** shows the square phase of tri-vacancies observed in $Na_{0.75}CoO_2$ at low temperature and panel **(c)** shows the ordered stripe phase observed in $Na_{0.78}CoO_2$. Two shear distortions along the supercell axis transform between the two phases. The high temperature phase of randomly ordered stripes is shown in panel **(d)**.

Figure 4.3 shows that the thermoelectric power factor increases as the number of holes decreases and x increases. However in the high-x region, phase separation occurs and this leads to a reduction in the power factor due to phase coexistence with the insulating $x = 1$ phase [7]. In order to increase this limit on the thermoelectric properties of this system it is important to decrease the number of holes, and this can be performed by doping the sodium layer with divalent ions. Doping with Ca^{2+} and Sr^{2+} has shown improvements to the power factor due to a large enhancement of the Seebeck coefficient, as illustrated in figures 4.4 and 4.5. In both cases the initial improvement of the power factor decreases as the dopant concentration increases. However, single crystal diffraction studies have not been performed on these systems until now.

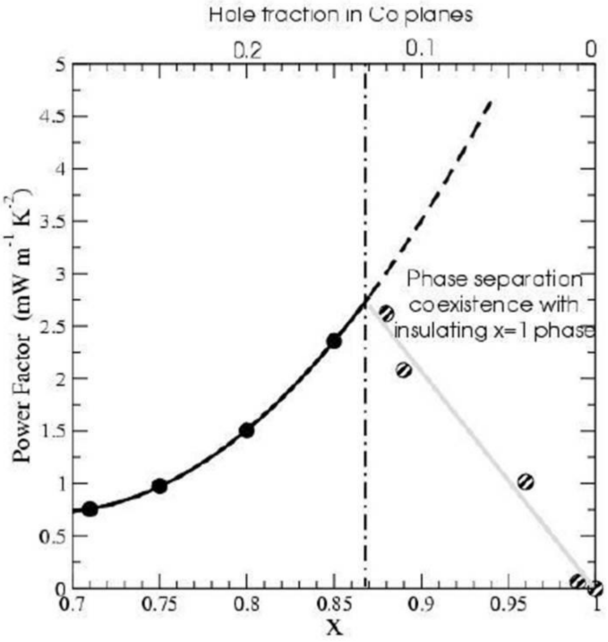

Figure 4.3: Increasing the sodium concentration, x, leads to greater power factors until $x \approx 0.86$, when phase coexistence with the insulating $x = 1.0$ phase reduces this value. From figure 4, ref. [7]

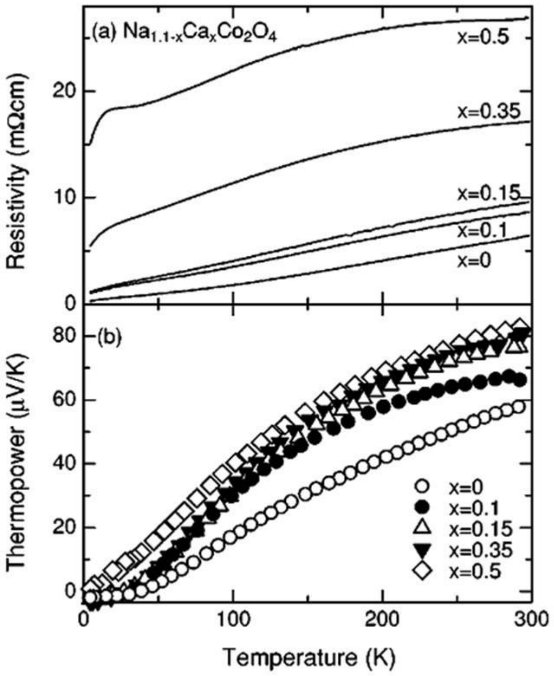

Figure 4.4: Doping with various concentrations of calcium leads to higher values of the Seebeck coefficient (thermopower), however at increased calcium content, x, the resistivity increases, reducing the power factor. From figure 3, ref. [81]

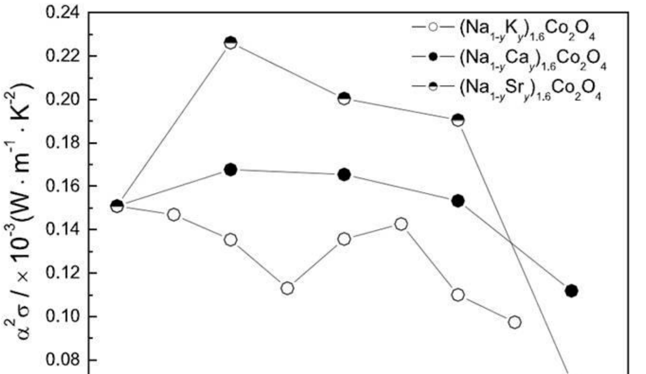

Figure 4.5: Power factor of $(Na_{1-y}M_y)_{1.6}Co_2O_4$ for different dopants with dopant fraction, y, showing the increase in power factor with small doping of divalent ions. From figure 5, ref. [82]

4.3 Experimental Procedure

4.3.1 Neutron Measurements on SXD

Boules of various compounds of Sodium Cobaltate were grown using the floating zone technique either at Oxford University by Dr D. Prabhakaran or at Royal Holloway by Dr S. Uthayakumar [47, 83]. We attempted to determine the composition of each boule by measuring small fragments using Energy-dispersive X-ray spectroscopy (EDX). EDX is only sensitive to the surface of the sample and it was found that scanning along the surface varied the compositions significantly around the nominal growth compositions, presumably due to loss of sodium from the surface in air. The boules were screened using neutrons on SXD at ISIS, allowing us to find large single grains within the growths. Table 4.1 shows several large single crystals that were found through this screening process and have been used in the following experiments. The largest $Na_{0.8}CoO_2$ crystal had remarkably strong and sharp reflections with an average mosaic spread in all directions of $0.05Å^{-1}$. This was easily the largest single crystal of Sodium Cobaltate grown to date. Once a single crystal with large principal Bragg peaks was found, longer exposures of 3-6 hours were taken at several different orientations, allowing a large portion of reciprocal space to be mapped. Each sample was measured at several temperatures using the standard SXD sample environment, which gives a temperature range between 40K and 300K. Additional environments were often used with alternative temperature ranges, such as the low temperature cryostat that can reach 5K or the furnace, which is able to heat the sample to 600K. High temperature measurements were made on each of the systems to observe the temperature at which the superlattice peaks disappeared, indicating that the sodium ions had become disordered.

Data from the 11 area detectors on SXD were analysed using the instrument software SXD2001, which is able to find peaks in the time-of-flight data and fit

	Composition	Growth Location	Mass (g)	Size (mm)	Volume (mm^3)
1	$Na_{0.8}CoO_2$	RHUL	1.036	26.3 × 5.9 × 2.6	403
2	$Na_{0.8}CoO_2$	Oxford	0.100	13.0 × 6.0 × 0.5	39
3	$Na_{0.7}Ca_{0.1}CoO_2$	Oxford	0.047	4.9 × 2.6 × 1.2	15
4	$Na_{0.7}Sr_{0.1}CoO_2$	Oxford	0.024	4.8 × 3.0 × 0.6	9

Table 4.1: Single crystal properties for neutron measurements

these peaks to an orientation matrix. This software was also used to visualise the data as two-dimensional cuts through reciprocal space and to integrate the observed principal and superlattice reflections.

4.3.2 X-ray measurements on Xcalibur

The size of single crystal required for lab based x-ray measurements is usually <0.5mm, which is much smaller than the crystals required for neutron scattering. It was possible therefore to find single crystals from multiple compositions of the doped systems, the various samples measured are described in table 4.2. The diffractometer uses a single area detector placed close to the sample. Large volumes of reciprocal space were mapped out by measuring many orientations of the sample. Each sample was measured for several hours with an exposure time of 10s per orientation, and typically several hundred orientations were required to accumulate good coverage of reciprocal space. The lab x-ray diffractometer does not currently have any ability to control temperature, and therefore only room temperature results could be obtained.

Each data set was analysed using $CrysAlis^{Pro}$, a commercial program built specifically for this type of diffractometer. This program dealt with peak searching, orientation matrices, data visualisation and integration, just as SXD2001 was used for SXD.

	Composition	Growth Location	Size (mm)	Volume (mm^3)
5	$Na_{0.8}CoO_2$	RHUL	0.34 × 0.14 × 0.01	0.001
6	$Na_{0.7}Ca_{0.1}CoO_2$	RHUL	0.55 × 0.28 × 0.02	0.003
7	$Na_{0.57}Ca_{0.14}CoO_2$	RHUL	0.57 × 0.18 × 0.02	0.001
8	$Na_{0.6}Ca_{0.2}CoO_2$	RHUL	0.40 × 0.17 × 0.04	0.003
9	$Na_{0.7}Sr_{0.1}CoO_2$	RHUL	0.64 × 0.18 × 0.06	0.007
10	$Na_{0.6}Sr_{0.2}CoO_2$	RHUL	0.29 × 0.16 × 0.08	0.004
11	$Na_{0.48}Sr_{0.32}CoO_2$	RHUL	0.54 × 0.17 × 0.13	0.012

Table 4.2: Single crystal properties for x-ray measurements

4.3.3 Structure refinement

The main hexagonal reflections from the neutron and x-ray data were integrated using SXD2001's Shoebox method or using the standard integration in $CrysAlis^{Pro}$. The various correction factors were determined (see section 2.1.6) and a refinement was performed using JANA2006. The program automatically selected the space group $P6_3/mmc$ which is consistent with previous refinements of Sodium Cobaltate [5, 84, 77]. Four atomic positions were used, including cobalt, oxygen and the two sodium sites as described in table 4.3. A systematic process of refinement was followed, slowly allowing a greater number of structural parameters to vary, with the final refinement including the occupancy of sodium and harmonic thermal parameters.

Atom	Position			Site	Sym.	Occupancy	Uiso
Co	0.0000	0.0000	0.0000	2a	-3m	1.00	0.010
O	0.3333	0.6667	0.0908	4f	3m	1.00	0.010
Na1	0.0000	0.0000	0.2500	2b	-6m2	x	0.010
Na2	0.6667	0.3333	0.2500	2d	-6m2	y	0.010

Table 4.3: Initial parameters for refinements in JANA2006.

A fundamental problem occurs when refining the sodium and dopant occupancies of the calcium and strontium doped systems. Occupation of Na1 and Na2 sites by divalent ions is strongly correlated with concentrations x and y, and these are not precisely known. In this case some physical constraints are considered. This situation arises because both elements can contribute to the scattering from a particular site and the form factor is a result of the sum of their occupancies. It is possible to assign any occupancy to sodium, provided the dopant occupancy on a single site leads to the observed form factor. In principle, this ambiguity is removed by the different Q dependencies of the form factors for the various ions in the case of x-rays. However, practically this did not resolve this issue. In these refinements I have made the assumption that sodium ions sit on the Na2 sites and dopant ions sit on the Na1 sites. This assumption was tested during the refinement process by placing the dopant on the Na2 site and seeing how this affected the fit.

4.3.4 Reverse Monte Carlo

The RMC program described in section 3.1 was used to model structures consistent with these diffraction patterns. Before the program could be run however, reliable peak intensities were required but because of the weak scattering from superlattice peaks in these systems, it was realised that the standard methods of integration provided by SXD2001 and $CrysAlis^{Pro}$ were unable to produce reliable estimates of the superlattice peak intensities. An alternative manual method was used, therefore, that was not reliant on finding the peak centre or fitting the peak shape. In this simple method, the counts within pixels in an area around a predicted superlattice position were summed up with the background removed (the background is defined as the average of the pixel counts at the edge of the area). The errors on each peak were defined by assuming standard Poisson counting statistics and given as the square root of the total sum of the pixel counts, without the background subtracted. This method has the advantage of being able to count extinctions as well as peaks, which is important as the extinctions can provide a more definite constraint on a given model than a non-zero intensity. The integration was performed over the entire coverage of reciprocal space, and any erroneous points that did not reproduce the observed scattering were removed. The erroneous points were found by directly comparing the integrated intensity with cuts through the data. The integration data and calculation parameters for each system are given in table 4.4.

Composition	Data type	Reflections	$\underline{\mathbf{a}}'$	$\underline{\mathbf{b}}'$	N_c	n_d
(1) $Na_{0.8}CoO_2$	Neutron	5780	$3\underline{\mathbf{a}}$	$4\underline{\mathbf{a}} + 5\underline{\mathbf{b}}$	15	5438
(2) $Na_{0.8}CoO_2$	Neutron	271	$-\underline{\mathbf{a}} + 3\underline{\mathbf{b}}$	$4\underline{\mathbf{a}} + 3\underline{\mathbf{b}}$	15	-72
(7) $Na_{0.57}Ca_{0.14}CoO_2$	X-ray	2216	$2\underline{\mathbf{a}} - \underline{\mathbf{b}}$	$\underline{\mathbf{a}} + 3\underline{\mathbf{b}}$	7	2060
(9) $Na_{0.7}Sr_{0.1}CoO_2$	X-ray	2182	$5\underline{\mathbf{a}} + 10\underline{\mathbf{b}}$	$10\underline{\mathbf{a}} + 5\underline{\mathbf{b}}$	75	472
(10) $Na_{0.6}Sr_{0.2}CoO_2$	X-ray	879	$3\underline{\mathbf{a}}$	$8\underline{\mathbf{a}} + 10\underline{\mathbf{b}}$	30	195

Table 4.4: Integration data for reverse Monte Carlo calculations, where N_c is the number of unit cells in the supercell and n_d is the number of degrees of freedom (the data points minus the number of free parameters). The unit cell vectors are defined as: $\underline{\mathbf{a}} = (a, 0, 0)$, $\underline{\mathbf{b}} = (-a/2, a\sqrt{3}/2, 0)$, $\underline{\mathbf{c}} = (0, 0, c)$, where a and c are the lattice parameters, nominally $a = 2.85$Å and $c = 10.8$Å.

For each system, 20,000 movement iterations were performed at each of the 200 temperature steps. The starting temperature was defined at a value at which thermal equilibrium is reached, where any movement is allowed. This temperature was found through trial calculations. As described in section 3.1, each movement step consists of a sodium ion hopping to an unoccupied site, a dopant attempting to switch with a sodium and an incremental movement for any atom type. Each movement is stored if it makes the fit with experimental data better, or with a probability dependent on the current temperature of the system, obeying a standard Boltzmann temperature distribution. Each calculation is performed numerous times with different random number seeds to check the consistency of the solution.

4.4 Results

4.4.1 Na_xCoO_2

The Royal Holloway $Na_{0.8}CoO_2$ crystal was mounted on SXD and exposures of several hours were taken at 300K, 250K and 5K. Figure 4.6 shows two dimensional cuts through the $(h, k, 4)$ plane that show the change of ordering in the system. At 300K there is a six-fold ring of satellite peaks around the main hexagonal reflections, where the separation between hexagonal reflection and superlattice peak is 1/5th of the distance between hexagonal positions. At 250K and 5K the six-fold ring of satellite peaks was still there but additional peaks were found, creating a complex arrangement of triangles around each hexagonal peak. These new peaks lie on a commensurate hexagonal grid, where the length of each element is 1/15th of the hexagonal lattice unit length. The complete pattern can be reproduced using a supercell with the following unit vectors:

$$\underline{\mathbf{a}}' = 3\underline{\mathbf{a}}$$

$$\underline{\mathbf{b}}' = 4\underline{\mathbf{a}} + 5\underline{\mathbf{b}}$$

The lattice produced by these unit vectors generates just over one third of the superlattice peaks, and the remainder are generated by symmetric domains, produced with rotations of 60° and 120°. This pattern has not previously been observed on its own and is different to the superlattice observed in previous samples of a similar composition at low temperature. This superlattice has however been observed as part of a co-existence of phases and is produced by the ordered stripe phase of tri-vacancy clusters from Ref. [50], see figure 4.2(c). Figures 4.8 and 4.9 show the full reciprocal space coverage of the high and low temperature phases, respectively.

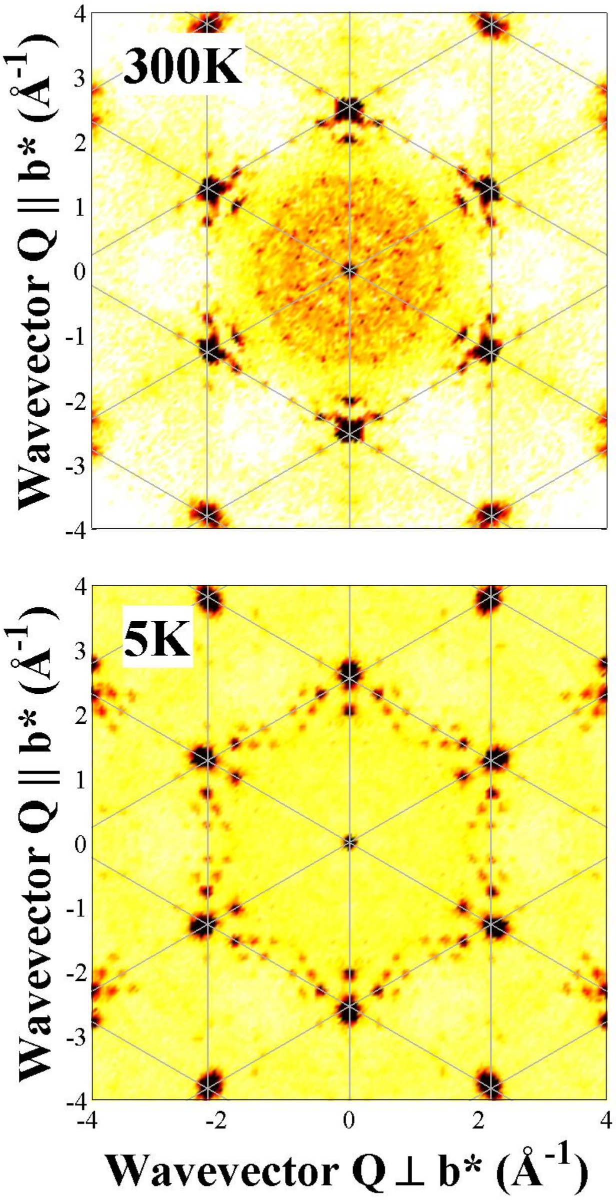

Figure 4.6: $Na_{0.8}CoO_2$ neutron diffraction data for different temperatures. Each panel is a 2D cut through reciprocal space in the $(h, k, 4)$ plane. The 300K data shows 6-fold rings of satellite peaks and the 5K data has additional peaks around those.

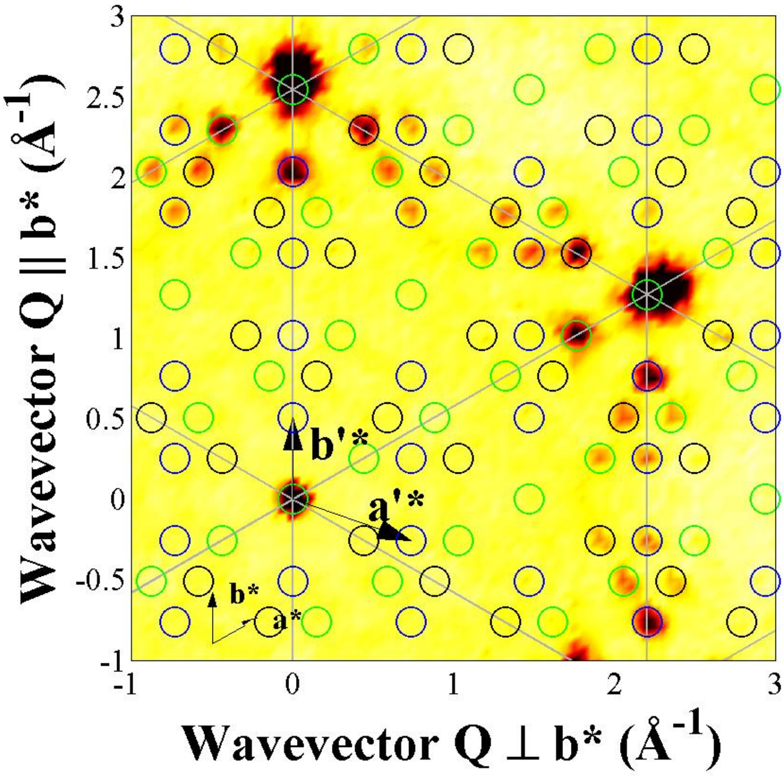

Figure 4.7: Close up of 5K neutron diffraction $(h, k, 4)$ plane. Circles show all possible superlattice positions for the ordered striped phase supercell, where different colours indicate different symmetric domains.

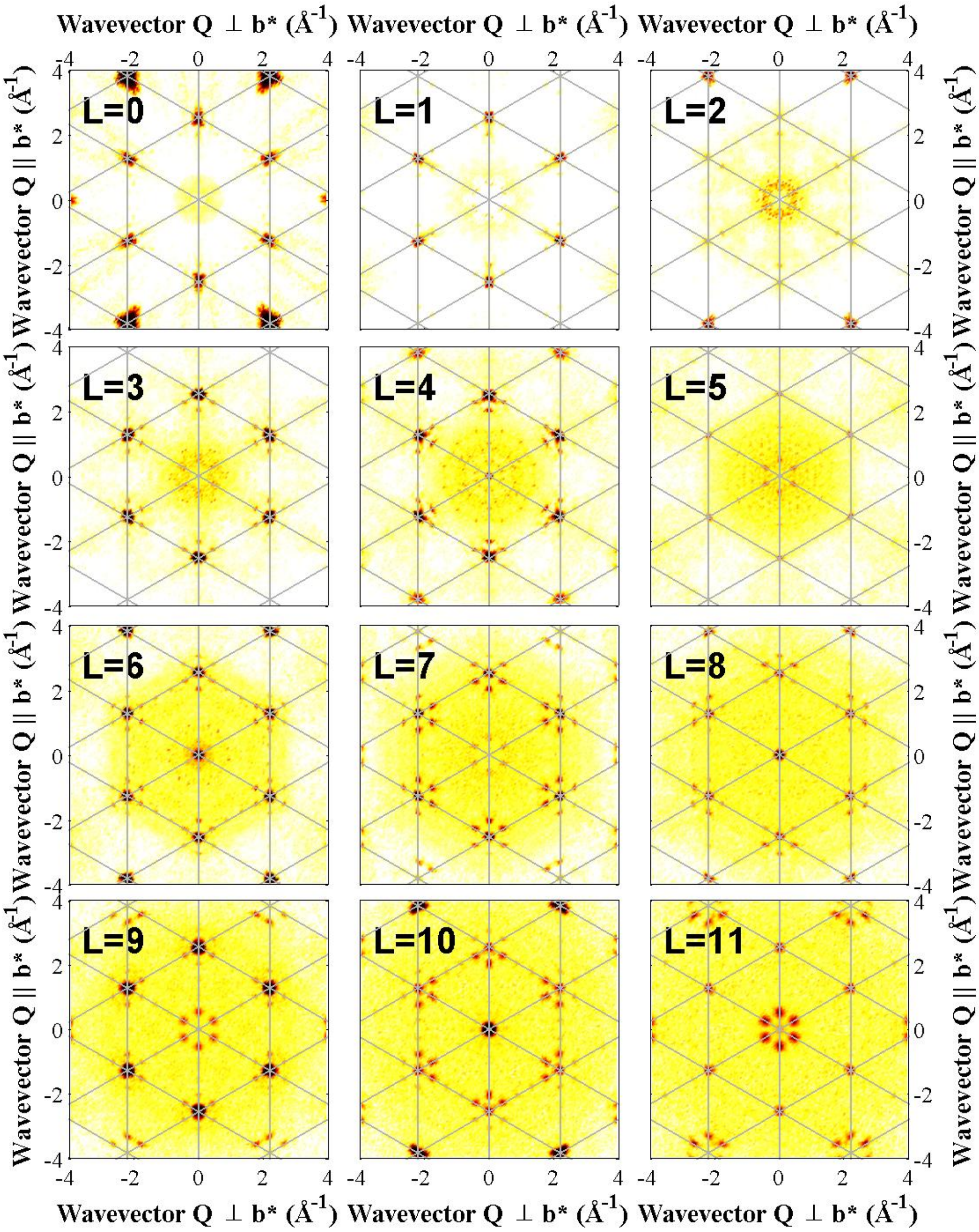

Figure 4.8: Full L-dependence of the SXD data for $Na_{0.8}CoO_2$ at T=300K

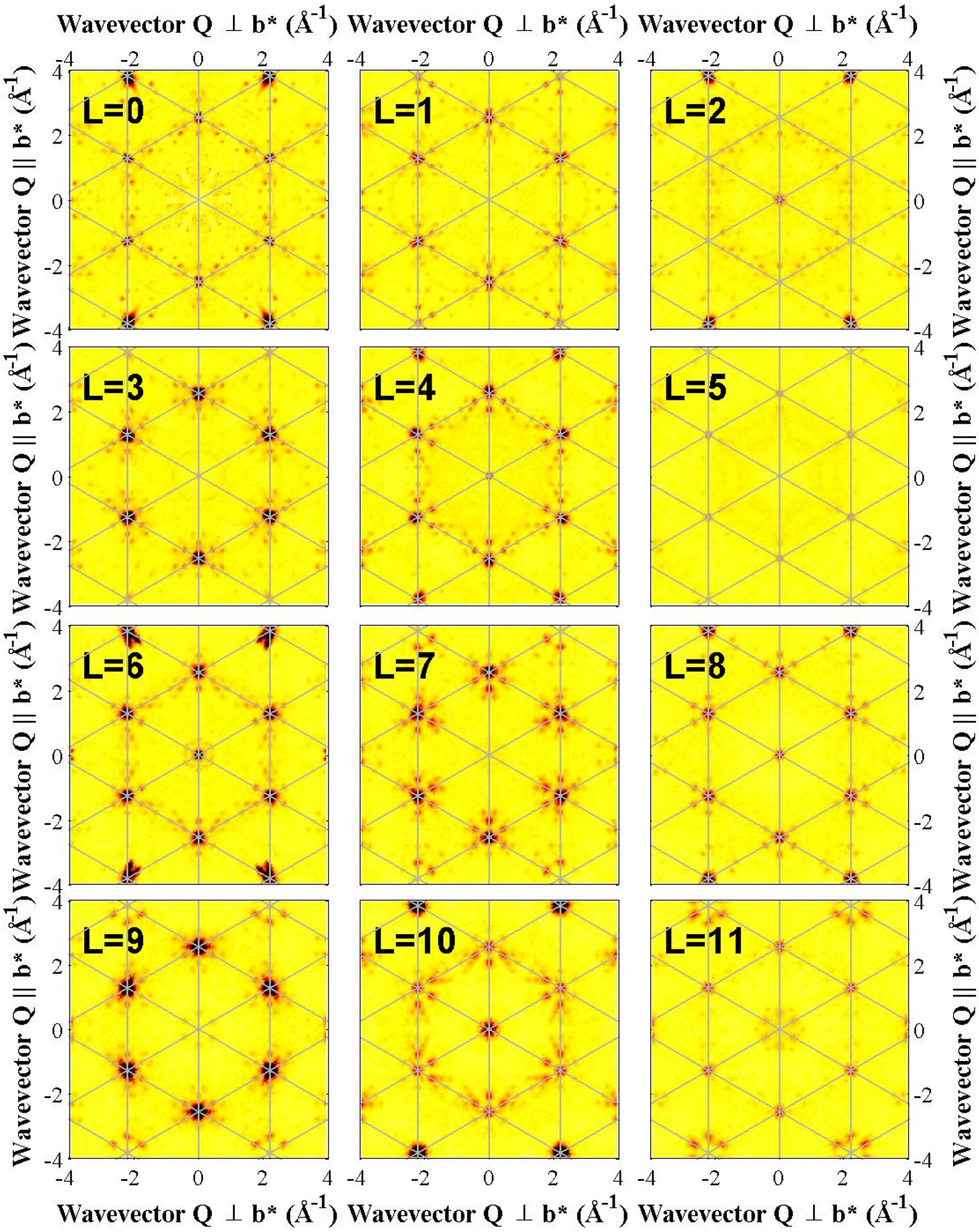

Figure 4.9: Full L-dependence of the SXD data for $Na_{0.8}CoO_2$ at T=5K

A second study was performed on a different crystal of $Na_{0.8}CoO_2$, grown at Oxford. This crystal exhibited the same superlattice pattern as the Royal Holloway sample of the same nominal composition at room temperature, but at low temperature the 6-fold rings were replaced by 12-fold rings of satellites, as shown in figure 4.10. This superlattice could be indexed using the following supercell:

$$\underline{\mathbf{a}}' = -\underline{\mathbf{a}} + 3\underline{\mathbf{b}}$$

$$\underline{\mathbf{b}}' = 4\underline{\mathbf{a}} + 3\underline{\mathbf{b}}$$

The reason for the difference in low temperature structure between the two growths is not clear at present. EDX analysis of both growth gave similar distributions of compositions along the surfaces, so it is assumed that they have the same composition. The low temperature superlattice reflections of the Oxford sample correspond to the square lattice of tri-vacancy clusters in Ref. [70], see figure 4.2(a).

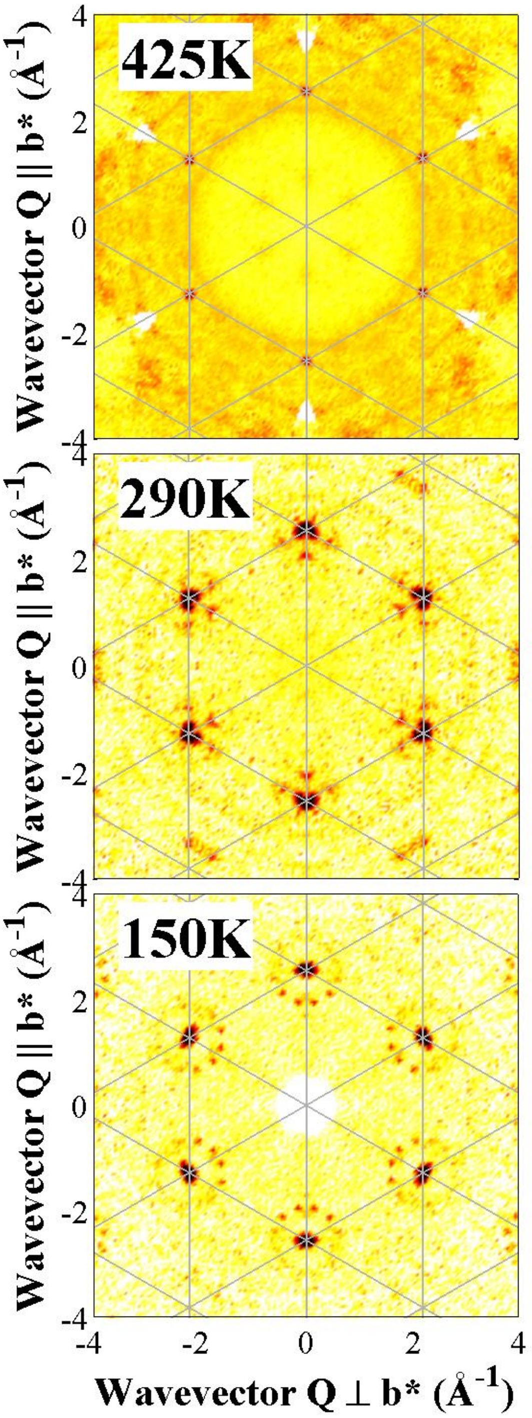

Figure 4.10: Cuts in the $(h, k, 7)$ plane for a the $Na_{0.8}CoO_2$ sample grown at Oxford, showing 12-fold rings at low temperature.

Tiny fragments of the Royal Holloway grown $Na_{0.8}CoO_2$ boule were measured using the in-house x-ray diffractometer at room temperature. Single crystals with a size of less than 0.5mm were found and full coverage of reciprocal space was mapped, using a typical exposure time of 10s, which was enough to produce good counting statistics in the superlattice peaks. Rings of superlattice peaks were observed at the same positions seen at room temperature on SXD, meaning the same high temperature phase was being observed. As well as these superlattice peaks, other phases could be seen that were not present in the neutron data, such as the strong peaks at positions directly between principal Bragg peaks and the weak ring of peaks slightly further out than the 1/5th peaks. Figure 4.11 illustrates how these additional phases can be indexed. The peaks half way between the principal Bragg reflections are due to contamination from the x-ray source with a wavelength of $\lambda/2$. The other peaks are indexed on a commensurate grid with lattice size 1/13th of the reciprocal lattice unit, with superlattice vectors:

$$\underline{\mathbf{a}}' = 3\underline{\mathbf{a}} - \underline{\mathbf{b}}$$

$$\underline{\mathbf{b}}' = 4\underline{\mathbf{a}} + 3\underline{\mathbf{b}}$$

Figure 4.12 shows the full reciprocal space coverage from this measurement for comparison with the room temperature neutron data.

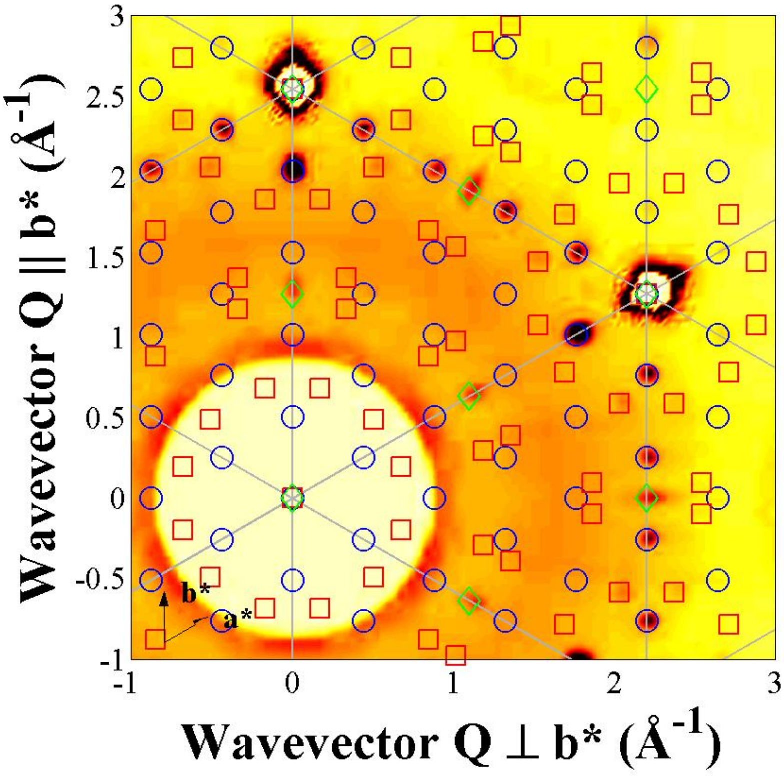

Figure 4.11: $(h, k, 0)$ layer of x-ray diffraction pattern for $Na_{0.8}CoO_2$. Different coloured shapes show the various phases observed in the system. Blue circles indicate the peaks at the 1/5th positions, green diamonds the 1/2 positions and the red squares weak peaks at the 1/13th positions.

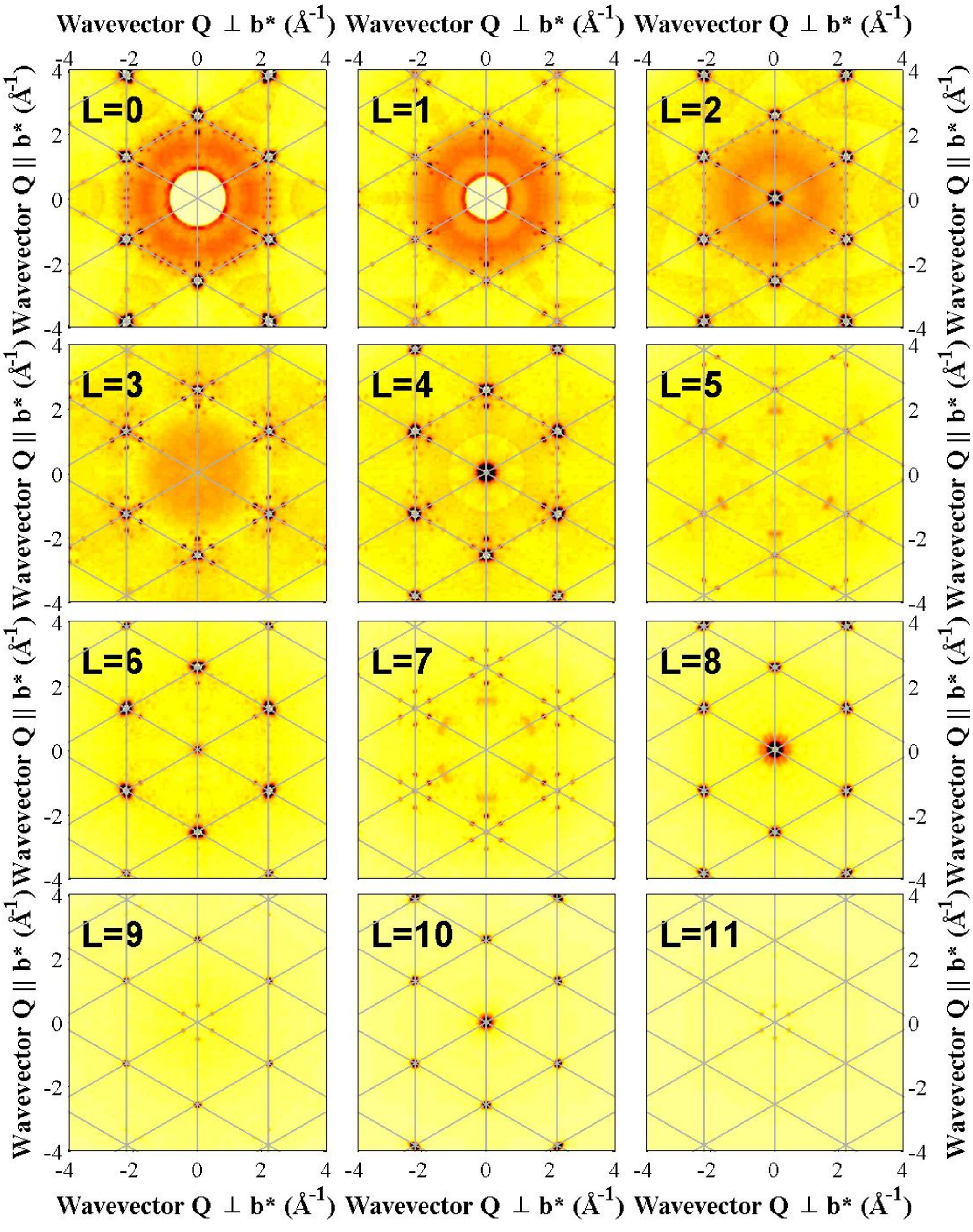

Figure 4.12: Full L-dependence of the x-ray data for $Na_{0.8}CoO_2$ at T=300K

The low temperature neutron data for the Royal Holloway $Na_{0.8}CoO_2$ crystal was integrated and refined, producing the results shown in table 4.5.

	Co	O	Na1	Na2
x/a	0.0000	0.3333	0.0000	0.6667
y/a	0.0000	0.6667	0.0000	0.3333
z/c	0.0000	0.0917(1)	0.2500	0.2500
Occupancy	1.000	1.000	0.15(3)	0.53(3)
U_{iso}	3	5	12	15
U_{11}	2.2(7)	3.5(3)	15(7)	21(3)
U_{22}	2.2(7)	3.5(3)	15(7)	21(3)
U_{33}	4(1)	6.6(5)	4(8)	2(3)
U_{12}	1.1(4)	1.7(1)	8(4)	11(1)
U_{13}	0	0	0	0
U_{23}	0	0	0	0

Table 4.5: Refinement of $Na_{0.8}CoO_2$ principal Bragg reflections from neutron data at 5K. Refinement converged at $R_w = 11.87\%$. Values with associated errors are the free parameters. Thermal parameters have units of 1×10^{-3}Å.

The fitted concentration of sodium in the system is 68(4)%, which is significantly lower than the expected 85%. The relative composition between Na1 sites and Na2 sites indicates that a small fraction of the sodium is sitting directly above the cobalt, giving evidence for vacancy clusters in the system. It can be seen from the isotropic thermal parameter, U_{iso}, that the thermal vibrations of sodium are much larger than that of either cobalt or oxygen. The harmonic anisotropic thermal parameters indicate that the vibrations of the sodium ions are pancake shaped, with larger vibrations within the plane. These in-plane vibrations are likely to arise from the presence of vacancies in the sodium plane, so that sodium ions have more room to vibrate within the plane. Figure 4.13 shows the refined average atomic structure with thermal ellipsoids showing the scale and shape of vibrations in the system.

Direct refinements of the supercells were considered, but we did not succeed in analysing these complicated superstructures using the software available.

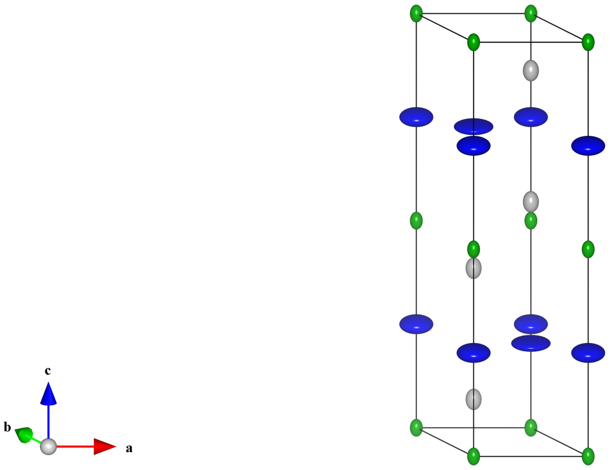

Figure 4.13: Refined average structure of $Na_{0.8}CoO_2$ from principal hexagonal reflections in SXD data at 5K. Each ball shows the anisotropic thermal vibrations refined for this model, where green balls are cobalt, grey balls are oxygen and blue balls are sodium.

The superlattice found in the Royal Holloway sample at low temperature had not been previously observed as a single phase, so RMC was used to solve the superstructure. Superlattice peaks laying on the 1/15th commensurate grid were integrated with the manual method. Peaks laying on the other commensurate lattice were ignored so that different phases could be separated. The process annealed to a single solution after many attempts with a χ^2/n_d value of 0.13 and an R_w of 42.56%, these values are consistent with a good fit to the experimental data, though the low value of χ^2/n_d may indicate that the errors have been overestimated. The solution found agrees exactly with previous work, having tri-vacancy clusters of Na1 atoms on both layers, the separation between the clusters is also the same as the previously reported structure.

The RMC calculation also presents additional information on the distortions of cobalt and oxygen ions. The RMC results show a sinusoidal distortion in the cobalt ions that follows the ordering in the sodium layers, and is very similar to the distortion model predicted by the effect of the Coulomb landscape [70]. The structure produced by RMC is illustrated in figure 4.14 and the full reciprocal space calculation is presented in figure 4.15 for comparison with the experimental data in figure 4.9.

The superlattice pattern produced by the Oxford sample at low temperature is different from the Royal Holloway sample. The same process was carried out on this data set. The solution found shows tri-vacancy clusters of sodium ions on Na1 sites, patterned in a square type arrangement. This solution appeared consistently over many calculations with a χ^2/n_d value of -43.1 and an R_w of 55.02%. The number of degrees of freedom in this system are lower than the number of datapoints, which is why the value of χ^2/n_d is negative. Ordinarily this would mean it is impossible to fit a model to the data, however the results clearly show a stable model that consistently appears. As described in section 3.1, the number of free parameters in the system is difficult to estimate and constraints on the RMC process mean that in reality the number of free parameters is much less than the value used in this estimate, which is why a realistic model can be found with so few data points. The calculated scattering is depicted in figure 4.16, for comparison with figure 6.1 in ref. [69].

The room temperature phase observed with all $Na_{0.8}CoO_2$ crystals cannot be easily modelled with RMC techniques due to the random nature of the striped ordering, however a good example of this can be modelled by building a structure of random stripes from the ordered stripe supercell. Adding together 13 supercells where the $\underline{\mathbf{b}}'$ vector can vary randomly between the three possible positions on an adjacent stripe produces a pseudo random stripe phase and the diffraction pattern produced by this, compared with neutron data in figure 4.17, does not contain any of the higher order peaks from the ordered stripe phase.

The other peaks in the x-ray data that did not fit the striped supercell were

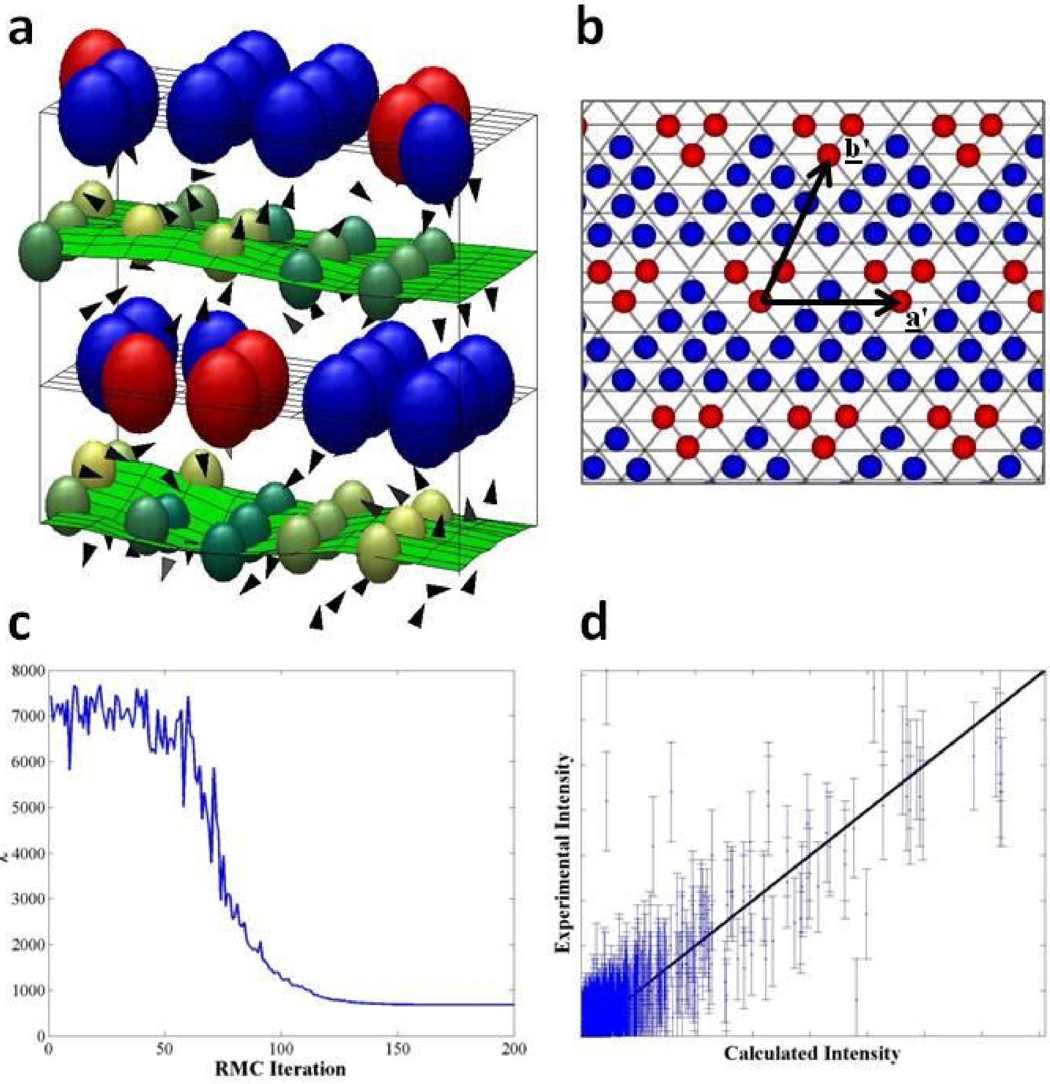

Figure 4.14: Results from the RMC calculation for the Royal Holloway $Na_{0.8}CoO_2$ neutron data. **(a)** The resultant structure, where blue balls are Na2 sodium ions, red are Na1 sodium ions, the other balls are cobalt ions, where dark green is a large negative distortion and light green is a large positive distortion. The arrows indicate the positions and distortion directions of the oxygen ions. **(b)** Top-down view of the sodium layer. **(c)** Annealing of χ^2 during the calculation. **(d)** Final comparison of calculated and experimental intensities on the right.

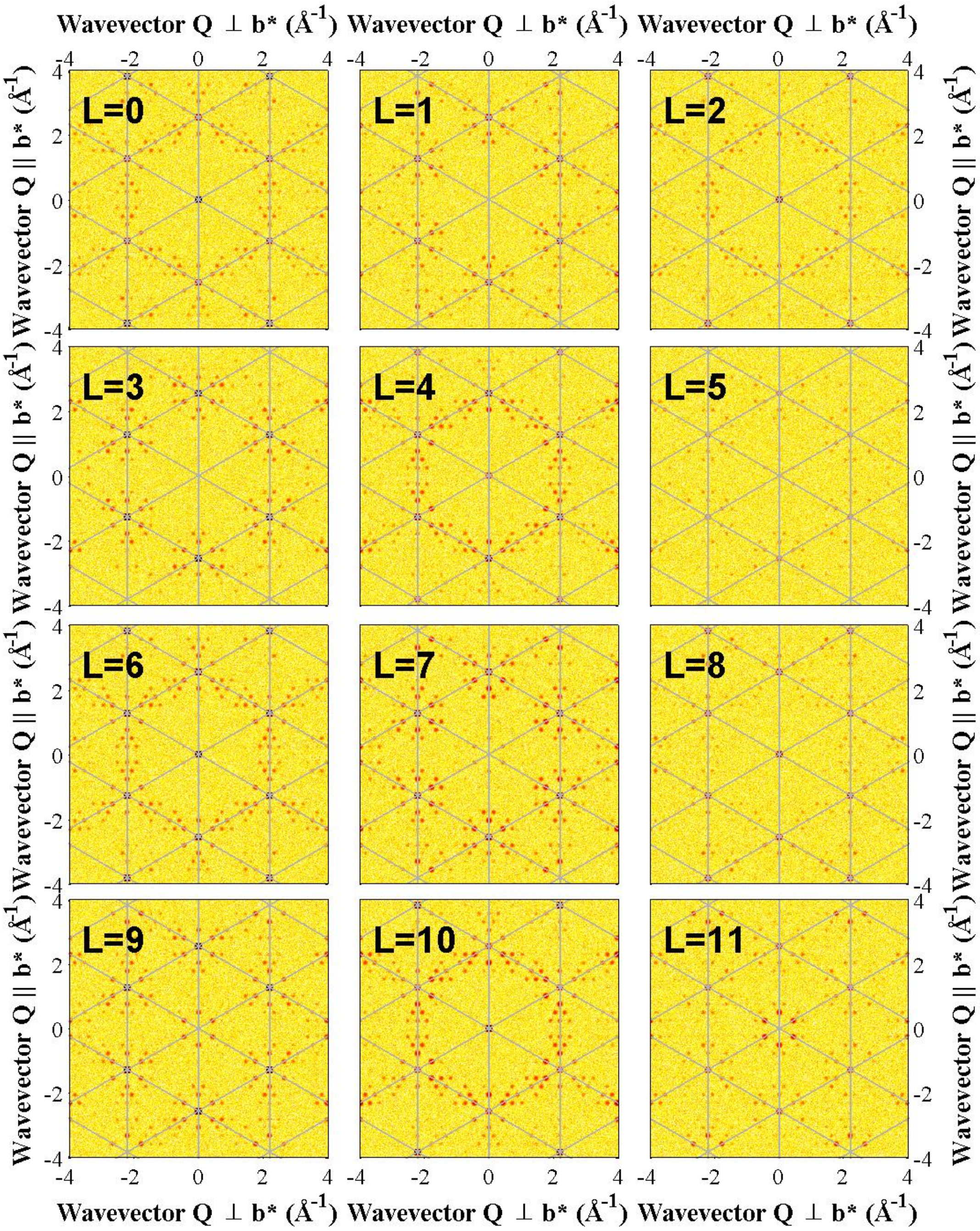

Figure 4.15: Full L-dependence for the RMC calculation of 5K Royal Holloway $Na_{0.8}CoO_2$ neutron data

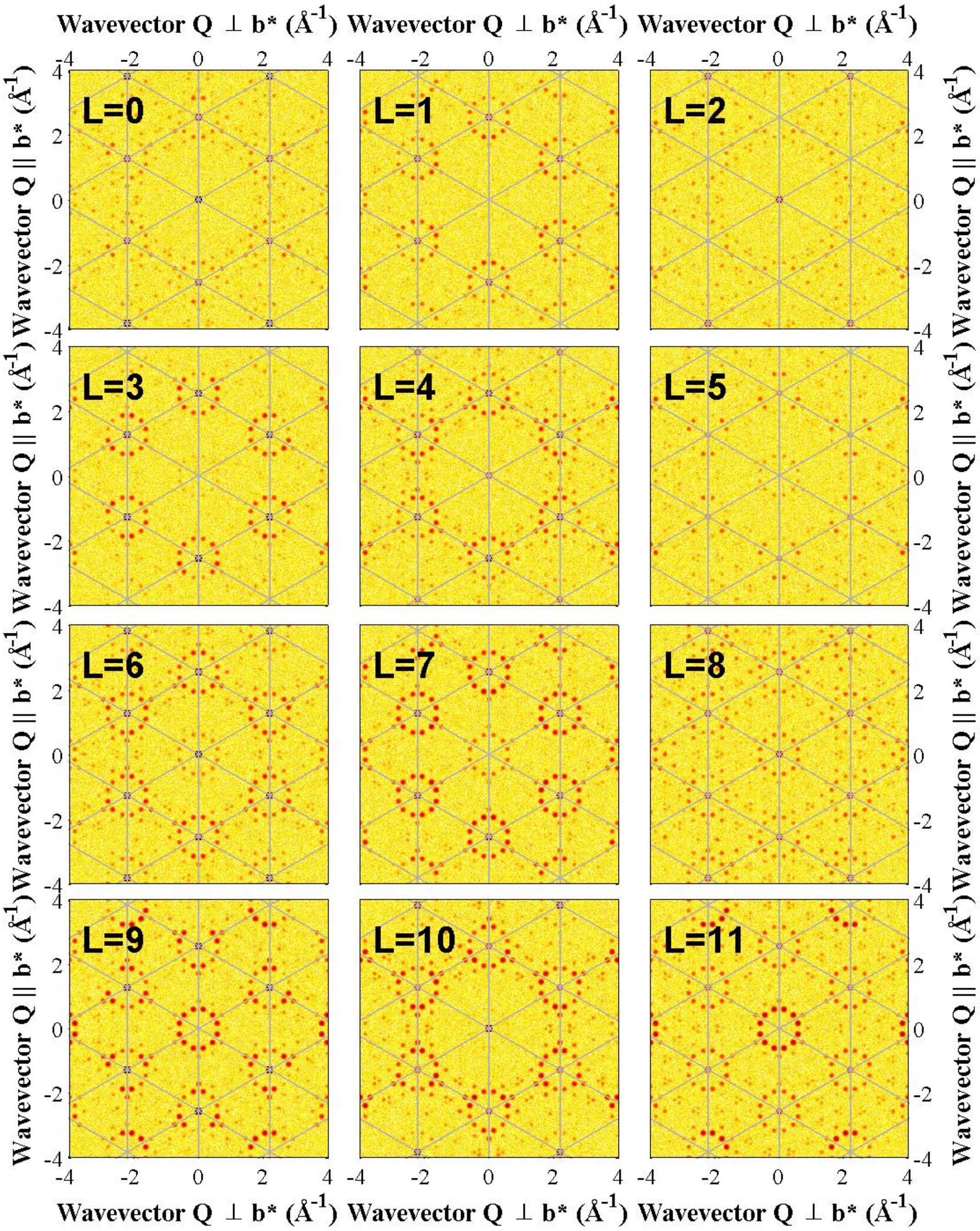

Figure 4.16: Full L-dependence for the RMC calculation of 150K Oxford $Na_{0.8}CoO_2$ neutron data

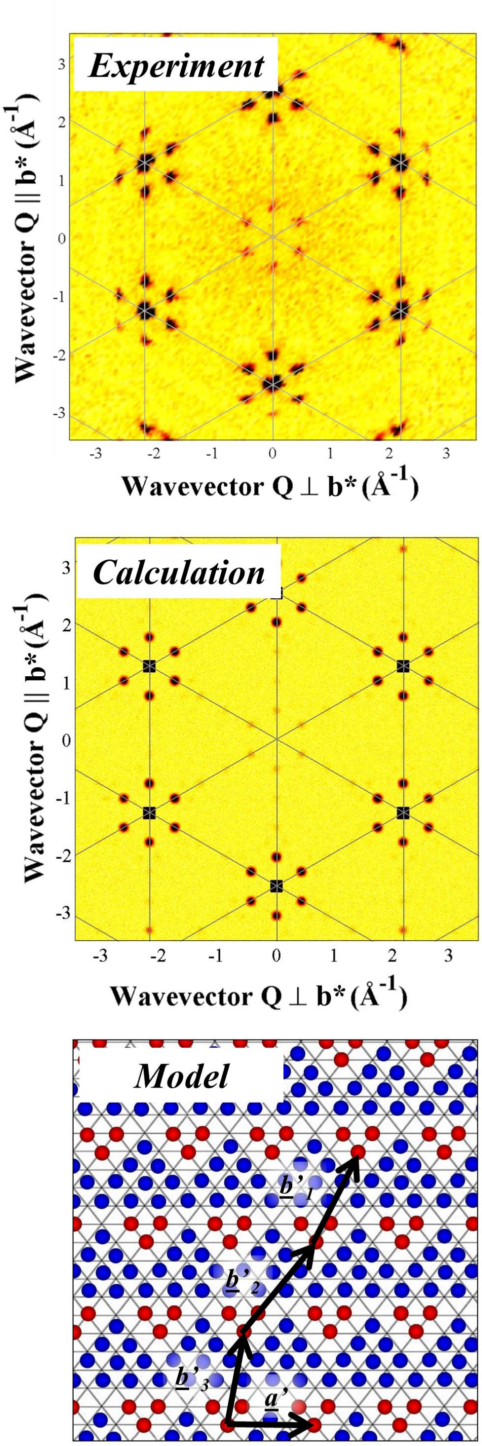

Figure 4.17: Random stripe phase calculation and comparison to the 300K neutron data set.

explained with other choices of propagation vector, as described earlier. It was not possible to use RMC on these data sets due to difficulties in integrating the peaks. The superlattice reflections at the half positions seem to be due to leakage of x-ray wavelengths at a higher order, such as $\lambda/2$. The set of superlattice reflections that sit on a 1/13th commensurate grid can be indexed in-plane using the structure first observed by Chou *et al.* [73]. However, it was found that these peaks are not located on $(h, k, integer)$ planes and are extended along the L direction. This makes it difficult to obtain peak intensities for RMC and it is not possible to solve this structure at this time due.

4.4.2 $Na_xCa_yCoO_2$

A boule of $Na_{0.7}Ca_{0.1}CoO_2$ was grown at Oxford and screened on SXD. We found quickly that the calcium doping lead to very high quality single crystals forming within the boule. A single grain with intense, sharp principal Bragg peaks was cleaved from the boule and longer exposures of several hours were taken at 350K, 150K and 40K. Other compositions of $Na_xCa_yCoO_2$ were grown at Royal Holloway and screened on SXD, but no large single crystals were found.

Due to the crystal producing such sharp reflections, satellite peaks were difficult to separate in the data, as small misaligned crystallites created a noisy background of sharp peaks. However, superlattice peaks could be found when indexed with a set of propagation vectors, and misaligned crystallites were distinguishable due to the peaks having the same magnitude of Q as principal reflections. These peaks were at different positions to those seen previously, indicating that this system had a new, previously unobserved superstructure. The superlattice pattern did not change between the three temperatures indicating a single phase present to 40K. In contrast to pure Na_xCoO_2 diffraction, this sample showed a large reduction in intensity with Q, as superlattice peaks were not observable in the high L planes.

The peaks align exactly on a hexagonal grid where the length of each element is 1/7th of the reciprocal lattice unit length. Figure 4.18 shows that the superlattice peaks can be indexed using a supercell with lattice vectors:

$$\underline{\mathbf{a}}' = 2\underline{\mathbf{a}} - \underline{\mathbf{b}}$$

$$\underline{\mathbf{b}}' = \underline{\mathbf{a}} + 3\underline{\mathbf{b}}$$

These propagation vectors index one of the two possible domains, where the second domain can be generated by a reflection in any principal axis. The full coverage of reciprocal space observed at 40K is shown in figure 4.19.

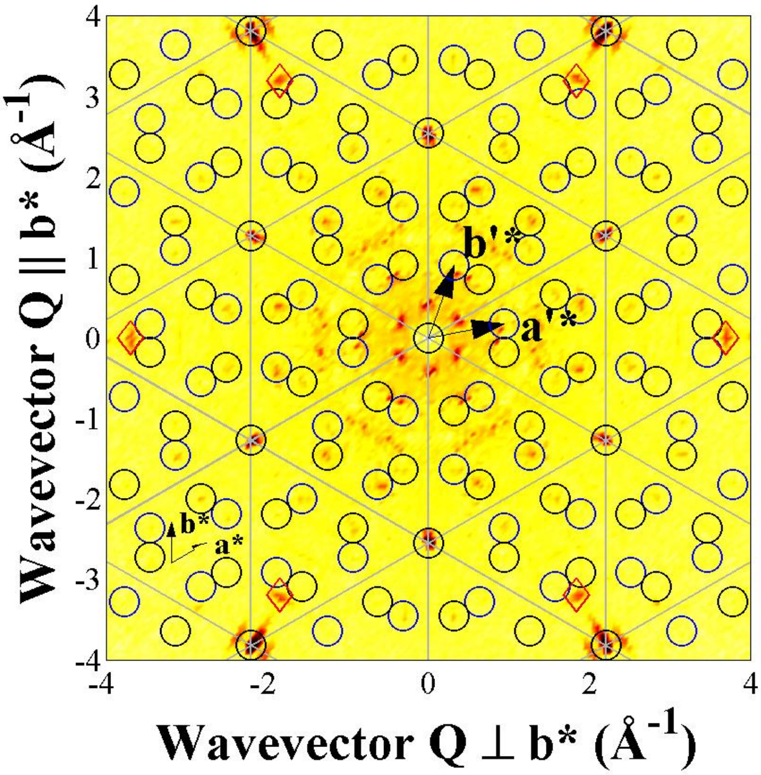

Figure 4.18: A cut in the $(h, k, 0)$ plane for $Na_{0.7}Ca_{0.1}CoO_2$ SXD data at 40K. A 12-fold ring of satellite peaks is observed around the principal Bragg reflections and these can be indexed on a hexagonal grid with spacing $a/7$. Blue and black circles show the two symmetry domains for the superlattice, and the red diamonds mark the {220} reflections of the epitaxial CaO impurity.

Additional to the satellites, peaks were observed close to the {110} principal hexagonal reflections. The d-spacing of these peaks was 3.70Å, which matches the {220} reflection of Calcium Oxide (CaO). CaO is a Face Centered Cubic (FCC) system with lattice constant $a = 4.81\mathring{A}$. For this system to produce a hexagonal pattern of points as found in these results, the (111) direction of the CaO crystal would have to be parallel to the (001) of $Na_{0.7}Ca_{0.1}CoO_2$, and the (110) direction of CaO would be parallel to the (100) of $Na_{0.7}Ca_{0.1}CoO_2$. In this direction the CaO structure can be described as successive hexagonal layers of calcium and oxygen ions with an ABC stacking sequence. Within a layer the calcium or oxygen ions are separated by $a/\sqrt{2} = 3.40\mathring{A}$, which is quite close to $2.85\mathring{A}$, the lattice parameter of Sodium Cobaltate compounds. This allows the CaO impurity to grow epitaxially within the $Na_{0.7}Ca_{0.1}CoO_2$ boule.

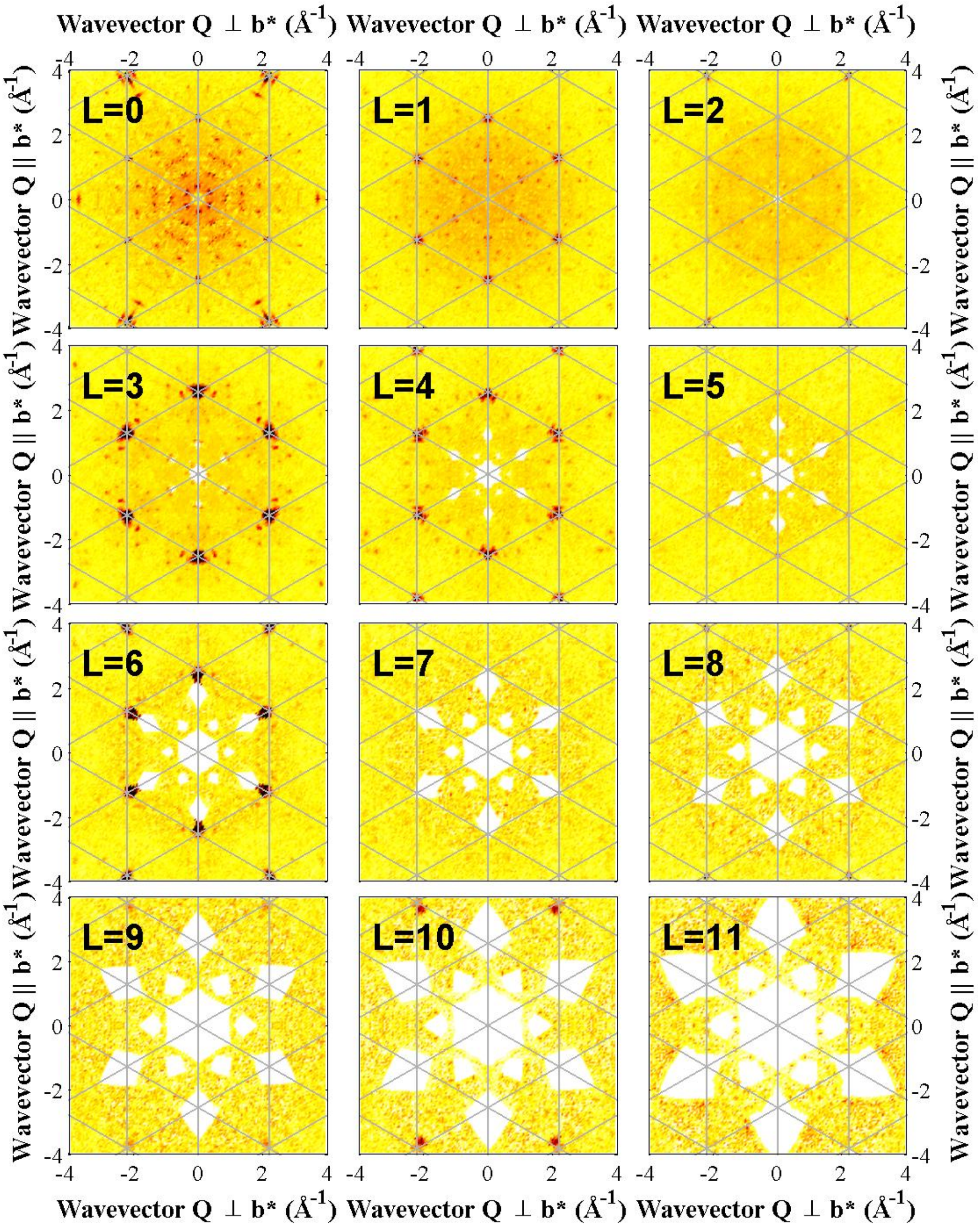

Figure 4.19: Full L-dependence of the SXD data for $Na_{0.7}Ca_{0.1}CoO_2$ at T=40K. (The white marks in high L planes are due to lack of detector coverage.)

The crystals required for x-ray diffraction are much smaller than for neutron diffraction, which allowed us to measure three compositions of the calcium doped system: $Na_{0.7}Ca_{0.1}CoO_2$, $Na_{0.57}Ca_{0.14}CoO_2$ and $Na_{0.6}Ca_{0.2}CoO_2$. Figure 4.20 shows that all three compositions exhibit a similar diffraction pattern, with superlattice peaks occurring at the same 1/7th positions as described above for the neutron data. The $Na_{0.7}Ca_{0.1}CoO_2$ and $Na_{0.57}Ca_{0.14}CoO_2$ samples have additional superlattice reflections half way between the hexagonal Bragg points, due to contamination by $\lambda/2$. The $Na_{0.6}Ca_{0.2}CoO_2$ sample also possesses these peaks as well as extra reflections near the primary superlattice rings. Figure 4.21 depicts the full L-dependence of the $Na_{0.57}Ca_{0.14}CoO_2$ system, showing remarkably strong and clear superlattice reflections.

To explain the additional peaks in the $Na_{0.6}Ca_{0.2}CoO_2$ data, a number of different supercells were attempted. The best agreement with the observed peak positions was obtained by including the model first observed in $Na_{0.5}CoO_2$ [71]. Figure 4.22 demonstrates that this supercell indexes the additional peaks but not the rings, implying a coexistence between this model and the one seen in other compositions.

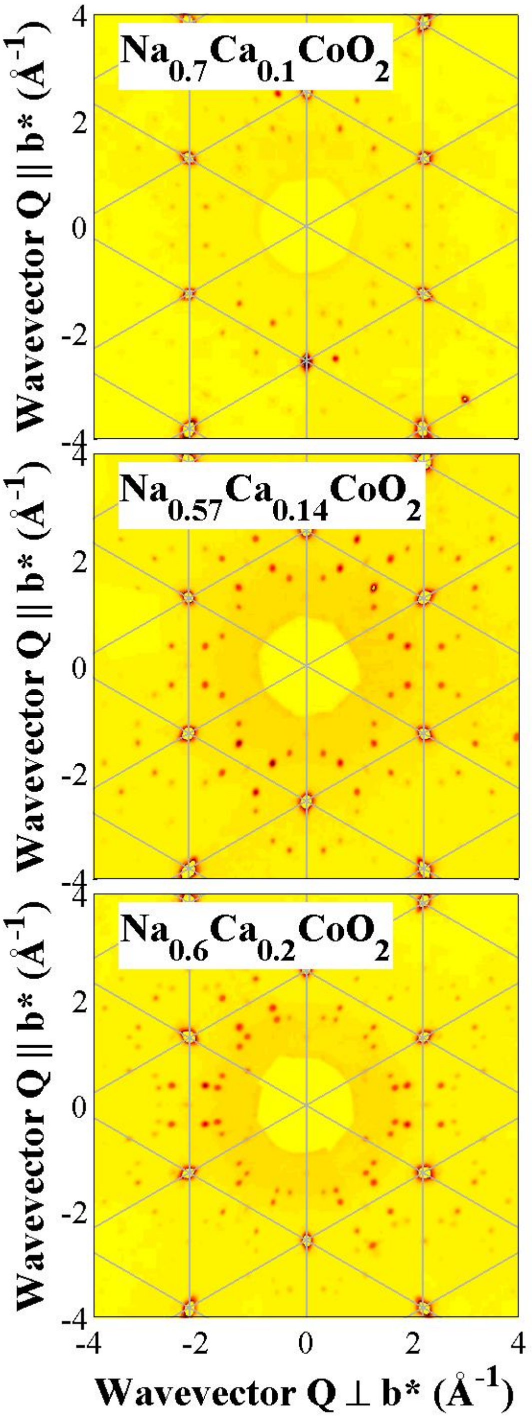

Figure 4.20: Three compositions of $Na_xCa_yCoO_2$ measured using x-ray diffraction, the $(h, k, 0)$ plane is shown at 300K.

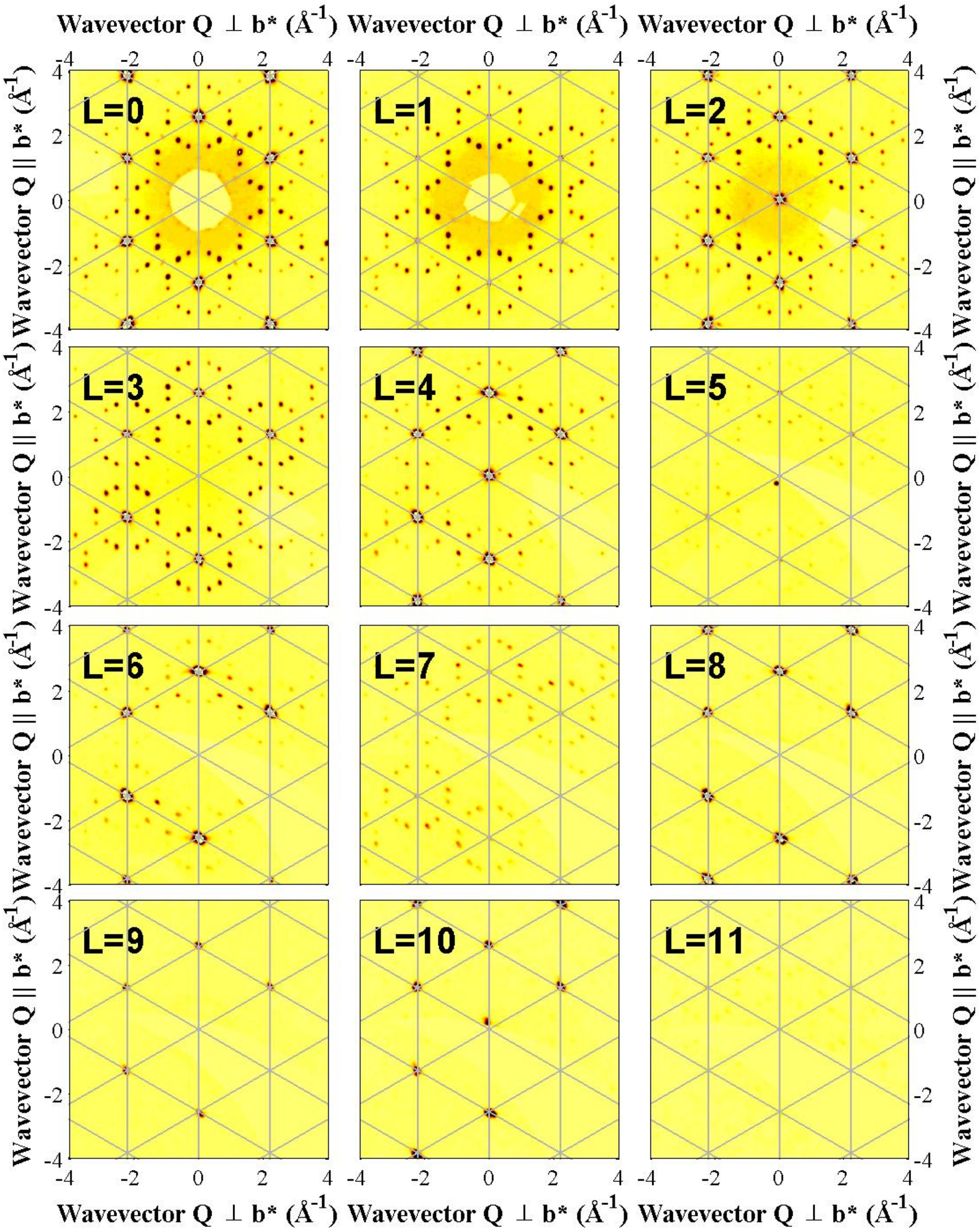

Figure 4.21: Full L-dependence of the x-ray data for $Na_{4/7}Ca_{1/4}CoO_2$ at T=300K.

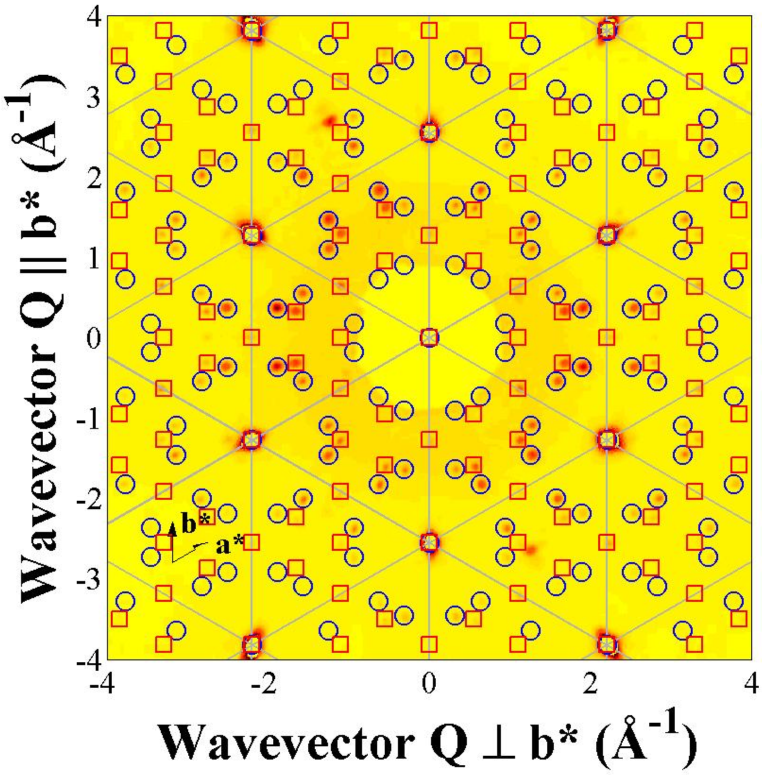

Figure 4.22: X-ray diffraction data of $Na_{0.6}Ca_{0.2}CoO_2$. Circles indicate the positions of the 1/7th superlattice and squares, the peaks at the 1/4 positions.

Integrations of the principal Bragg peaks were performed using SXD2001 for the $Na_{0.7}Ca_{0.1}CoO_2$ neutron data sets at different temperatures and by $CrysAlis^{Pro}$ for x-ray data for different compositions. The results of the refinements, as recorded in table 4.6, show that the sodium occupancies are again consistently lower than the nominal values. The calcium occupancies are much closer to the nominal values however, which is consistent with loss of the more volatile sodium ions during growth. For $Na_{0.57}Ca_{0.14}CoO_2$ the filled occupancies agree with the nominal composition, suggesting that this is a stable composition. This is consistent with the fact that the strongest, single-phase superlattice peaks are observed in this case.

		Occupancy		U_{iso}		
Composition	Temperature	Na	Ca	Na	Ca	R_w
$Na_{0.7}Ca_{0.1}CoO_2$	40K	0.55(2)	0.11(1)	0.007	0.002	6.74%
$Na_{0.7}Ca_{0.1}CoO_2$	350K	0.50(2)	0.09(1)	0.013	0.000	5.98%
$Na_{0.7}Ca_{0.1}CoO_2$	300K	0.56(1)	0.12(1)	0.019	0.013	7.84%
$Na_{0.57}Ca_{0.14}CoO_2$	300K	0.529(5)	0.138(5)	0.010	0.005	3.96%
$Na_{0.6}Ca_{0.2}CoO_2$	300K	0.517(7)	0.172(9)	0.013	0.014	7.39%

Table 4.6: Refinement of $Na_xCa_yCoO_2$ principal Bragg reflections from neutron and x-ray diffraction data.

The thermal parameters were initially refined as isotropic spheres and then allowed to vary in different directions as an ellipsoid. While the thermal isotropic sphere for the Na ions in the pure system had a large radius, the calcium sitting on the Na1 sites in these systems has small isotropic radii. Sodium on the Na2 sites however, show similar values to the pure system, implying a similar amount of movement. This could be due to the calcium ions being heavier, which may lead to them vibrating less than their monovalent neighbours.

The R-factors for these refinements show that there is excellent agreement between the refined models and the experimental data. Other refinements were attempted that changed the assumption of the locations of sodium and calcium in the system. These resulted in unrealistic concentrations of calcium or negative thermal parameters, and these models were, therefore, rejected.

Intensities from the superlattice reflections from $Na_{0.57}Ca_{0.14}CoO_2$ were obtained from the neutron and x-ray data using a combination of automatic and manual integrations. The number of reflections for the x-ray data were much larger, though for both sets erroneous integration led to incorrect intensities for some peaks. The real space supercell that describes the superlattice in reciprocal space creates a structure of seven hexagonal Sodium Cobaltate unit cells, and the concentrations from the refinements meant that 4 sodium ions and 1 calcium were added to each layer. RMC calculations led to a solution that was largely independent of the starting parameters (such as number of iterations and annealing temperature parameters). The solution illustrated in figure 4.23 puts the calcium on an Na1 position surrounded by sodium ions sitting at Na2 sites. The fit for this model was better than previous results, giving a χ^2/n_d of 9.43 and an R_w value of 8.56%. Figure 4.24 shows the calculated x-ray pattern for this solution, and it compares well in the low L planes to the observed patterns in figure 4.21. The intensity falls off slower than observed in the high L planes, which could be due to some disorder in the long range stacking of the supercell along the c-direction.

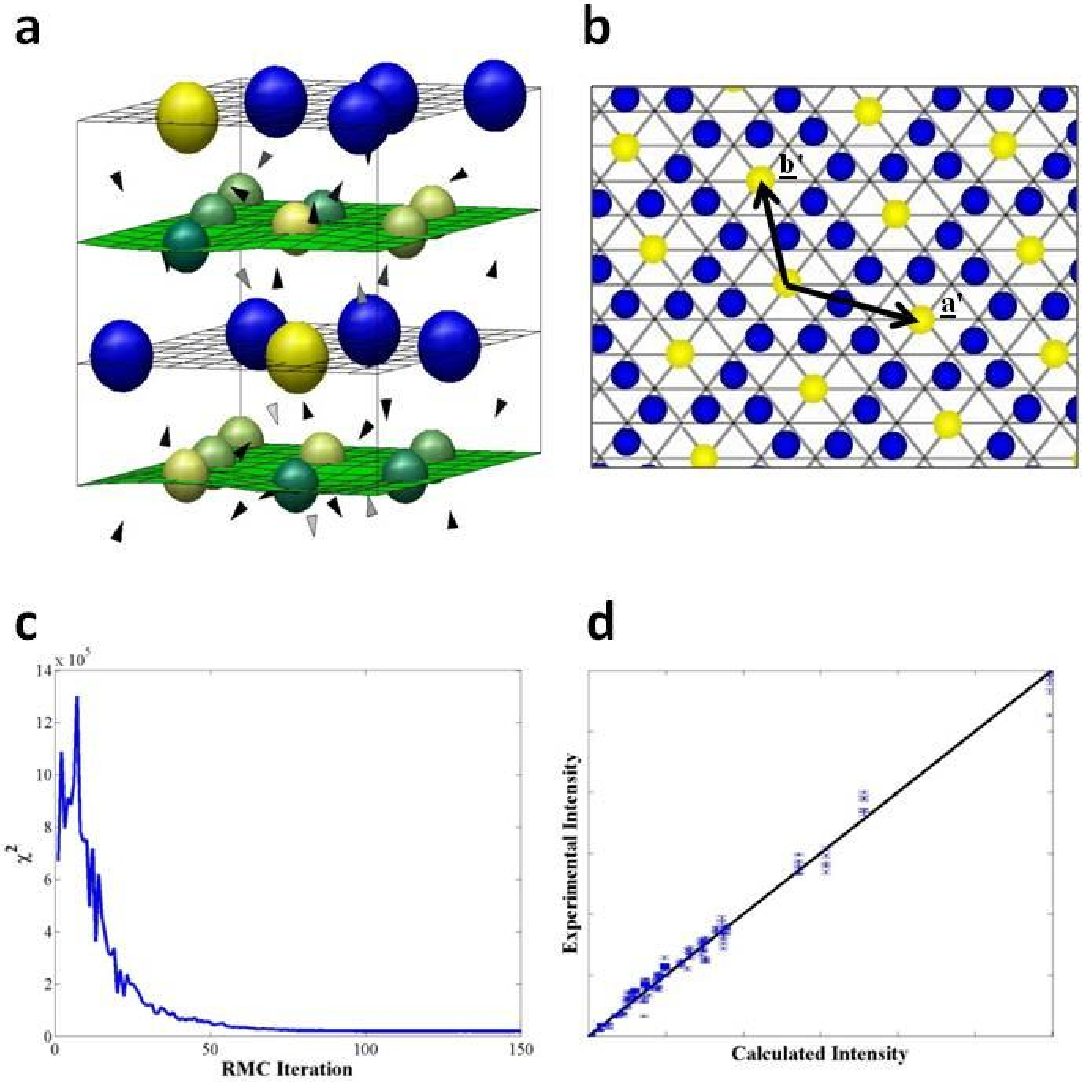

Figure 4.23: Results from the RMC calculation of $Na_{0.57}Ca_{0.14}CoO_2$ x-ray data. **(a)** The resultant structure, where blue balls are sodium ions, yellow are calcium ions, the other balls are cobalt ions, where dark green is a large negative distortion and light green is a large positive distortion. The arrows indicate the positions and distortion directions of the oxygen ions. **(b)** Top-down view of the sodium layer. **(c)** Annealing of χ^2 during the calculation. **(d)** Final comparison of calculated and experimental intensities on the right.

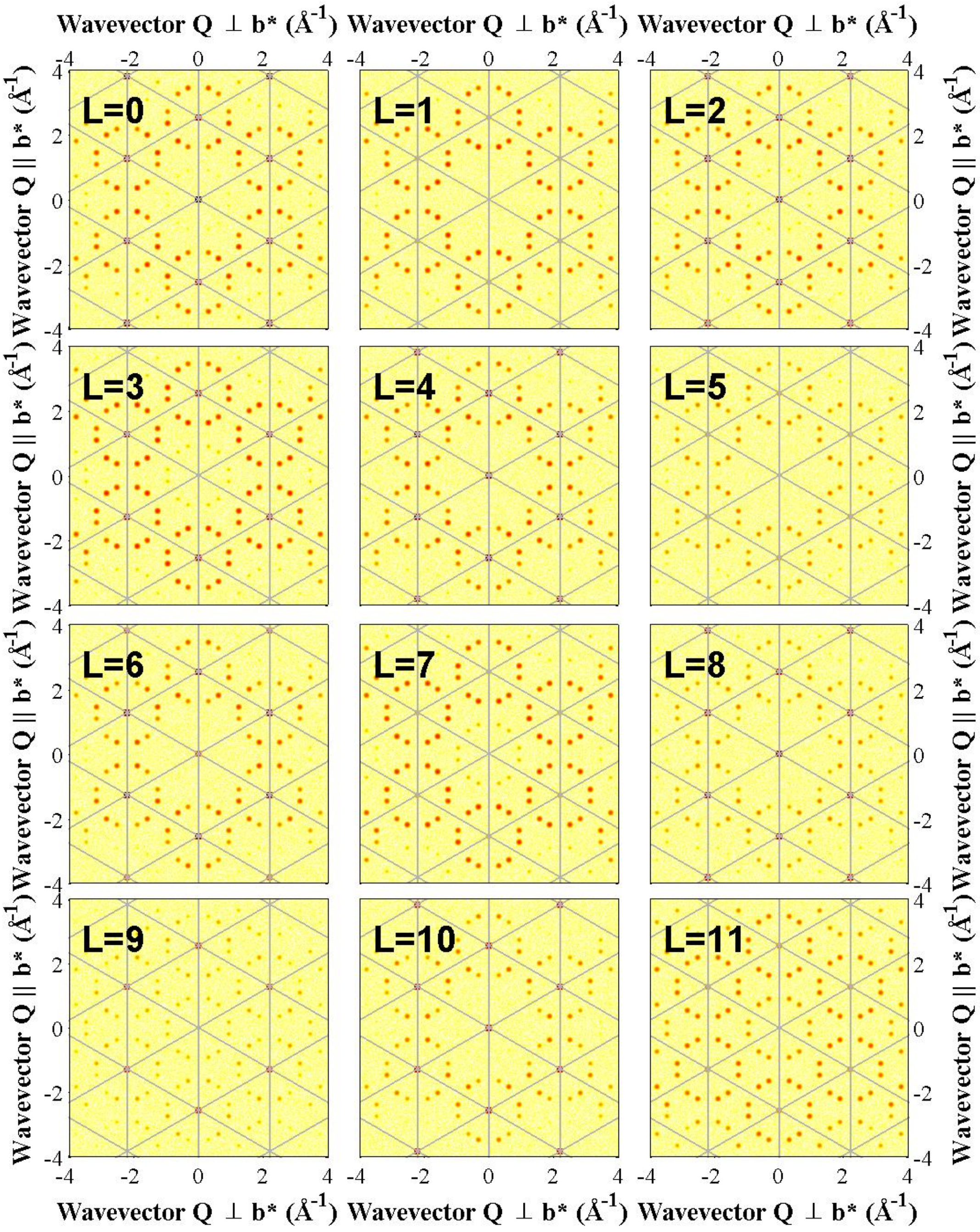

Figure 4.24: Full L-dependence for the RMC calculation of $Na_{0.57}Ca_{0.14}CoO_2$ x-ray data.

For pure Sodium Cobaltate the corresponding superstructure has a sodium concentration $x = 5/7$. According to calculations of the ground state energies of multi-vacancy structures, this is the only stable di-vacancy cluster in this composition range, see figure 4.1(c). It is likely that the substitution of the divalent calcium at the centre of the di-vacancy cluster has a stabilising effect since it lowers the charge of the di-vacancy cluster. The fact that this superstructure does not change with temperature, and it forms over a range of sample compositions, suggests that it is a particularly stable superstructure.

The RMC calculations also exhibit ordering in the distortions of the cobalt plane, with cobalt ions moving away from the closest calcium (which is sitting at an Na1 site). The distortions are smaller than for the pure system though the form of the distortions is the same, this makes sense as the divalent nature of calcium will reduce the electrostatic potential from the vacancy cluster. Figure 4.23-top shows the calcium doped di-vacancy structure with cobalt distortions emphasized for clarity.

For $Na_{0.6}Ca_{0.2}CoO_2$ this di-vacancy phase coexists with the phase observed for $Na_{0.5}CoO_2$. In fact, the $Na_{0.5}CoO_2$ superstructure can also be viewed as stripes of di-vacancy clusters.

In summary, both neutron and x-ray diffraction of calcium doped Sodium Cobaltate revealed a previously unobserved superlattice that could be explained by a superstructure with 7 unit cells. The RMC program was then used to find the ordering in the sodium layer, generating a di-vacancy structure where calcium ions form at the centre.

4.4.3 $Na_xSr_yCoO_2$

A single crystal of $Na_{0.7}Sr_{0.1}CoO_2$ was cleaved from a boule and measured using Neutron Laue diffraction on SXD. Measurements were made of large portions of reciprocal space at temperatures of 350K, 150K and below 10K. To attain the largest coverage of reciprocal space on the detectors, the sample was moved through several different orientations, each of these orientations was given around 8 hours of beam time. The experiments took place over a period of several months with several different trips to ISIS, however, it was found that the sample remained robust during this time.

As illustrated in figure 4.25, the results from the experiments show a superlattice of peaks indicating patterning of the sodium layer. At 350K, six-fold rings are visible around the principal Bragg reflections at the same positions as the high temperature phase in pure $Na_{0.8}CoO_2$. At low temperature, superlattice peaks from the ordered stripe phase are observed, again consistent with $Na_{0.8}CoO_2$. However additional peaks are observed in certain planes that are much closer to the principal Bragg reflections, such as those in the $(hk9)$ plane illustrated at the bottom of figure 4.25. Figure 4.26 shows the full L dependence from these data sets at 150K.

Other compositions were screened using SXD, but it was not possible to obtain a single crystal large enough for neutron diffraction. The ability to perform diffraction experiments with much smaller crystals is a considerable advantage for x-rays, and the composition dependence was determined using x-ray diffraction. Figure 4.27 illustrates typical superlattice reflections from samples of composition $Na_{0.7}Sr_{0.1}CoO_2$, $Na_{0.6}Sr_{0.2}CoO_2$ and $Na_{0.48}Sr_{0.32}CoO_2$. The superlattice wave vectors are different to those observed for $Na_{0.7}Sr_{0.1}CoO_2$ using neutron diffraction. Furthermore, the superlattice reflections are strongest away from the hexagonal reciprocal lattice vectors, in contrast to all previous Sodium Cobaltate samples.

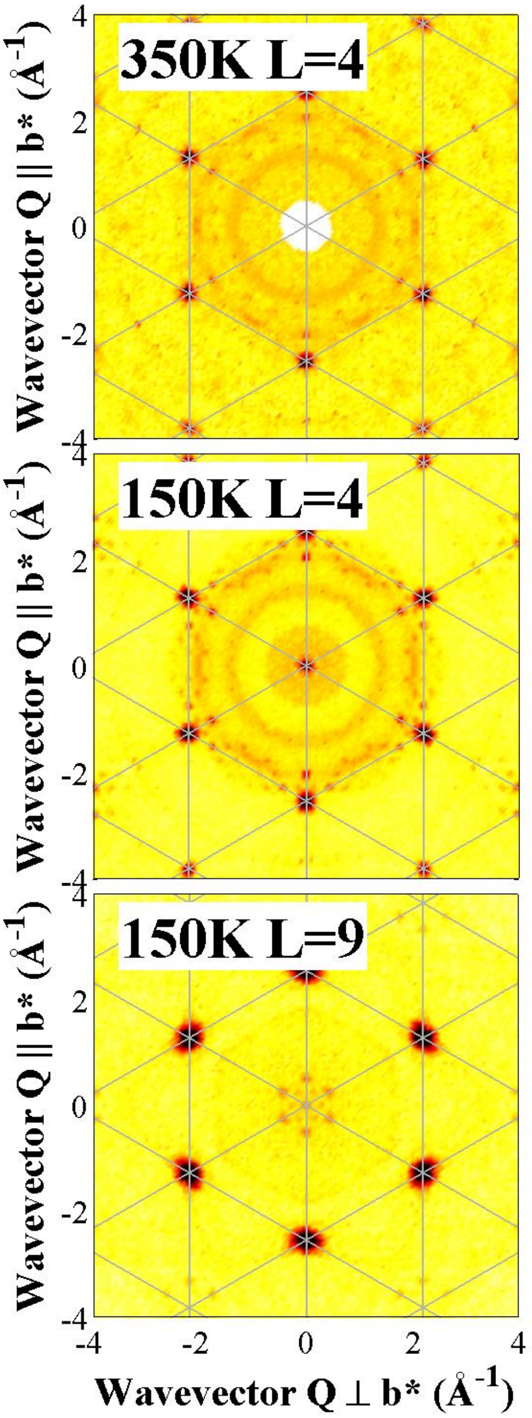

Figure 4.25: Cuts through reciprocal space for $Na_{0.7}Sr_{0.1}CoO_2$ on SXD. Weak peaks in the 1/5th positions are seen at 350K whereas the ordered stripe superlattice is observed at 150K. Additional weak peaks are observed at 150K in the L=9 plane, close to the (009) extinction and by the 104 peaks in the L=4 plane.

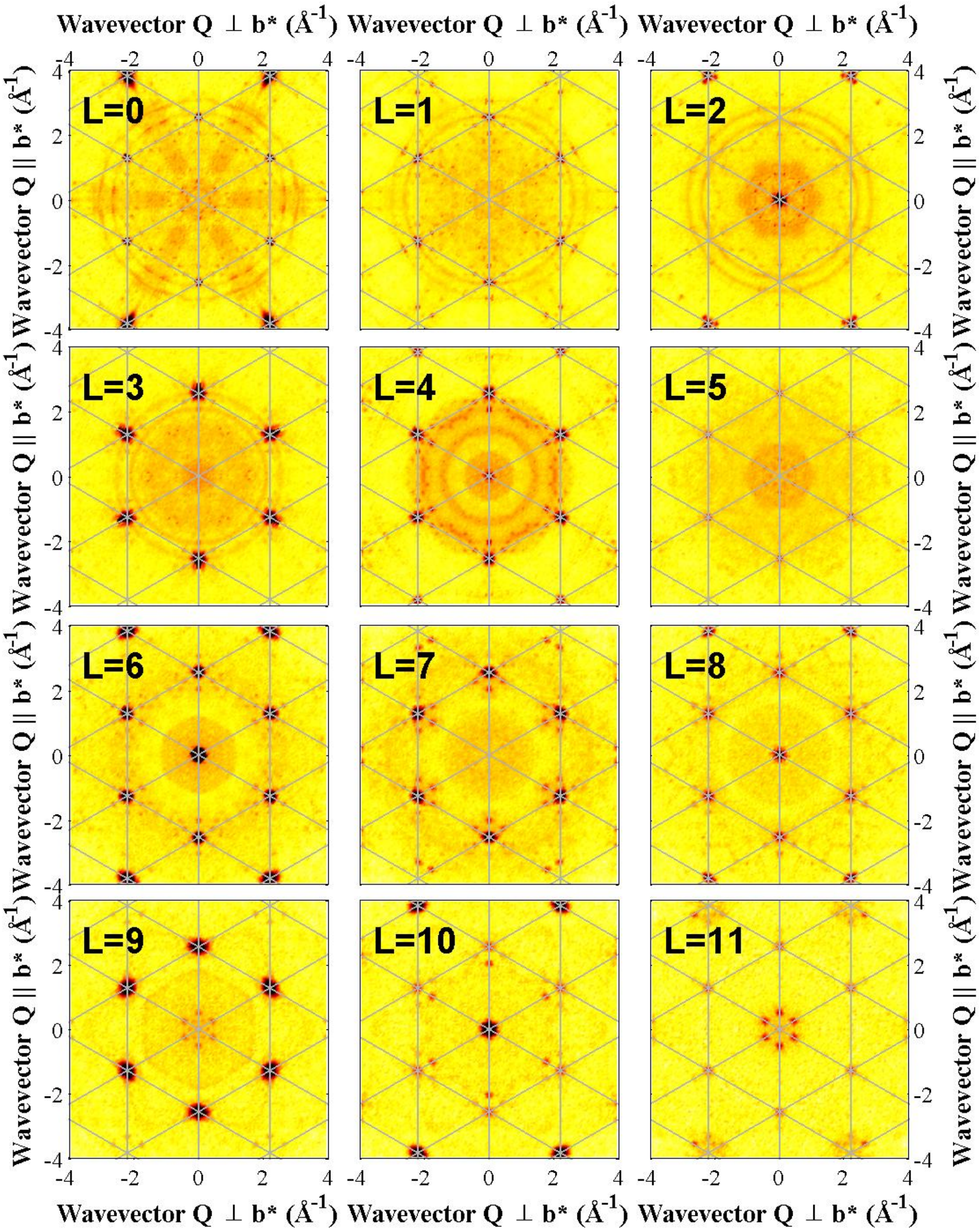

Figure 4.26: Full L-dependence of the SXD data for $Na_{0.7}Sr_{0.1}CoO_2$ at T=150K

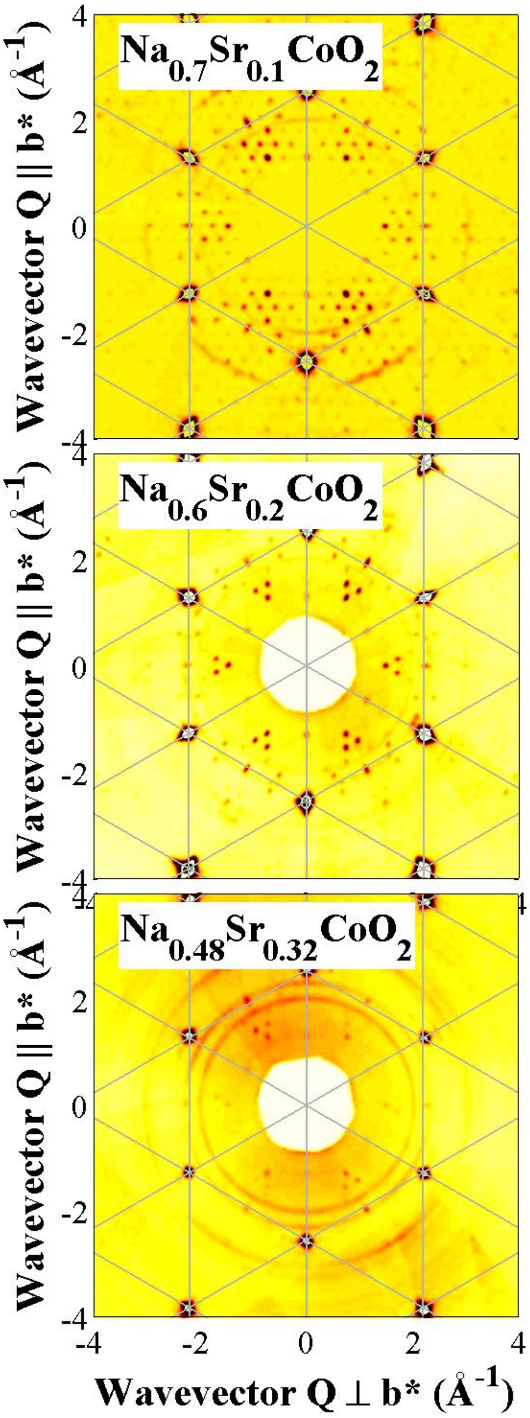

Figure 4.27: Three compositions of $Na_xSr_yCoO_2$ measured using x-ray diffraction, the $(h, k, 0)$ plane is shown at 300K.

Figure 4.28 shows that the peaks in $Na_{0.7}Sr_{0.1}CoO_2$ can be indexed with superlattice vectors:

$$\underline{\mathbf{a}}' = 5\underline{\mathbf{a}} + 10\underline{\mathbf{b}}$$

$$\underline{\mathbf{b}}' = 10\underline{\mathbf{a}} + 5\underline{\mathbf{b}}$$

This large cell, comprising 75 hexagonal Sodium Cobaltate unit cells has been named the alpha phase for strontium doped systems. The peaks observed in $Na_{0.6}Sr_{0.2}CoO_2$ and $Na_{0.48}Sr_{0.32}CoO_2$ can be indexed with a second set of superlattice vectors, named the beta phase:

$$\underline{\mathbf{a}}' = 3\underline{\mathbf{a}}$$

$$\underline{\mathbf{b}}' = 8\underline{\mathbf{a}} + 10\underline{\mathbf{b}}$$

The beta phase includes 30 unit cells and can be described as a doubling of the stripe phase supercell between successive stripes. Other peaks were found in the data that could be attributed to the 1/13th phase or $\lambda/2$ contamination, described previously in section 4.4.1. The full L dependences for $Na_{0.7}Sr_{0.1}CoO_2$ and $Na_{0.6}Sr_{0.2}CoO_2$ are shown in figures 4.29 and 4.30 respectively.

While the majority of the superlattice peaks observed in the neutron data cannot be indexed using either the alpha or beta supercells, the additional peaks observed very close to the main hexagonal positions can be indexed with the alpha phase propagation vectors. The large sample of $Na_{0.7}Sr_{0.1}CoO_2$ used for the neutron experiments was measured in reflection geometry using the Royal Holloway diffractometer, and as illustrated in figure 4.31, alpha phase peaks can be observed around the principal Bragg reflections.

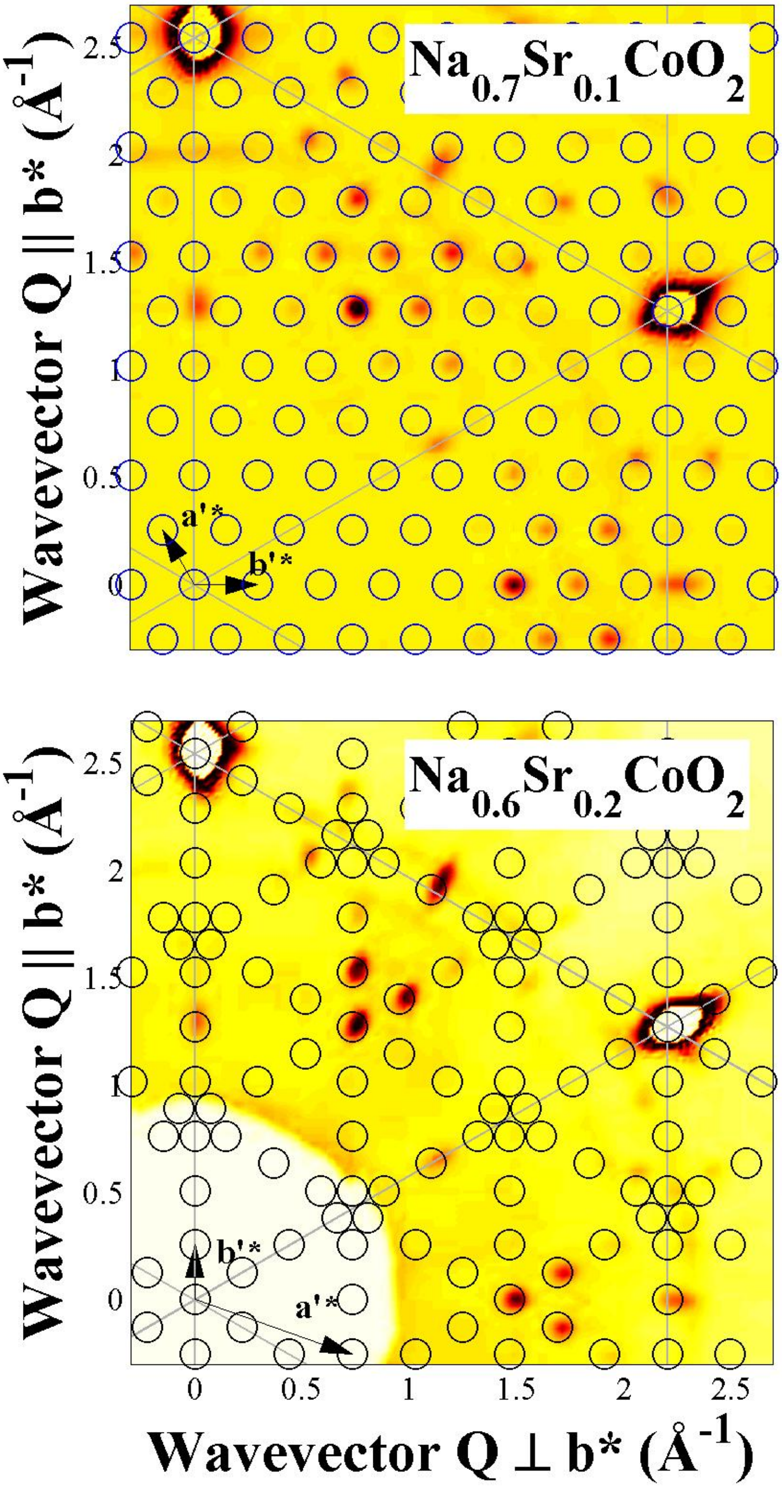

Figure 4.28: Indexing of the two phases observed in $Na_xSr_yCoO_2$, as described in the text.

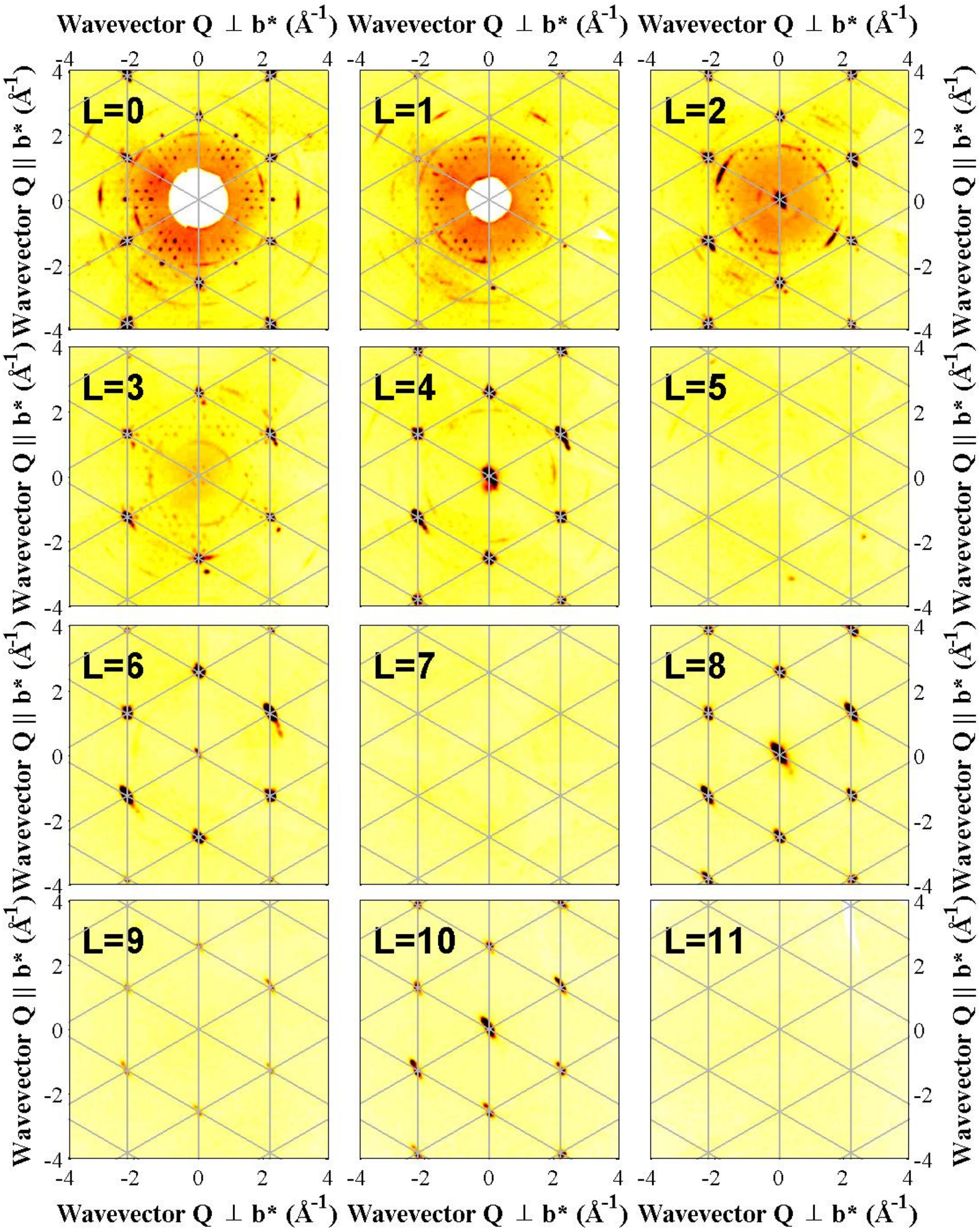

Figure 4.29: Full L-dependence of the x-ray data for $Na_{0.7}Sr_{0.1}CoO_2$ at T=300K.

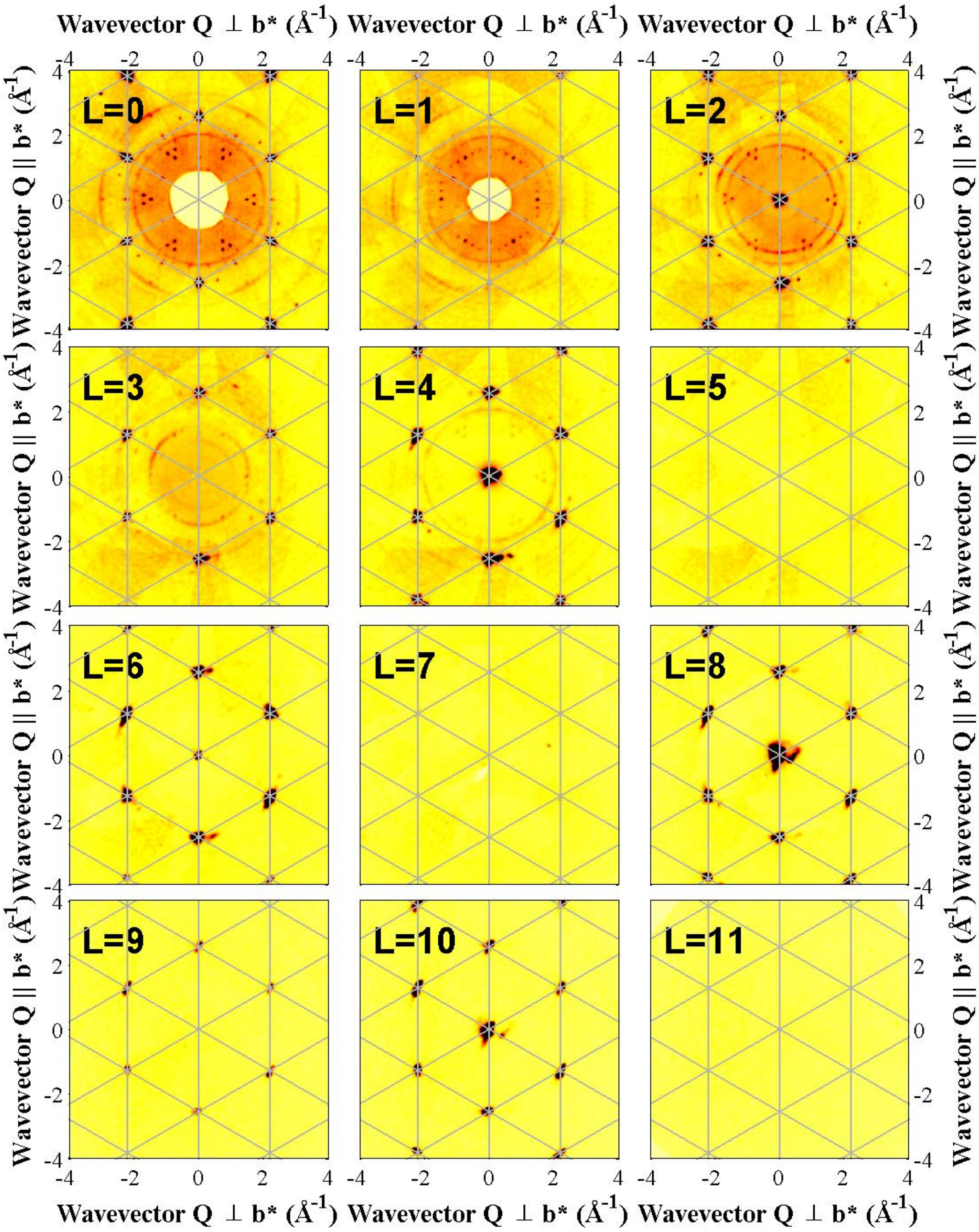

Figure 4.30: Full L-dependence of the x-ray data for $Na_{0.6}Sr_{0.2}CoO_2$ at T=300K.

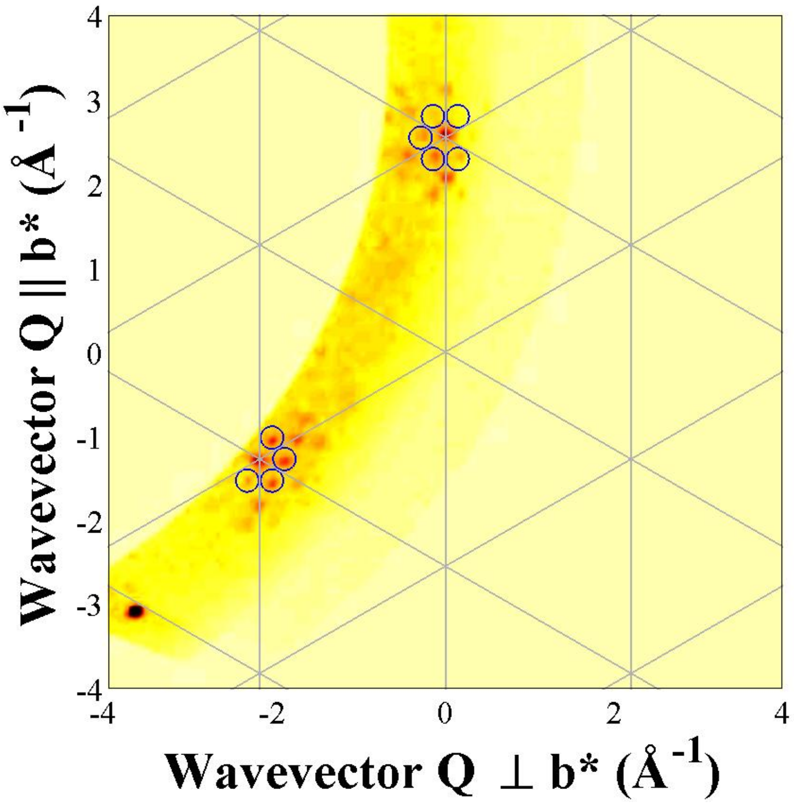

Figure 4.31: X-ray measurement of the of $Na_{0.7}Sr_{0.1}CoO_2$ neutron sample in reflection geometry, the $(hk7)$ plane is shown. Reflections from the alpha phase of Sr doping are marked with circles.

Refinements were performed using the hexagonal Bragg peaks of the neutron and x-ray experimental data using Jana2006. The method used is the same as for the calcium doped system, where the sodium ion is placed on the Na2 site and the dopant is placed on the Na1 site. Table 4.7 shows typical refinement results. It was not possible to obtain reliable integrations for some temperatures and compositions due to high backgrounds and weak scattering. The refinements reveal very similar occupancies for sodium and strontium across all three experiments. This is surprising, particularly given that the superlattices are found to be different in each case. It is possible to obtain different superstructures for the same composition, as we found for the square and striped phase of $Na_{0.8}CoO_2$.

		Occupancy		U_{iso}		
Composition	Radiation	Na	Sr	Na	Sr	R_w
$Na_{0.7}Sr_{0.1}CoO_2$	Neutron	0.56(1)	0.099(8)	0.018	0.015	6.45%
$Na_{0.7}Sr_{0.1}CoO_2$	X-ray	0.542(8)	0.067(5)	0.016	0.033	6.31%
$Na_{0.6}Sr_{0.2}CoO_2$	X-ray	0.54(1)	0.071(8)	0.029	0.037	8.60%

Table 4.7: Refinement of $Na_xSr_yCoO_2$ principal Bragg reflections from neutron and x-ray diffraction data.

The refined thermal parameters show that strontium has a large isotropic thermal displacement value, in contrast to calcium, which had a lower value than sodium. This may arise from differences in the multi-vacancy clusters. Alternatively, it may be due to the presence of static disorder, due to the lack of mobility of the strontium ions, which have a larger radius than sodium. The shape of the thermal ellipsoids is the same in all three refinements and is consistent with $Na_{0.8}CoO_2$, where cobalt and oxygen are elongated along the c-axis and atoms in the sodium layer are spread out within the plane.

RMC has been attempted on the x-ray data, however, the integration files used tend to be unreliable and only have a small number of peaks. As a result, the calculations did not lead to a solution of the long-range order. X-rays are most sensitive to the strontium ions, and some quite robust results on the strontium ordering could be inferred. Simulations for the alpha phase tend to lead to the formation of multi-vacancy clusters with four strontium ions, whereas stripes of strontium ions are found for the beta phase. The location of the sodium ions is less well defined, with a degree of randomness. The fits to the data from the generated structures are not statistically good, but the results were used as a guide for manual modelling.

By manually calculating a large number of possible structures, it has been possible to find two models that give rise to similar superlattice patterns to those observed in the data. These are shown in figure 4.32 and 4.33. The beta phase comprises a single stripe of strontium ions sitting $a\sqrt{3}$ apart on Na2 sites, with vacancies surrounding the stripe. The alpha phase comprises two 12-vacancy clusters within the supercell, where each cluster contains 4 strontium ions on Na1 sites, separated from each other by $a\sqrt{3}$.

The agreement between the calculations and the x-ray data for the beta phase is quite good. All of the beta phase peaks are reproduced, and the very different patterns for L = odd or even are captured. The intensity falls off a bit faster with L than predicted, but this could be due to a high Debye-Waller factor from static disorder.

For the alpha phase the x-ray data set is complex and the agreement is encouraging. However, the tight ring of superlattice peaks calculated around reciprocal lattice points for all L are only observed for L = 7 and in general, the L dependence for this phase does not agree well.

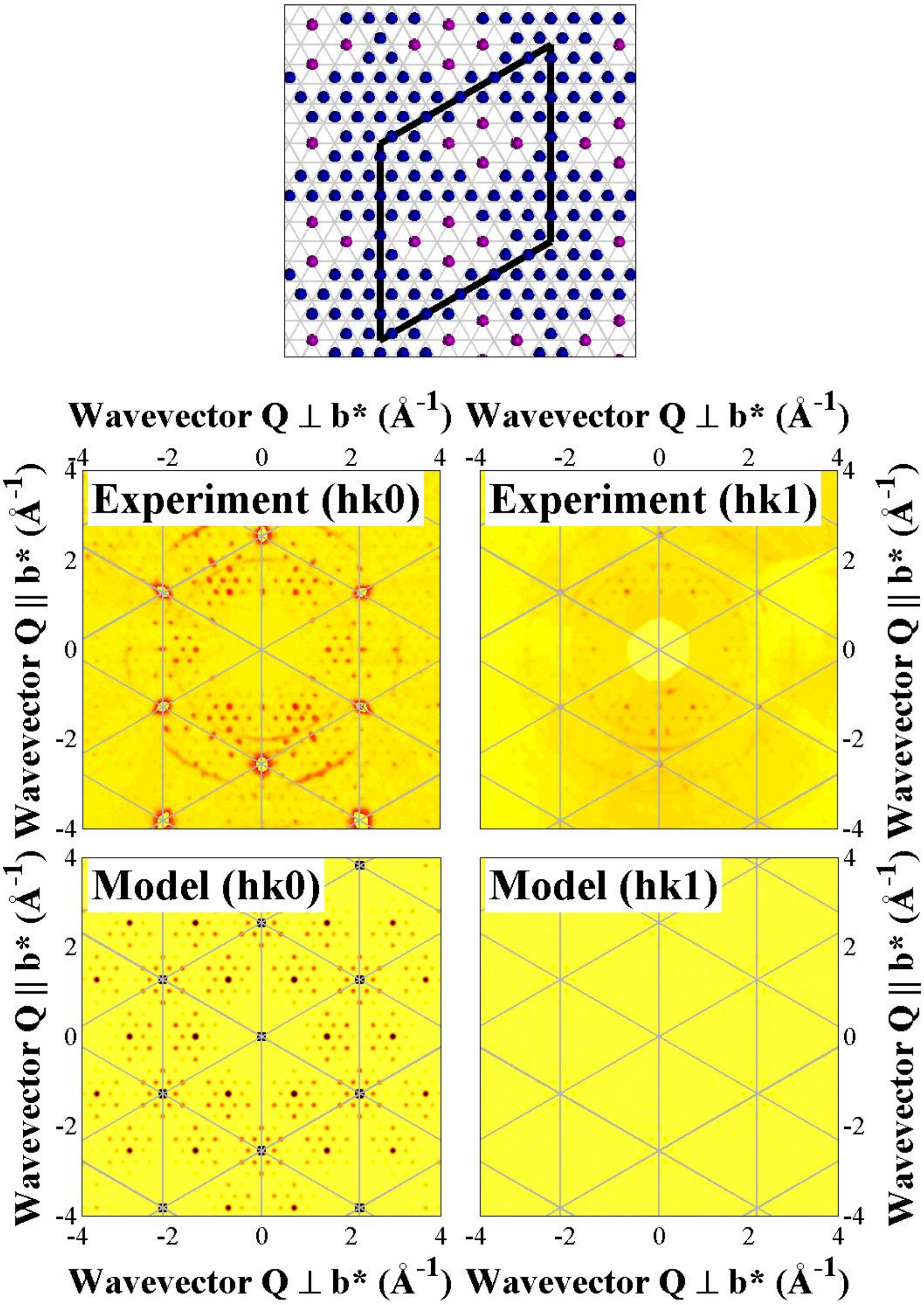

Figure 4.32: Model and calculation for the alpha phase of $Na_{0.7}Sr_{0.1}CoO_2$. Blue balls show sodium ions and purple balls are strontium.

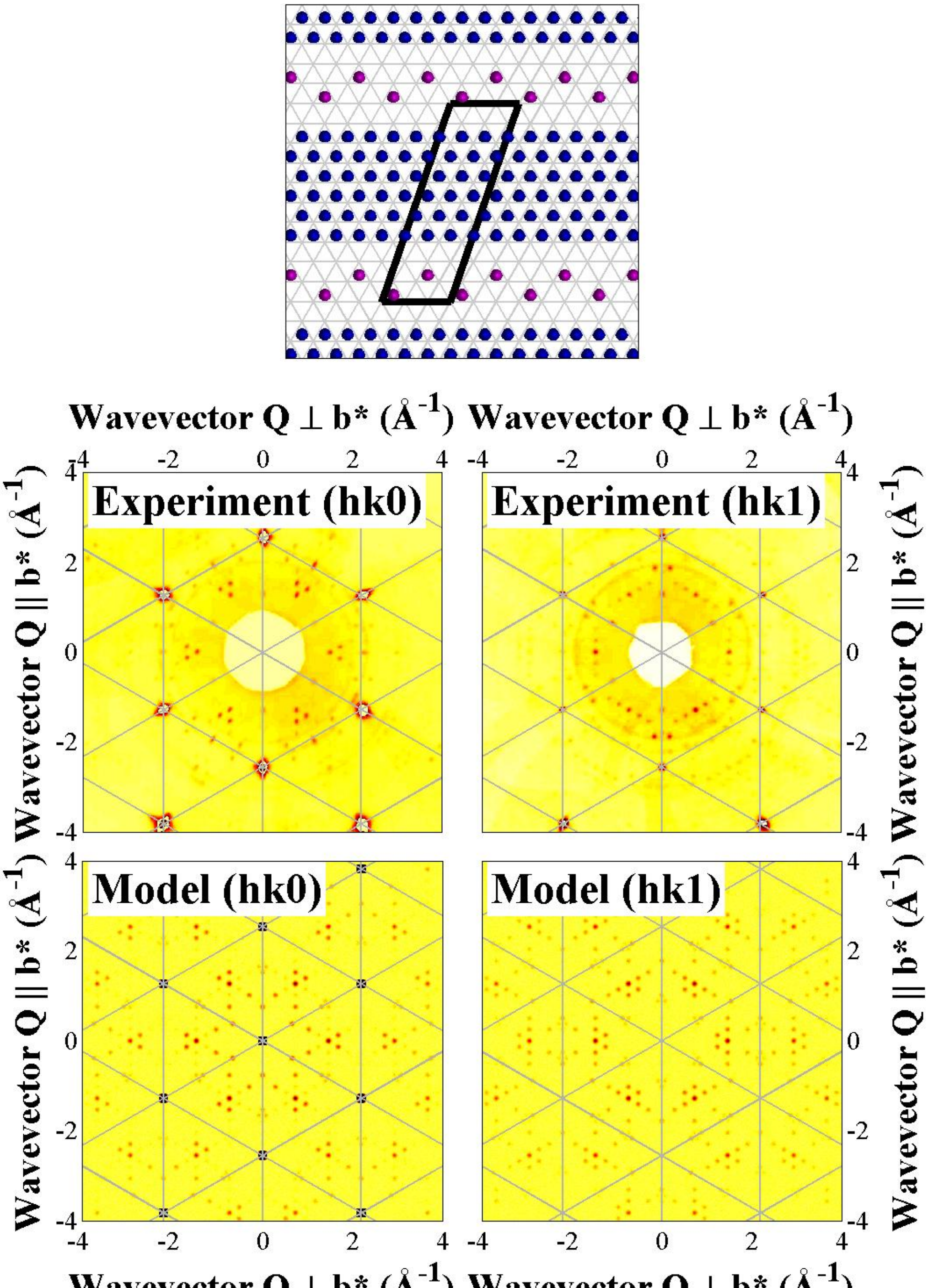

Figure 4.33: Model and calculation for the beta phase of $Na_{0.6}Sr_{0.2}CoO_2$. Blue balls show sodium ions and purple balls are strontium.

4.4.4 Temperature Dependences

Temperature dependence measurements on the superstructures of the materials described previously were performed on SXD using the furnace sample environment. High temperature exposures were taken from 300K in 25K steps until the strongest superlattice reflections had visibly disappeared. The system would then be re-cooled to observe the re-emergence of the superstructure. The variation in superlattice intensity for the three systems measured is shown in figure 4.34. Unfortunately it was not also possible to perform temperature dependence measurements with x-rays, because at the current time, the Royal Holloway diffractometer can only measure at 300K.

In the Oxford grown $Na_{0.8}CoO_2$ sample, the strongest superlattice reflections had visibly disappeared at 425K. Above 425K the sodium layer had become disordered, as indicated by the absence of satellites in figure 4.10. Cooling the system back to 300K resulted in the original superlattice returning with the same intensity. In the calcium doped system, the superlattice peaks disappeared at 370K, $\approx 50K$ less than the pure system, despite the very stable di-vacancy superstructure.

High temperature measurements of the strontium systems revealed that the superlattice peaks disappeared by 400K, also lower than the pure sample. Unfortunately, our first measurement on heating was at 373K, and by this point the superlattice peaks had already reduced in intensity substantially, and the relative intensities of different superlattice reflections had changed. Measurements on cooling reveal strong hysteresis with the superlattice peaks reappearing at about 325K. Although the full peak height had not been recovered by room temperature, the intensity distribution resembled that at the start of the experiment.

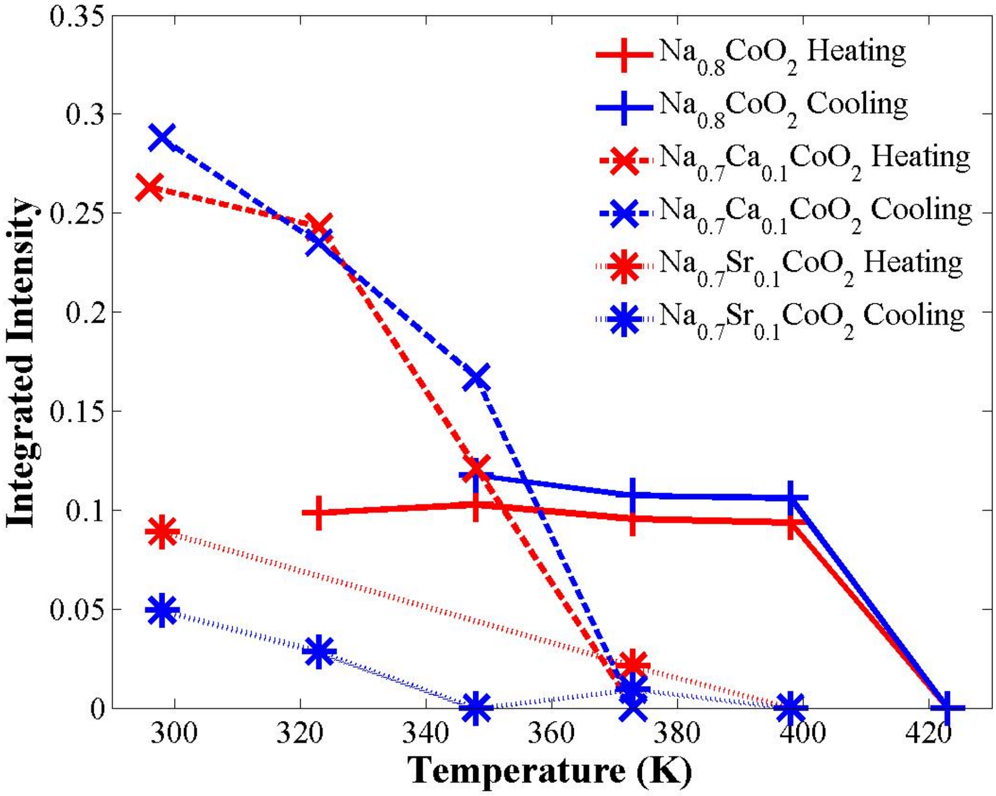

Figure 4.34: Temperature dependence of three different Sodium Cobaltate systems, measured using the SXD furnace. Each point integrates over a number of superlattice positions and averages the intensities (error bars are smaller than the symbol size).

4.5 Discussion

Standard tools in crystallography, such as charge flipping [85] and the refinement of the supercell [86] were attempted, but the results obtained were found to be unreliable and difficult to interpret. Instead substantial progress was achieved using the technique of RMC. In some cases RMC gave a detailed solution for new superstructures, in others it paved the way towards a solution by identifying key elements of a superstructure.

In the case of pure Sodium Cobaltate, large neutron data sets were available for several structural domains and, as a consequence, it was possible to determine a large number of parameters by RMC. X-ray studies yielded fewer reflections due to the fall off of intensity with form factor, and the data sets were less clean due to the presence of additional phases. For the doped systems the fall-off in intensity of the neutron data with Q meant that more x-ray reflections were available for RMC calculations and in this case x-ray data were used.

For pure Sodium Cobaltate two fully ordered phases were solved, the square and striped arrays of tri-vacancy clusters. The ordering of the sodium ions had been solved previously using RMC by Morris *et al.* [50], though the results presented here are the first time that the ordered stripe phase has been observed as a single phase. By using much larger neutron data sets we have succeeded in determining more details of the superstructure using RMC. In particular, displacements of the cobalt and oxygen ions are obtained in a much more objective and robust manner. For the square phase, the displacements of the cobalt ions obtained using RMC are compared with those proposed previously in figure 4.35, where these use the electrostatic potential gradient from the sodium ion pattern. The fact that the results agree so well with this single model gives us confidence that the RMC results are reliable.

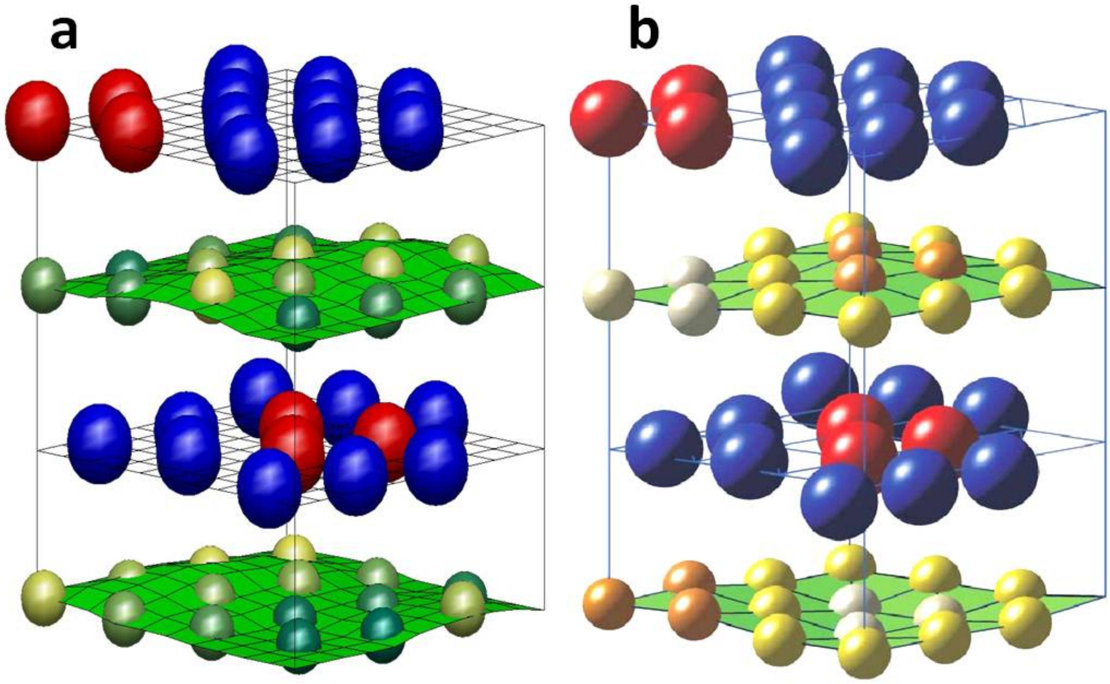

Figure 4.35: Comparison of distortions produced by RMC for the Oxford $Na_{0.8}CoO_2$ sample neutron data (a) with the distortion model predicted in Ref. [70] figure 3 (b).

The solution obtained using RMC for the calcium doped samples did not depend on the starting parameters of the RMC code and was therefore robust as well as producing a good fit to the experimental data. This array of di-vacancy clusters is known to be particularly stable [70]. The RMC calculations place the di-valent Ca^{2+} ions at the centre of the di-vacancy cluster. Since this lowers the charge on the cluster from $-2e$ to $-e$, it is likely to reduce the ground state energy of the cluster. The stability of this superstructure is evident from its presence over a range of compositions and temperatures. The distortions of the cobalt and oxygen ions seem to agree with the pure system, with neighbouring cobalt ions moving away from the di-vacancy clusters, though the distortions are much smaller in this case. The proposed superstructure will lower the hole concentration and charge modulation in the cobalt-oxygen layers, and this must affect physical properties. For the highest concentration, the presence of the insulating additional phase must also be important in determining physical properties.

For the high temperature striped phase of pure Sodium Cobaltate it is not possible to solve the superstructure using RMC due to the presence of disorder within the stripes. It has not proved possible to solve the superstructures of strontium doped samples using RMC. One factor might be the presence of static disorder, suggested by the rapid fall off of superlattice peak intensity with L. Strontium has a larger ionic radius than sodium or calcium and, therefore, it is likely to be less mobile. The stripes of strontium ions proposed for the beta phase correspond to an energetically favourable configuration, and the calculated intensities agree well with the data. The solution for the other data sets is less favourable. There are substantial differences between the proposed solution for the alpha phase and the data. Perhaps it is simply the case that the supercell is too large for the data available. In the case of the neutron superlattice peaks indexed on the disordered stripe phase, it is not clear whether this a separate phase or one that contains strontium at random positions. Either way, it is not susceptible to a solution using RMC.

Temperature dependences of the three compositions indicated that the long range sodium superstructures become disordered at around 400K. It is surprising that the calcium system has the lowest disorder temperature, as the lack of variation across compositions indicates that the di-vacancy superstructure is robust. However it is difficult to compare the energy scales of these structures due to the presence of partial disorder in the pure and strontium doped systems

Hysteresis is observed in the strontium system but not in the pure or calcium systems. This is due to the presence of large, immobile strontium ions, whereas sodium and calcium are both small and can move more freely, reducing any hysteresis effect on ordering.

These disorder transition temperatures can be very useful in assigning energy scales to the associated superstructures, allowing forward Monte Carlo techniques to be employed that can predict the sodium ordering on the basis of energy minimisation. Such calculations however, are beyond the scope of this thesis.

4.6 Conclusions

Single crystals of pure and doped Sodium Cobaltate were studied using neutron and x-ray diffraction techniques, and the satellite peaks observed were used to calculate the long range sodium ordering in each system. Temperature dependencies were determined for each system and the temperature at which the sodium layer of each system disorders was established. Integrating the intensities of the principal and satellite reflections allowed structural refinements to gain information on the sodium/ dopant occupancy in the system, as well as the thermal motions of the atomic sites. RMC techniques were employed to help solve the superstructures of the system by modelling a standard Na_xCoO_2 lattice and allowing Sodium and dopant ions to change site at random.

The pure $Na_{0.8}CoO_2$ system was found to form ordered stripes of tri-vacancy clusters at low temperatures and the stripes became disordered at room temperature. The RMC code was able to accurately solve the structure for this phase, and even included finer details of the model such as the distortions of the cobalt and oxygen ions in the system, where these distortions agreed with buckling previously predicted using an electrostatic potential gradient from the sodium ion patterning.

Doping with calcium leads to a new superstructure, where calcium ions order long range at the centre of di-vacancy clusters. At high calcium concentration, phase co-existence with the insulating 50% phase was found.

Three different diffraction patterns were observed when doping the system with strontium, including the same pattern observed in $Na_{0.8}CoO_2$ and two new superlattice patterns. RMC calculations on this data were unable to produce reliable results, but in combination with manual modelling, tentative models were discovered. The alpha phase was found to include two 12-vacancy clusters within the supercell, where each cluster contains 4 strontium ions on Na1 sites. The beta phase comprises a single stripe of strontium ions sitting $a\sqrt{3}$ apart on Na2 sites, with vacancies surrounding the stripe.

The superstructures established in this chapter can be used as a starting point for further investigations into the electronic and magnetic properties of the system.

Chapter 5

Electronic Ordering

5.1 Abstract

Resonant x-ray scattering experiments were performed on I16 at Diamond on single crystal samples of $Na_{0.8}CoO_2$ *and* $Na_{0.7}Ca_{0.1}CoO_2$. *Resonant behaviour is observed at the superlattice positions demonstrating the link between the sodium ordering and electronic patterning of the cobalt-oxide layer. The resonant behaviour is calculated from the superstructures by Density Functional Theory using the FDMNES code which is able to model the experimental data from first principles. The FDMNES calculations imply an ordering of charges in the cobalt-oxide layer and it is found that the strongest charge ordering is on the oxygen rather than cobalt ions.*

5.2 Background

It was shown by Roger *et al.* that the sodium ordering and its associated distortion field are governed by pure electrostatics, and the organizational principle is the stabilisation of multi-vacancy clusters that become ordered over long range at some simple fractional fillings. These results provide a good starting point to understand the electronic properties of the system in terms of a modified Hubbard Hamiltonian that takes into account the electrostatic potential, or ‘Coulomb landscape’, in the cobalt layers. The resulting depth of potential wells in the cobalt layer is greater than the single-particle hopping kinetic energy and, as a consequence, holes preferentially occupy the lowest potential regions [70].

This picture is consistent with the multiple valence states detected using NMR, where valence states of Co^{3+}, $\text{Co}^{3.3+}$ and $\text{Co}^{3.7+}$ are detected in the cobalt layer, suggesting charge ordering within these layers [20]. X-ray absorption studies of pure Na_xCoO_2 at the Co-L and O-K absorption edge show an increase of cobalt and oxygen valence as x decreases, as shown in figure 5.1, indicating that charge ordering could also be occurring in the oxygen layers [87]. Charge ordering has been observed in $Na_{0.5}CoO_2$, where it was found using magnetic neutron diffraction that Co^{4+} ions ordered within the plane with a supercell commensurate with the sodium supercell [6, 71, 88]. However, prior to this work, this patterning has not been detected in the high-x compositions by a diffraction technique that gives spatial information.

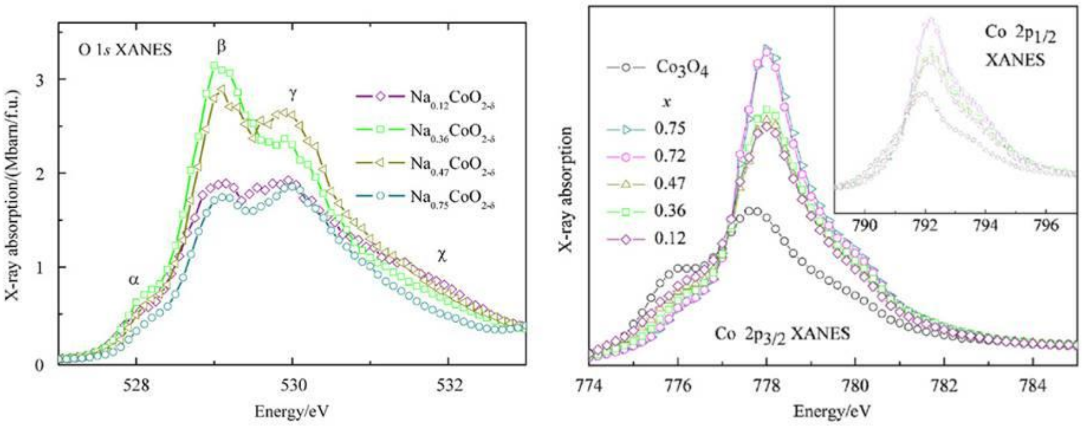

Figure 5.1: Co 2p and O 1s x-ray absorption spectra for Na_xCoO_2, from Fig. 4 and 8 Ref. [87]. As x increases, there is an change in x-ray fluorescence in both systems, where the alteration of peak heights and centroid mass are attributed to a change in valence of each ion.

The stoichiometric compound $NaCoO_2$ ($x = 1$) is insulating with a cobalt t_{2g} sub-band, in the 3d shell, filled with 6 electrons [89]. In Na_xCoO_2, the removal of $\delta = (1 - x)$ sodium ions creates δ holes in the Co layers. These holes preferentially occupy the lowest potential regions within the layer, leading to charge ordering if the potential is patterned [90, 80]. The substitution of a divalent ion, such as Ca, for Na decreases the number of holes in the Co layer, and this will dramatically affect the electronic and magnetic properties.

Resonant x-ray scattering combines the spatial sensitivity of diffraction with the sensitivity to the band structure of absorption spectroscopy techniques, allowing direct measurements of electronic ordering in Na_xCoO_2 for the first time. The measurements of $Na_xCa_yCoO_2$ show how this ordering changes as the superstructure changes and the number of holes is decreased.

5.3 Experimental Procedure

Resonant x-ray scattering measurements were performed on single crystal samples of $Na_{0.8}CoO_2$ and $Na_{0.7}Ca_{0.1}CoO_2$ using the beamline I16 at the Diamond synchrotron. Details of the instrument are described in section 2.3.5. The two samples were measured during separate beam times, each lasting six days. In both cases large single crystals were screened at Royal Holloway using x-rays.

The samples were mounted in a cryofurnace on I16 with a temperature range 12<T<600K. The crystals are flat plates with the hexagonal c-direction normal to the surface. These were stuck on a copper block using silver paste in order to obtain a good thermal contact.

The experiments were performed in reflection geometry. Samples were aligned at room temperature and scans of beam position along the surface were performed to identify the best single-crystal grain. The $Na_{0.8}CoO_2$ sample was measured in the vertical scattering geometry. In this case some of the structural superlattice reflections measured in the σ-σ channel were weak, and it was possible to detect resonant scattering in the σ-π channel. Attempts to measure resonant scattering from $Na_{0.7}Ca_{0.1}CoO_2$ were unsuccessful in this scattering geometry, since the structural superlattice reflections were large, and the leakage in the rotated channel swamped the signal. Therefore, the $Na_{0.7}Ca_{0.1}CoO_2$ sample was measured in the horizontal scattering geometry, where we can measure the π-π and π-σ channels. The reflections were chosen to have a scattering angle close to 90° so that the π-π cross section is small and, therefore, the leakage in the π-σ is also considerably reduced.

In order to characterize the nature of the resonant scattering a series of measurements are performed. First, by scanning x-ray energy with Q fixed it is possible to vary the cross section for a particular reflection. A resonance is peaked in the vicinity of an absorption edge. Secondly, a scan of Q is performed with energy fixed at the maximum to distinguish between resonant x-ray scattering and fluorescence. The scan would be peaked for resonant scattering, whereas it would be flat for fluorescence, which does not depend upon Q. Thirdly, polarisation dependence can be used to discriminate between different types of scattering. Charge scattering is always in the unrotated channel, σ-σ or π-π. In general, scattering from the magnetic or orbital order is present in both the unrotated and rotated channels. However, in our case the electronic ordering has the same periodicity as the superstructure and the scattering in the unrotated channel is dominated by the structural charge scattering. Our studies of resonant scattering are, therefore, limited to the rotated channels (σ-π and π-σ) where leakage of charge scattering from the unrotated channel can still be a problem. Fourthly, the azimuthal dependence of the scattering gives important additional information on the nature of resonant scattering. Charge scattering is isotropic and, therefore, it is independent of azimuthal angle. In contrast, magnetic and orbital ordering are anisotropic, and this leads to a characteristic azimuthal dependence. When rotating the azimuthal angle the beam often moves along the surface of the sample and it is necessary to realign. In order to obtain reliable data it is necessary to normalise to the charge scattering. In our case this is achieved by normalising the σ-π (π-σ) scattering by the structural scattering in the σ-σ (π-π) channel. Finally, the temperature dependence is used to relate the order parameter to any known phase transitions. Again realignment of the sample is necessary due to changes in lattice parameters, and small movements and rotations of the sample.

5.4 Computational Modelling

To explain the resonant behaviour we used the FDMNES code by Yves Joly [58] to calculate the experimental data from first principles. FDMNES is able to predict resonant scattering for a system using only its atomic positions. It does this by generating the electronic structure from Density Functional Theory using a muffin-tin potential and other approximations, see chapter 3. It then calculates the energy, polarisation and azimuthal dependence of the resonant x-ray scattering.

We used the atomic coordinates generated by Reverse Monte Carlo in Chapter 4, including 114 atoms for $Na_{0.8}CoO_2$ and 52 atoms for $Na_{0.7}Ca_{0.1}CoO_2$, both of which are large numbers for such calculations (for reference, the strontium systems have 568 atoms for the alpha phase and 220 for the beta phase, which would make calculations of these systems very difficult). The variables used in the calculation are listed in appendix B. The radius of the cluster used is the most important parameter and the approximations used. Calculations with a small radius and the additional memory-save approximation (which limits the number of atoms used to calculate the electronic potential and reduces the amount of memory required in the processing computer) where possible on my own duel-core laptop and would generally take about two days. We found that due to the large size of the cell and the high number of atoms, certain calculations could only be performed on a cluster of computers optimized for large scale parallel computing. Calculations with a larger radius and no memory-save approximation had to be performed on a cluster of computers with the aid of Michel Roger in Paris. The cluster had one hundred CPUs and was able to complete calculations in around 4 days. An example input data file for these calculations is given in appendix B. Resonant behaviour can also be caused by distortions of the cobalt-oxygen bond lengths, from the Jahn-Teller effect [91], therefore, the atomic coordinates we use do not include any distortions in the cobalt-oxygen layers.

The initial step of the FDMNES code is to solve the electronic structure of the system using only the basis of atoms in the input file. The calculation is self-consistent meaning that the electronic states about each atom are calculated and re-calculated in a loop until the calculation converges and there is no change between successive steps. The charge of each atom in the supercell is then defined by the density of filled electronic states within a certain radius of each atom, and this radius is defined using standard values for different atoms. Plotting the charge on each atom at its location in the superstructure allows us to visualise the ordering of charge in the system. The charge ordering calculated by FDMNES leads to scattering in the unrotated channel and since this signal is obtained by the scattering from the superstructure, we can not directly measure the charge ordering in this experiment. However other aspects of the electronic structure, such as orbital ordering, can lead to resonances in the rotated channel at the superlattice peaks which can be calculated by FDMNES and compared with the resonant scattering observed in the I16 experiment. The FDMNES code is able to calculate lineshapes for energy spectra and azimuthal dependence, which can be compared to the experimental data by applying a scaling factor and an offset in energy to correct for calibration errors. The azimuthal dependence is calculated at the maximum of the resonance, where the azimuthal angle, Ψ, defines the rotation angle perpendicular to $\underline{\mathbf{Q}}$, where $\Psi = 0$ is defined as the direction parallel to $\underline{\mathbf{a}^*}$, along the beamline direction. Note that the calculations have the same definition of the azimuthal angle as I16 and are directly comparable.

5.5 Results

5.5.1 $Na_{0.8}CoO_2$

After aligning the beam on a single crystal grain within the $Na_{0.8}CoO_2$ sample, we were able to observe two different superlattice phases at room temperature, the 1/13th phase previously seen in deintercalated systems [73] and the random stripe phase that is normal for this system.

At low temperature (10-20K) the 1/13th phase peaks were still there, but additional off-axis peaks had appeared indicating that the stripe phase had become ordered, which can be seen in figure 5.2. As less is known about the 1/13th phase, we decided to only study the ordered stripe phase. The lattice parameters for these phases are different. For large L the resolution in Q is sufficient to allow the scattering from these phases to be separated.

We looked for charge ordering in the stripe phase using the PILATUS area detector, i.e. with no polarisation analysis, by scanning in energy across the cobalt-K absorption edge ($\approx 7.78keV$) at different points in reciprocal space. Typical data is shown in figure 5.3. We found that there were no conclusive peaks at the absorption edge at any of the superlattice positions in the $(h, k, 9)$ or $(h, k, 10)$ plane. Instead the lineshape is typical of the absorption expected for purely structural scattering.

Next we decided to use the analyser crystal to measure polarisation dependence of the superlattice peaks, performing energy scans in the σ-σ (No polarisation rotation) and σ-π (rotated polarisation) channels. As shown in figure 5.4, we observed

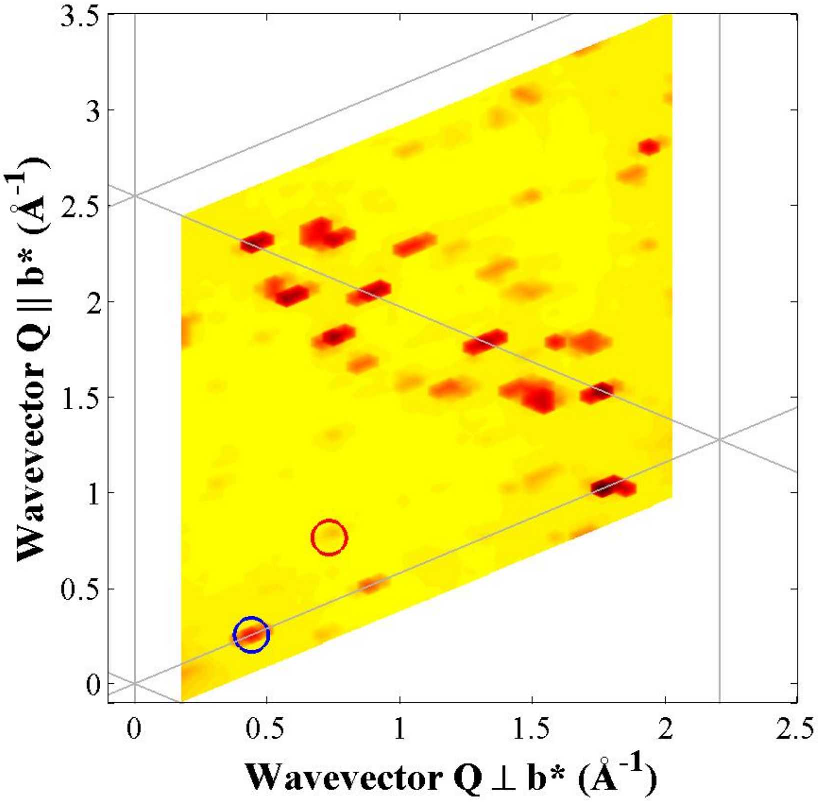

Figure 5.2: The structural scattering in the $(h, k, 10)$ plane for $Na_{0.8}CoO_2$ at T $\approx$ 20K. The peaks can be indexed using the ordered stripe phase superstructure described in Chapter 4. The polarisation dependence, energy line shape, temperature dependence and azimuthal dependence were determined for the circled peaks at $\underline{\mathbf{Q}} = (0.2, 0, 10)$ and $(0.333, 0.133, 10)$.

peaks at the absorption edge in scans of x-ray energy with Q fixed at $(0.2, 0, 10)$ and $(0.333, 0.133, 10)$. Scans of energy were performed in the σ-π channel and the fluorescent background was measured away from the superlattice reflection where Q scans were flat. By measuring the scattering at a Bragg reflection, the leakage from the σ-σ channel in σ-π was estimated to be a factor of 350. Thus, by measuring the superlattice intensity in σ-σ it was possible to estimate the leakage in σ-π. Several resonant peaks were observed in the $(h, k, 10)$ plane, but none were detected in the $(h, k, 9)$ plane.

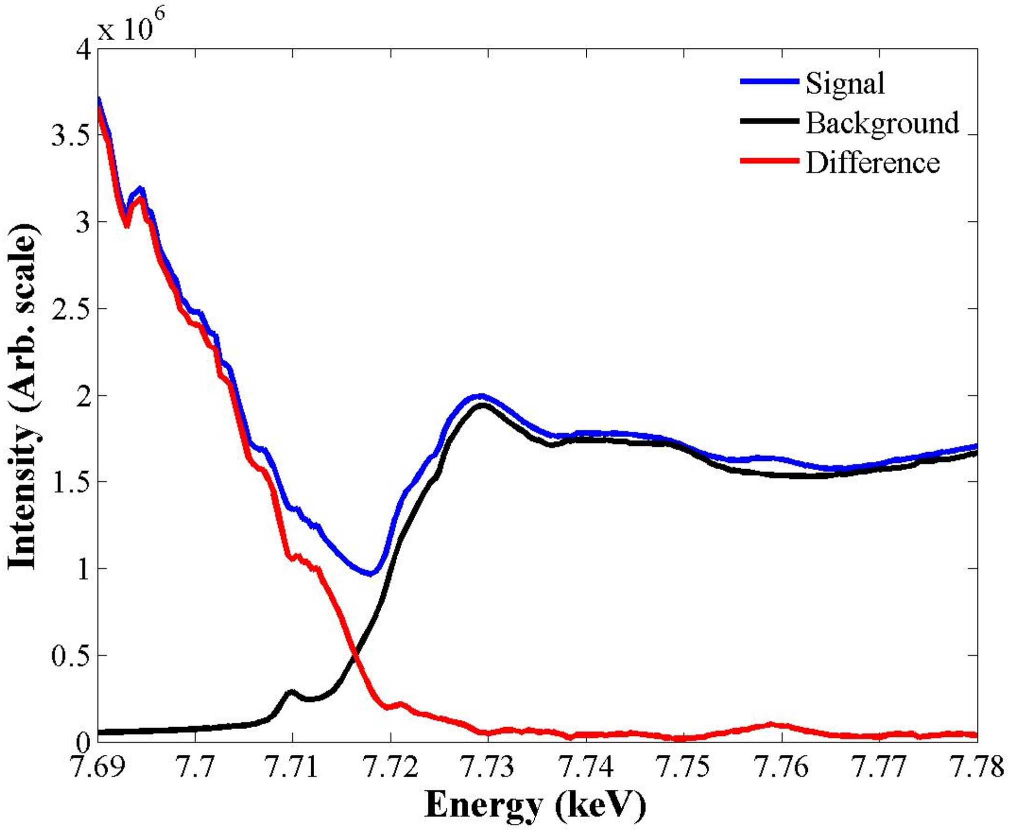

Figure 5.3: Energy scan at $\underline{\mathbf{Q}} = (0.2, 0, 10)$ shows no resonant scattering due to charge ordering.

We performed further measurements on the strongest peaks. Figure 5.5 shows a mesh of θ scans with energy fixed at successive values in the vicinity of the absorption edge for the $(0.2, 0, 10)$ reflection. The fact that it is peaked in both θ and energy confirms that it is resonant scattering. We then measured the temperature dependence of the σ-σ and σ-π channels of the $(0.333, 0.133, 10)$ superlattice peak. Figure 5.6 indicates that the peak disappeared in both channels at about 280K, which corresponds to the phase change from ordered to random stripe phase superlattice [50].

Theta scans were performed on the $(0.333, 0.133, 10)$ peak in σ-π and σ-σ as a function of azimuthal angle. Normalizing the intensity of the σ-π resonance by

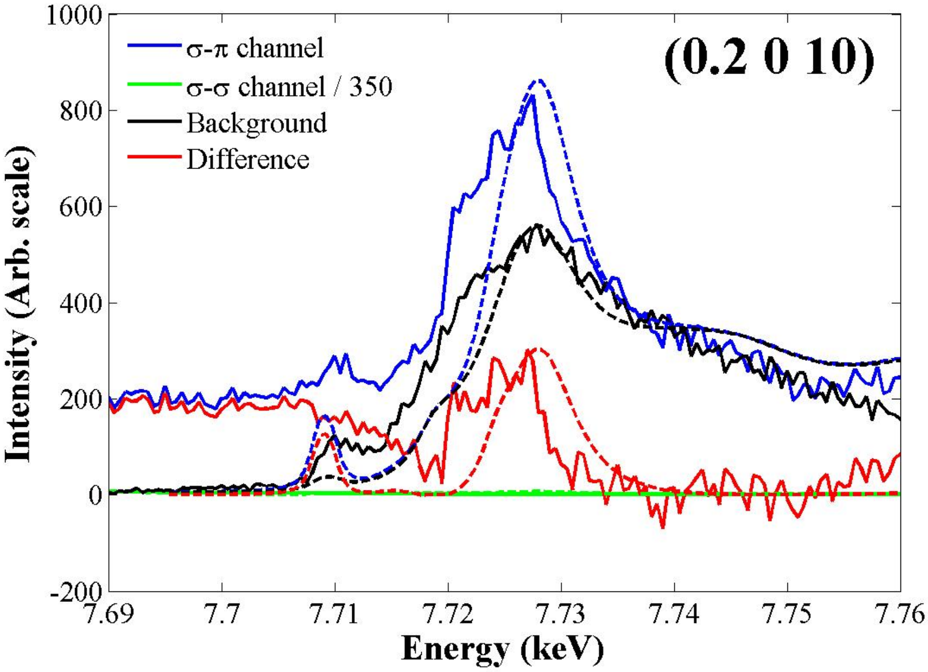

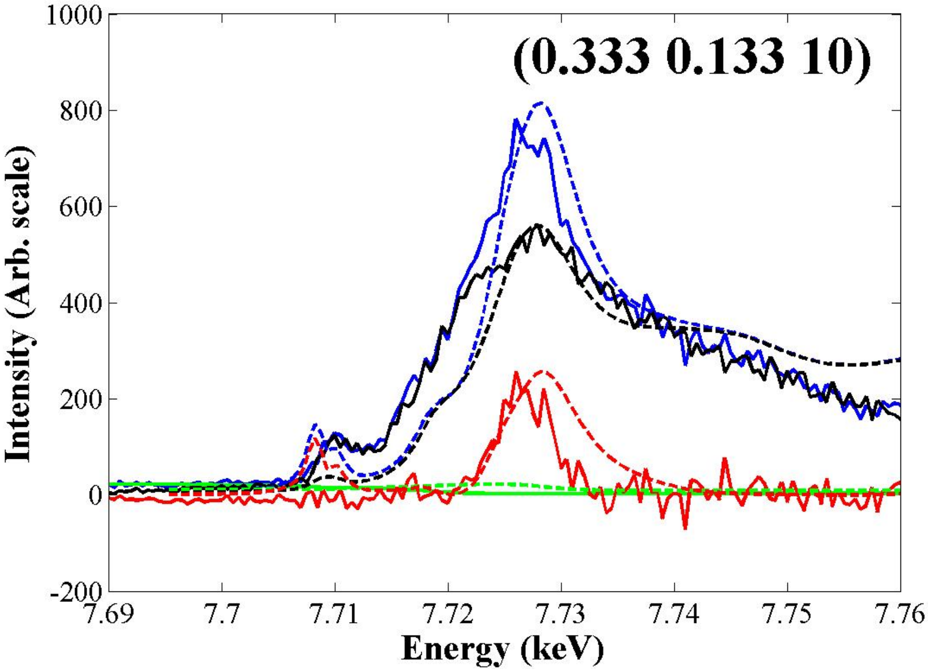

Figure 5.4: Energy scans of $\underline{\mathbf{Q}} = (0.2, 0, 10)$ and $\underline{\mathbf{Q}} = (0.333, 0.133, 10)$ using polarisation analysis. Resonant scattering is observed in the σ-π channel once structural leakage from the σ-σ channel and the fluorescent background are removed, shown in both plots as the red line. In these cases the structural leakage is negligible and the resonant scattering is clearly visible above the florescent background. The dotted lines show the calculated resonant scattering using FDMNES, as described in the text, showing qualitative agreement in both cases.

dividing by the structural intensity in σ-σ, which does not depend on azimuthal angle and accounts for small movements of the beam on the sample surface, shows an oscillating dependence on the azimuthal angle with a period of 100°, as shown in figure 5.7.

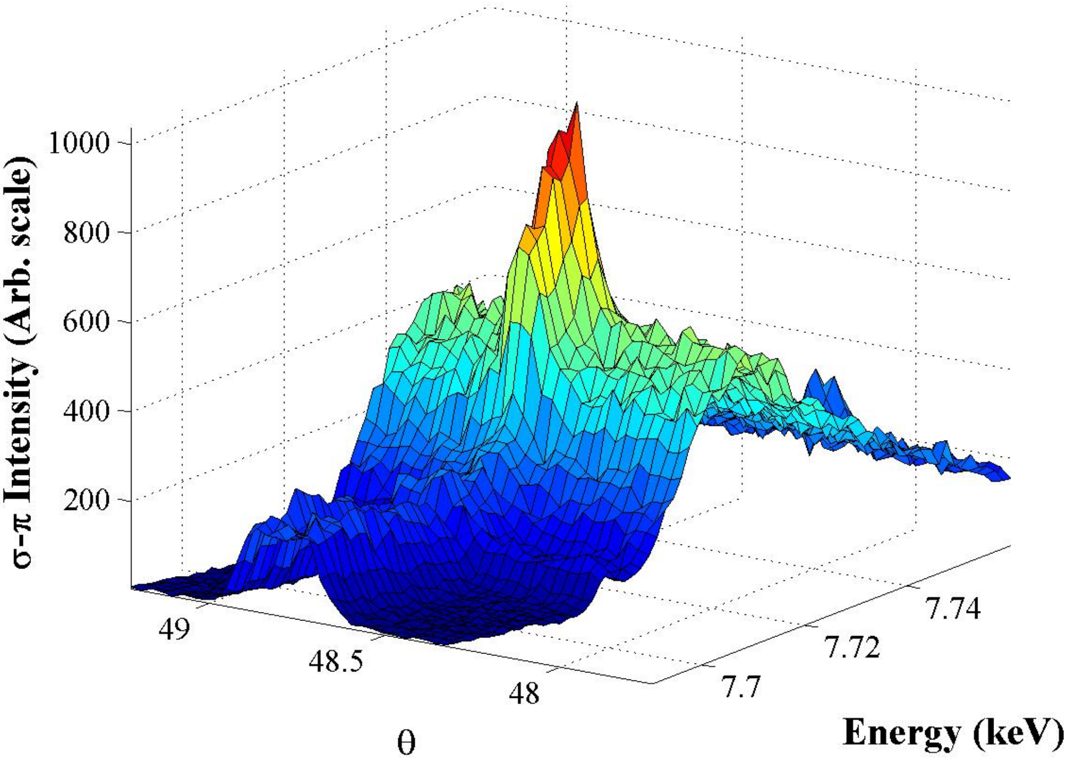

Figure 5.5: Energy-Q scan of $(0.2, 0, 10)$. At each point in energy, a θ scan is performed, showing that the resonance is peaked in both energy and reciprocal space.

FDMNES calculations were performed for cluster radii of 3, 3.5, 5 and 7Å. The calculation with the largest radius of 7Å gives best agreement with the experimental data in figures 5.4 and 5.7. In the case of figure 5.4, the same arbitrary offset in energy is applied to the calculated scans, whereas the azimuthal angles in figure 5.7 are

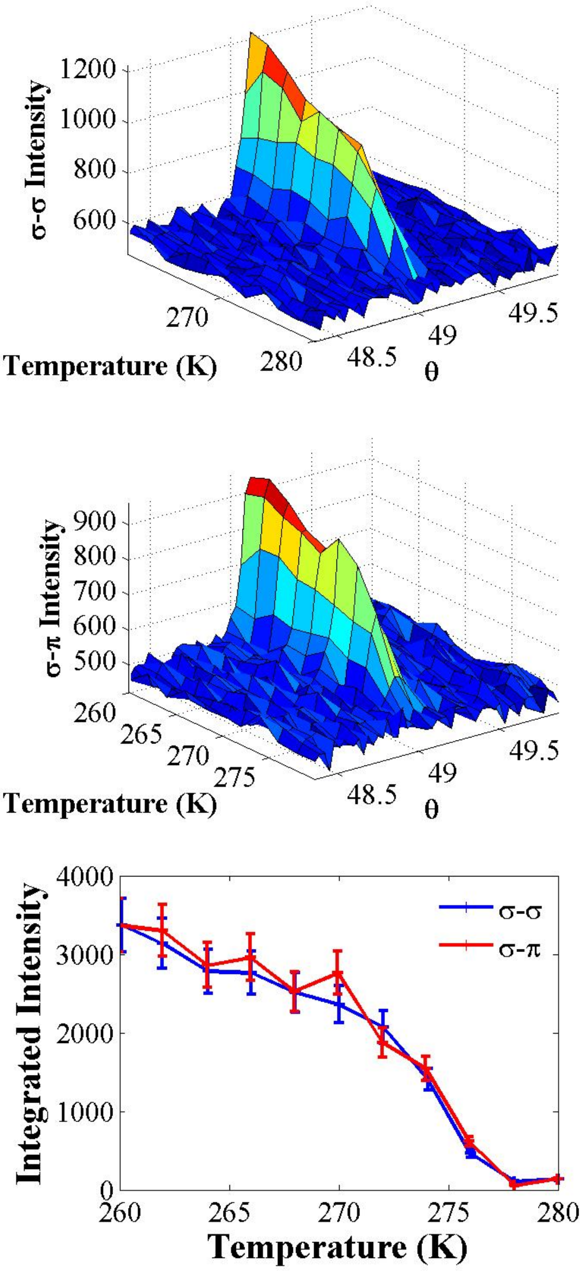

Figure 5.6: Temperature dependence of $\underline{\mathbf{Q}} = (0.333, 0.133, 10)$. The top and middle plots show *theta* scans at each temperature through the σ-σ and σ-π channels respectively. The bottom image shows the normalised, integrated intensity of these peaks, clearly showing the resonant and structural peaks disappearing at 278K.

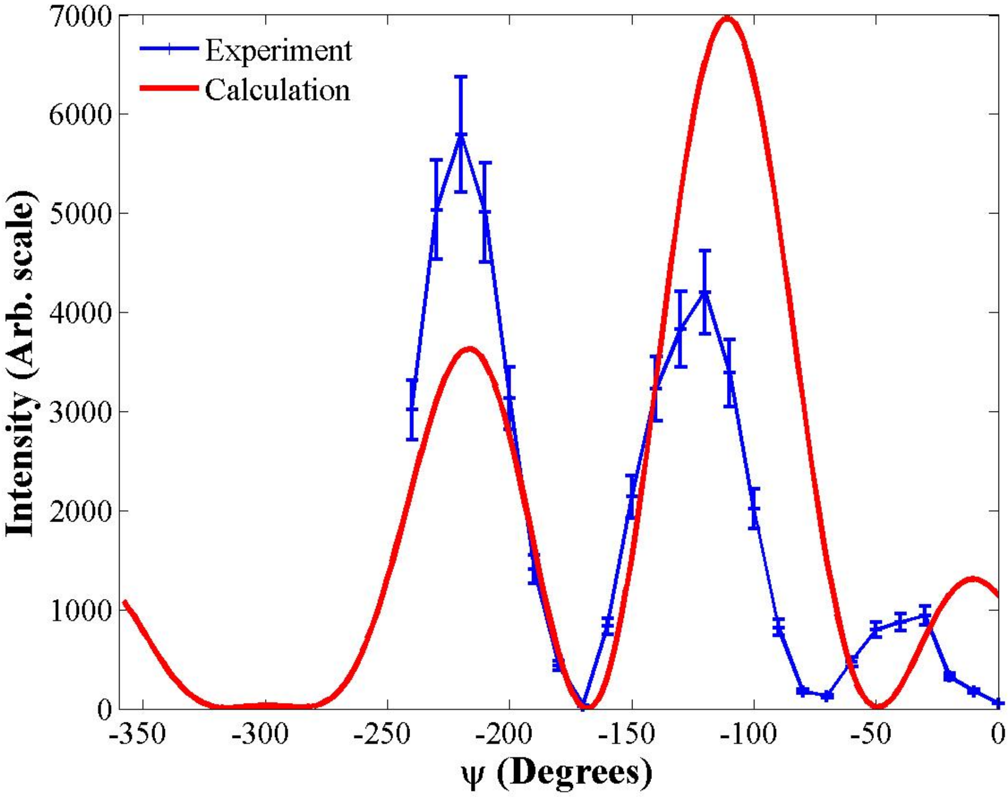

Figure 5.7: Comparison of azimuthal dependence with FDMNES calculations for $\underline{\mathbf{Q}} = (0.333, 0.133, 10)$ with incident energy $E = 7.728keV$. The calculated dependence is scaled to the experimental data by matching the sum under each data set.

absolute. Although the calculation has not converged by this radius, the agreement with the data is encouraging. Unfortunately calculations with a larger radius would be prohibitively long. A better approach would be to perform a calculation for the supercell with periodic boundary conditions. Another potential source of discrepancy between calculation and experiment could be variations in the cobalt-oxygen bond length not picked up in the RMC calculations. However the qualitative agreement without distortions suggests that electronic ordering is the dominant factor in the resonant scattering.

FDMNES also calculates the X-ray Absorption Near Edge Structure (XANES) which is observed experimentally as a Q-independent fluorescent background. XANES measures the total joint density of states of the initial core level with all final states, consistent with conservation rules. It therefore gives useful additional information on the electronic state of the system. Figure 5.4 shows the comparison between the experimental fluorescent background and the XANES calculated with a cluster radius of 7Å. Major features are reproduced, such as the pre-edge peaks and the shoulder on the absorption edge, although there are discrepancies in intensity.

The charge ordering in the cobalt and oxygen planes calculated with a cluster radius of 7Å is illustrated in figure 5.8. Charge stripes are obtained, directly between stripes of tri-vacancy clusters in successive sodium layers. In fact, the qualitative features of this figure are reproduced in calculations for all cluster radii. What is surprising, however, is that the largest variations in charge is not in the cobalt layer, as expected, but on the oxygen. The charge on the cobalt ions only varies between $+3.08e$ and $+3.15e$. In contrast, the charge on the oxygen ions varies by a much larger amount, between $-2.10e$ and $-0.74e$.

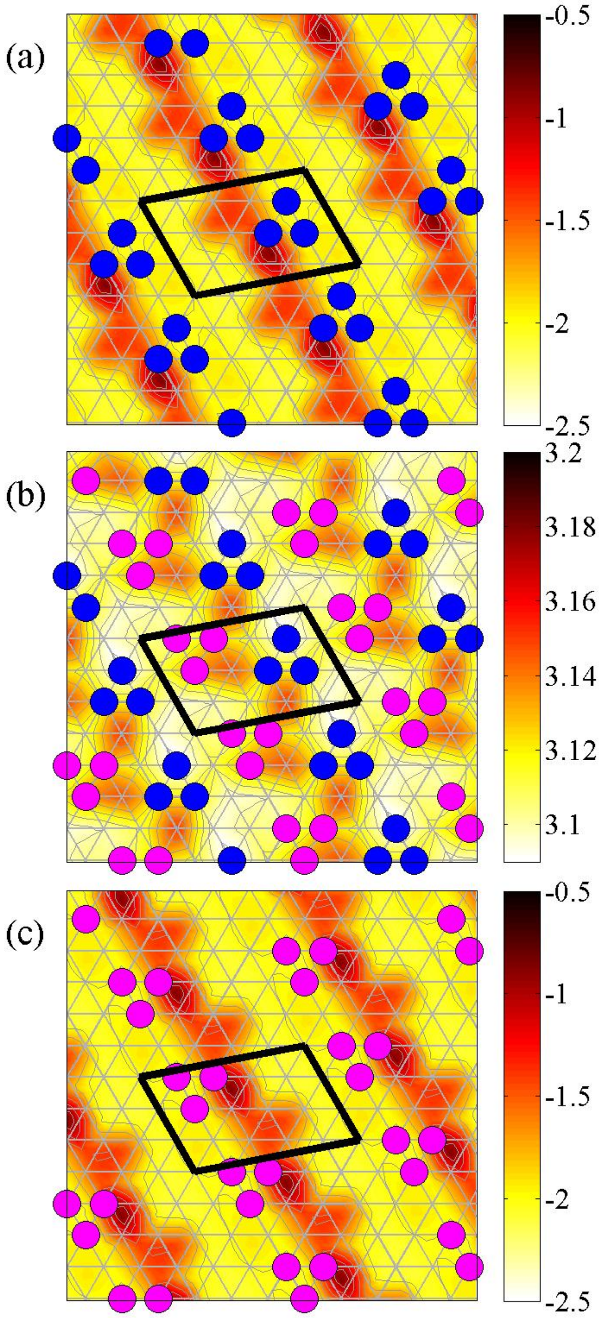

Figure 5.8: 2D map of charges produced by the FDMNES code for the ordered stripe structure. Images (a) and (c) show the charge variation in the oxygen layers above and below the cobalt layer, where large variations in charge can been seen. Image (b) shows the smaller variation in charge within the cobalt layer.

5.5.2 $Na_{0.7}Ca_{0.1}CoO_2$

The single crystal of $Na_{0.7}Ca_{0.1}CoO_2$ was aligned on strong hexagonal Bragg reflections. Figure 5.9 shows structural scattering in the $(h, k, 8)$ plane measured with the PILATUS area detector at $T \approx 10K$. All of the superstructure peaks can be indexed using the di-vacancy superstructure illustrated in figure 4.23. It is clear from the figure that we have a high quality single crystal in a single phase.

We studied the resonant scattering at two superlattice positions, $(0.286, 0.571, 8)$ and $(0.143, 0.286, 8)$, and at a hexagonal Bragg reflection (009), which for structural scattering is a systematic absence.

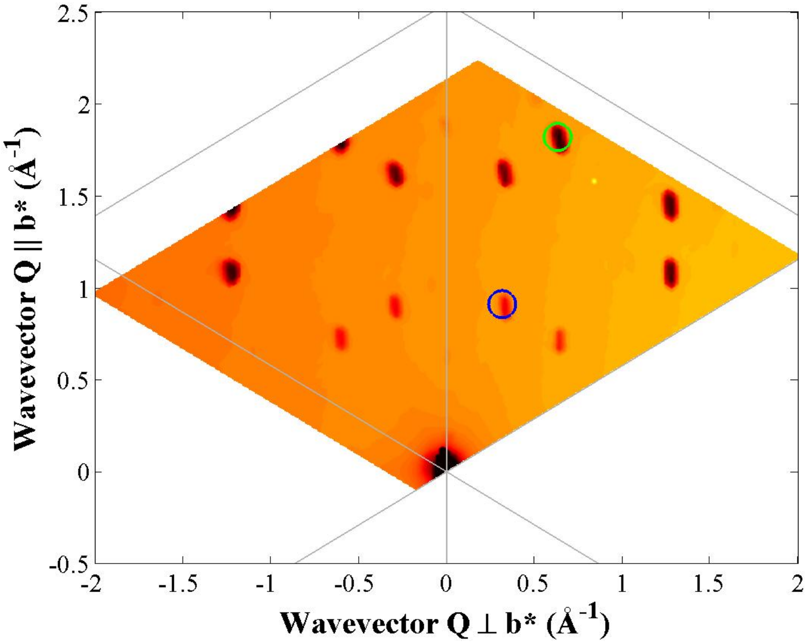

Figure 5.9: Structural scattering in the $(h, k, 8)$ plane at T ≈ 10K for $Na_{0.7}Ca_{0.1}CoO_2$. Superlattice positions $(0.286, 0.571, 8)$ and $(0.143, 0.286, 8)$ from the di-vacancy superstructure in figure 4.23 are circled green and blue respectively.

Figure 5.10 shows the energy lineshapes. In this case the leakage from the structural scattering in the π-π channel is significant, even in the horizontal scattering geometry. Nevertheless, clear resonances are observed after subtraction of the background.

The meshes in energy and Q presented in figure 5.11 show that the main resonances at the absorption edge, and the pre-edge features are resonant scattering. The azimuthal dependence of the scattering was measured at the maximum of the energy scan, and the results are plotted in figure 5.12. Both superlattice reflections oscillate slowly as a function of azimuthal angle, whereas the resonant scattering at (009) exhibits a sinusoidal azimuthal dependence with a period of $\approx 50°$

The temperature dependence of the superlattice reflection at $(0.286, 0.571, 8)$ is presented in figure 5.13. Theta scans were performed at each temperature. Both the π-σ and π-π scattering disappears at $T \approx 350K$, indicating that the resonant scattering is caused by the formation of the di-vacancy superstructure. However, unlike for the pure compound (see figure 5.6) the two order parameters do not overlay. However, it must be noted that temperature stability was an issue in this experiment. The resonance in the π-σ at (009) also disappears at this temperature. Note that there is also a peak in π-π at (009), which does not disappear at high temperature, and this was attributed to multiple scattering.

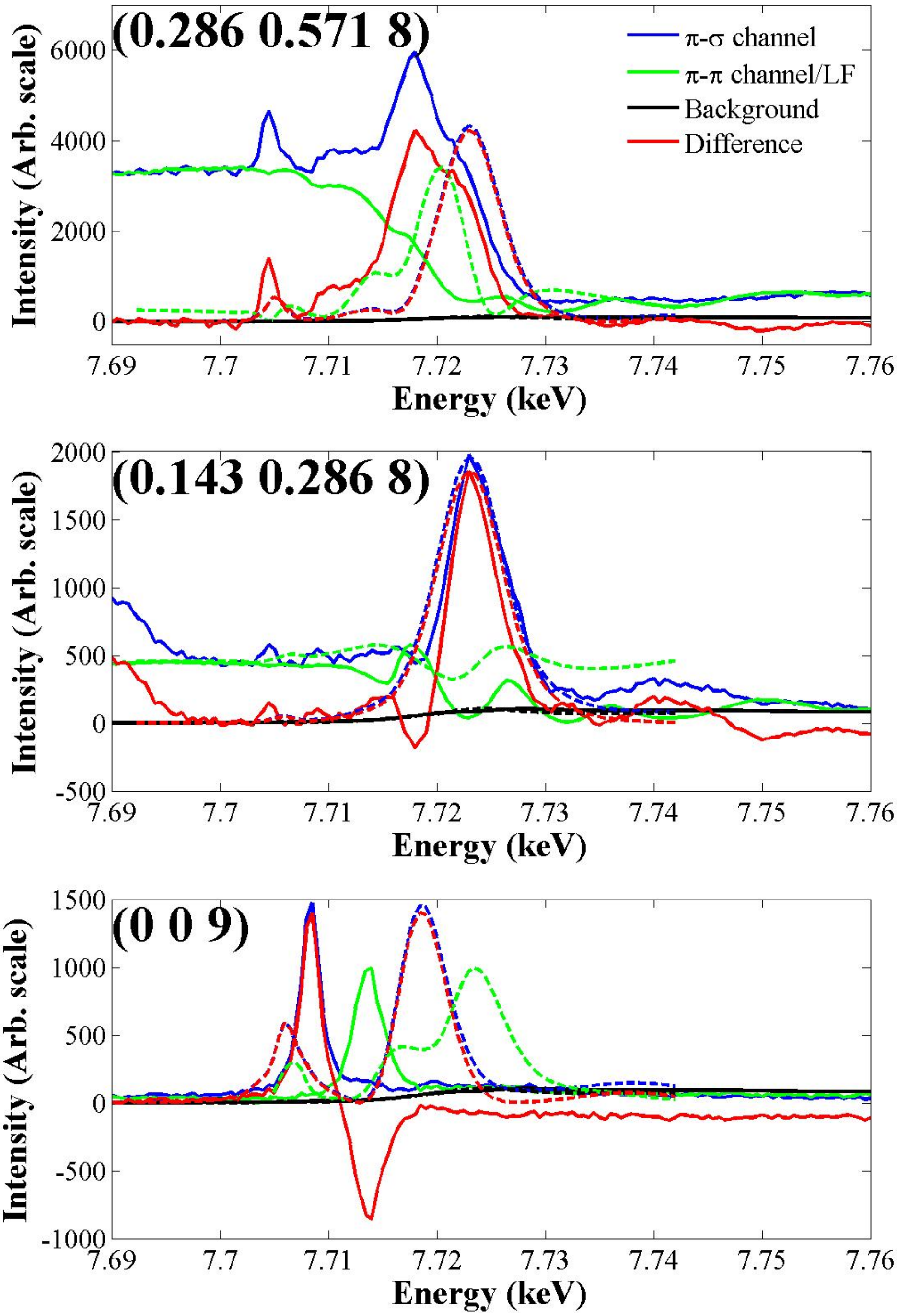

Figure 5.10: Resonant behaviour at various positions for $Na_{0.7}Ca_{0.1}CoO_2$ at T ≈ 10K in the horizontal scattering geometry. For each of the three positions, the π-π leakage and background are removed from the resonant π-σ channel. The leakage factor (LF) is determined by matching the scattering at low energy. Calculations from FDMNES are shown as dotted lines for comparison.

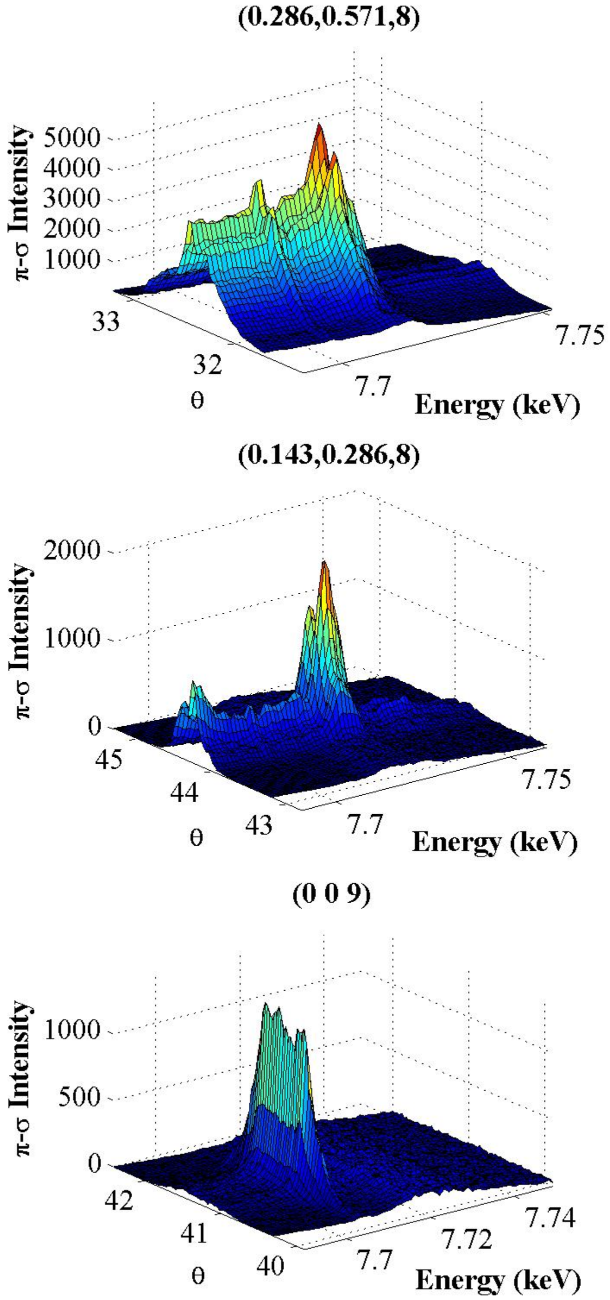

Figure 5.11: Energy-Q meshes for various resonant peaks in $Na_{0.7}Ca_{0.1}CoO_2$ at T ≈ 10K. At each energy, a θ scan of is performed, showing that the main resonance and pre-edge features are peaked in both Q and energy.

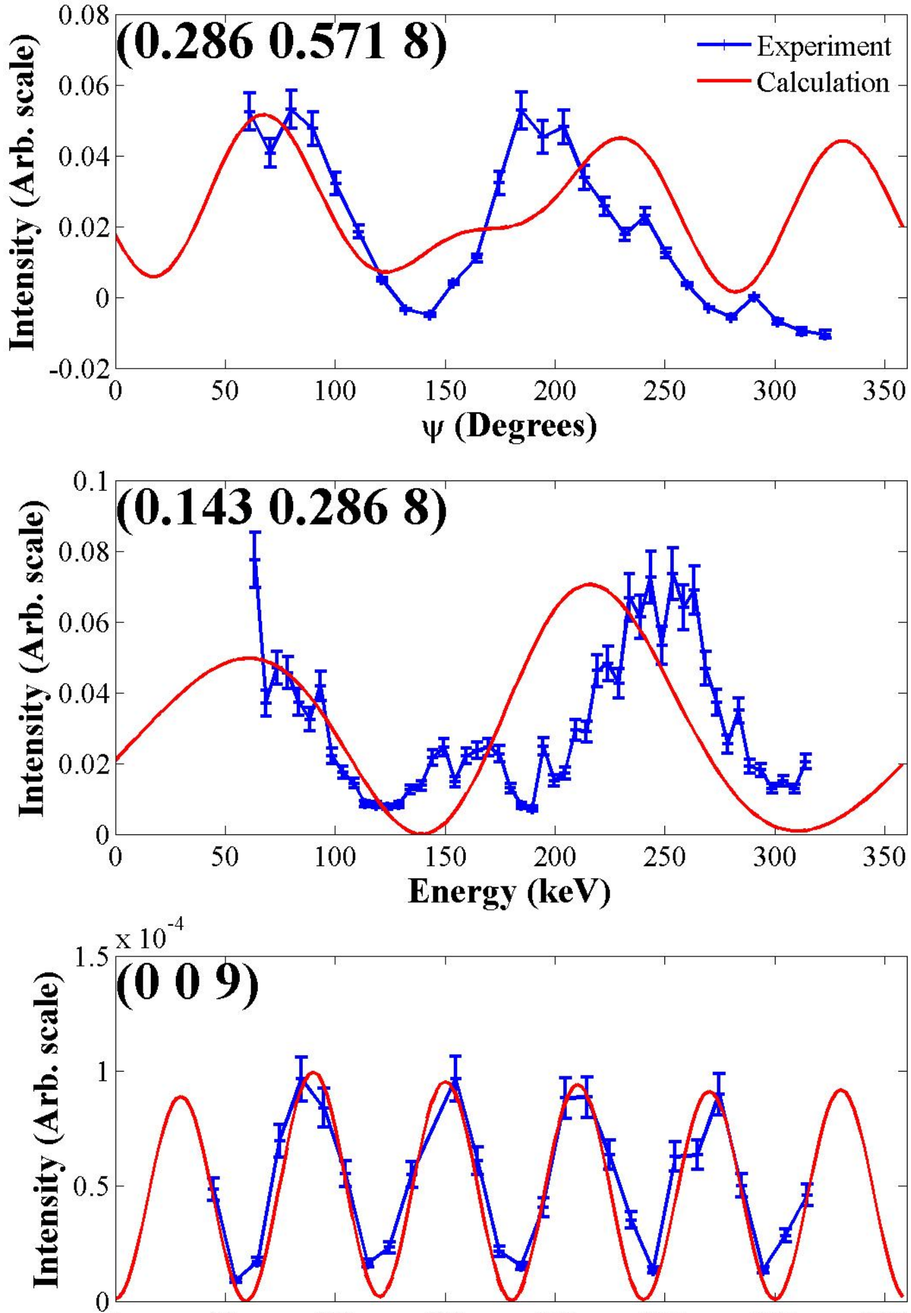

Figure 5.12: Azimuthal dependence of various reflections for $Na_{0.7}Ca_{0.1}CoO_2$ at T $\approx$ 10K. For the superlattice reflections, the resonant π-σ channel is normalized for structural leakage by dividing by the π-π channel. Calculations from FDMNES are shown as red lines for comparison.

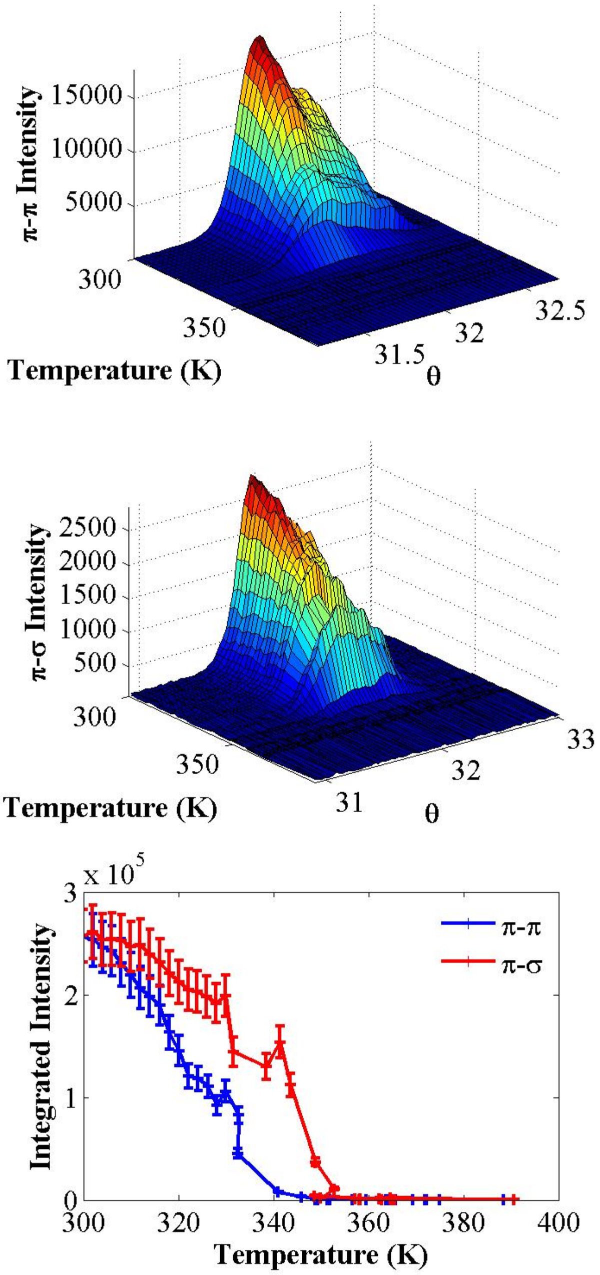

Figure 5.13: Temperature dependence of the structural (π-π) and resonant (π-σ) channels for $\underline{\mathbf{Q}} = (0.286, 0.571, 8)$. The peak disappears in both channels at the same temperature, which is when the sodium layer disorders.

FDMNES calculations were performed using atoms fixed in the positions shown in figure 4.23, with calcium ions occupying the central site in the di-vacancy cluster and with no distortions of the cobalt and oxygen ions. The qualitative agreement between the experimental data in figure 5.10 and 5.12 and the calculations are encouraging, but there are some discrepancies.

In figure 5.10 the offset in energy is determined by the XANES. The main resonance is at the correct energy for the $(0.143, 0.286, 8)$ superlattice reflection, but it is offset in energy for $(0.286, 0.571, 8)$ by 5eV and (009) by 10eV. The azimuthal dependence was calculated at the peak maxima and this lead to good agreement with experiment, see figure 5.12. Note that the quadrupolar correction was required to get agreement with experimental data at (009), indicating that this resonance is related to a quadrupolar transition. The XANES calculation is compared with the experimental data in figure 5.14. The main peak and the pre-edge feature are reproduced, however there is a shoulder on the experimental absorption edge that is not reproduced in the calculation.

FDMNES calculations for the superstructure in figure 4.23, but with sodium on the central sites of the di-vacancy cluster were not able to reproduce the experimental data, even qualitatively. This reinforces the conclusion in chapter 4 that calcium ions occupy this central site.

The charge ordering in the cobalt and oxygen layer determined in the FDMNES calculations is illustrated in figure 5.15. As expected, doping with di-valent ions results in much smaller modulations of charge within the CoO_2 layers, with charges on the cobalt sites varying between $+3.25e$ and $+3.28e$, and the oxygen charges varying between $-2.05e$ and $-1.90e$. Again the modulation in charge is larger on the oxygen sites, and the charge ordering pattern follows very closely the di-vacancy superstructure. In this case a two-dimensional charge order pattern is obtained, rather than the one-dimensional stripes found for the pure compound, however there

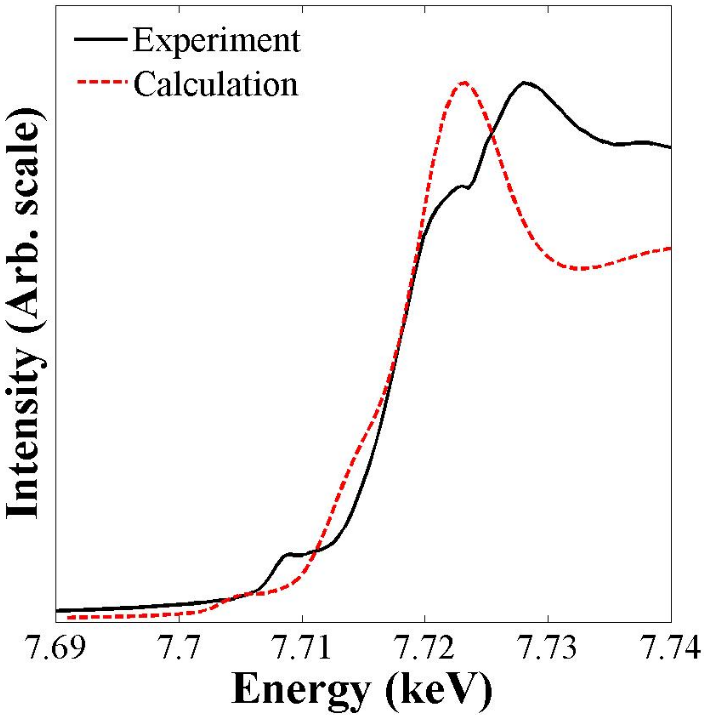

Figure 5.14: Comparison of experimental fluorescent background with XANES lineshape calculated with FDMNES.

are still constricted conduction pathways.

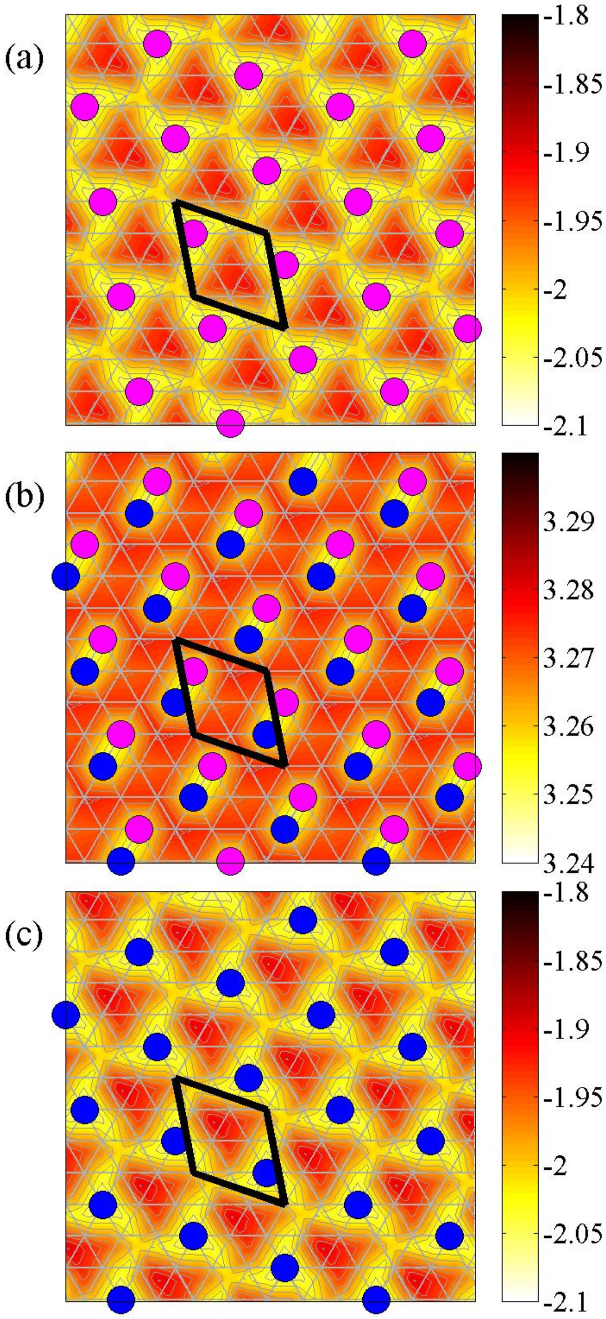

Figure 5.15: 2D map of charges produced by the FDMNES code for the Ca-doped divacancy structure. Overall variation in charges is much smaller than in the pure system, however, the charges of oxygen (top and bottom) and cobalt (center) still follow similar ordering to the sodium ions.

5.6 Discussion

The presence of resonant scattering at superlattice positions clearly demonstrates the correlation between the sodium patterning and the electronic ordering. The fact that the main features of the scattering are reproduced in FDMNES calculations with no distortions of the cobalt and oxygen ions shows that the ordering is primarily electronic rather than due to Jahn-Teller distortions. In these studies we are not directly sensitive to charge ordering, since strong structural scattering obscures the signal in the unrotated channel. Signal in the rotated channel could come from magnetic or orbital ordering. However, the magnitude of the signal rules out magnetic scattering at the cobalt K-edge. Thus the resonant signal originates from ordering of orbitals that arises as a consequence of the superstructure formation. Since charge ordering would be expected to lead to orbital ordering, this is also an indirect measurement of the charge order.

The order of charges predicted in the cobalt and oxygen layers is validated by the general agreement between the FDMNES calculations and the observed resonant scattering. Figure 5.16 compares the charge ordering calculated in the cobalt layer by FDMNES with the electrostatic potential calculated using an Ewald summation of the lattice Coulombic potential. The agreement with this simple model lends further credence to the FDMNES calculations. These calculations all suggest a channel of electrons along stripes. This would be a natural explanation for the strong correlations in the cobaltates, where effective masses are intermediate between those of high-temperature superconductors and heavy fermion materials.

Our FDMNES calculations indicate that the charges order significantly on the oxygen sites. In these calculations the charge on an ion is defined by the electron density within a certain radius. We have performed calculations with different definitions of this radius from the literature, and this leads to a redistribution of charge between oxygen and cobalt. Nevertheless, the presence of substantial charge mod-

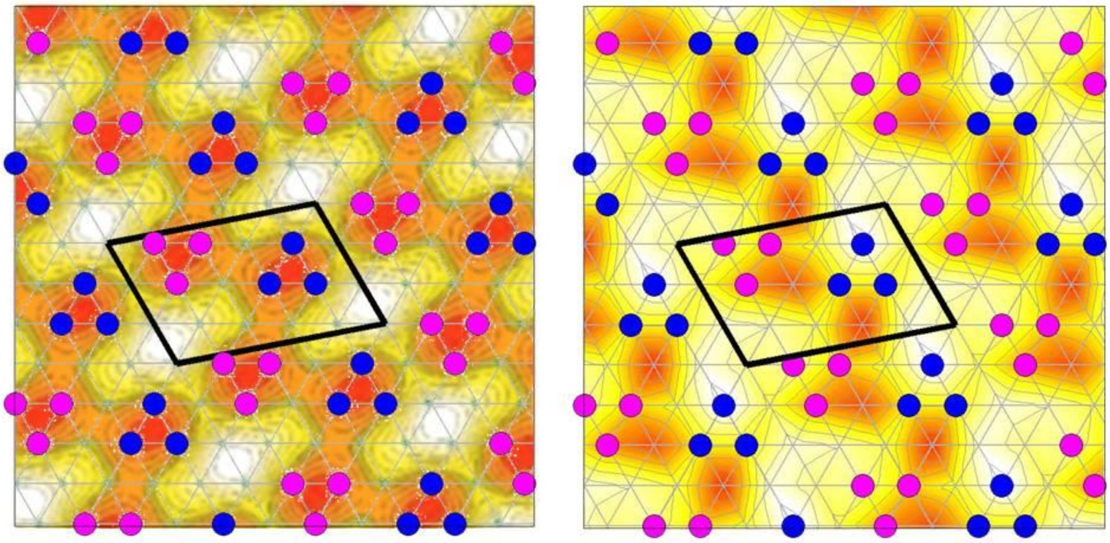

Figure 5.16: Comparison of charges generated by FDMNES in the cobalt layer with the Coulomb landscape from figure 2, Ref. [50]

ulation on the oxygen sites seems to be a robust conclusion from the calculations. This is important for the physics of cobaltates, since it implies that there is at least some screening of the potential on the cobalt ions.

On the basis of NMR measurements from a pure Sodium Cobaltate sample of similar composition to ours, Mukhamedshin *et al.* find substantial variation of cobalt ion valence states [20]. This does not agree with our prediction of a narrow range of valence states for cobalt. However, we speculate that if account was taken of the charge distribution from the oxygen ions, it might be possible to interpret the NMR data with a smaller range of charges on the cobalt site. Our conclusion is very strongly supported by the x-ray absorption results from Valkeapää *et al.* who report a larger change in valence of oxygen than cobalt ions [87]. The qualitative changes to the XANES at the oxygen K-edge as the sodium concentration is varied is reproduced in figure 5.1, and this implies that there must be at least some variation in charge on the oxygen sites. Such charge variation on the oxygen ions has also been observed in other transition metal-oxides, such as Li_xCoO_2 [92] and $La_{1-x}Sr_xFeO_3$ [93]. However, holes in the oxygen ions in these systems are created due to compensation from a change in composition (such as changing x in Li_xCoO_2) and as such do not produce a change in valence as large as the change predicted by FDMNES here.

Our resonant x-ray scattering results have provided important information on the electronic ordering in cobaltates. However, we cannot claim perfect agreement between the FDMNES calculations and the experimental data. The calculations as a function of cluster radius have not reached convergence by 7Å and, unfortunately, the large supercells make the CPU time for calculations with a sufficiently large radius prohibitive. Calculations with periodic boundary conditions are in progress, but even these are likely to be imperfect due to the limitations in modelling strongly correlated systems by Density Functional Theory. It is also possible that Jahn-Teller distortions beyond our detection limit using RMC could improve the fit to the data. The agreement for the calcium doped sample is worse. This seems reasonable since perfect occupation of the central di-vacancy site by calcium is not possible for this composition. This must lead to some disorder, and we know that altering the occupancy of these sites dramatically changes the resonant scattering.

5.7 Conclusions

In summary, we measured single crystals of $Na_{0.8}CoO_2$ and $Na_{0.7}Ca_{0.1}CoO_2$ in reflection geometry using I16. We were able to study the resonant x-ray scattering at the cobalt K-edge for the ordered stripe phase and calcium doped di-vacancy phase. Unpolarised energy scans did not detect charge ordering peaks at the Co absorption edge, however, energy scans in the rotated polarisation channels did show resonant peaks at the absorption edge in both systems, which could be evidence for orbital or other electronic ordering. We can rule out this resonance being magnetic because we are at an even plane in reciprocal space, where the expected antiferromagnetic structure should only allow magnetic effects in the odd planes, and also the magnetic resonant scattering is expected to be small at the cobalt K-edge. Temperature dependence of these peaks found that the electronic transition occurs at the same temperature as the structural transition from ordered to disordered stripes, meaning that these resonances are clearly related to the sodium ordering.

In order to understand this complex resonant behaviour, the FDMNES code was used. These calculations are able to reproduce qualitative features of the experimental datasets, although finer calculations are required to reproduce the observed data accurately. This sort of agreement is not uncommon in the resonant scattering field and better comparisons are unlikely to be found without advances in instrumentation and modelling techniques. The electronic ordering proposed by the FDMNES calculations shows an ordering of charges within the cobalt-oxygen layers that is clearly correlated with the patterning of sodium ions. However, it was found that the largest charge variation was around the oxygen ions, rather than cobalt, where previous work has predicted charge ordering. The clear similarities between the experimental and calculated resonant spectra imply that the electronic patterning proposed by FDMNES may have some truth to it, and this clearly reinforces the theory that the ordering of the sodium layer is controlling the electronic properties of the system. If these calculations are accurate it has profound implications on the understanding of the properties of Sodium Cobaltate as this would imply that the conduction of electrons though the system is travelling through the oxygen layers. Also, the striped nature of the ordering in $Na_{0.8}CoO_2$ would confine these conduction pathways to one dimension, which is likely to lead to increased interaction between the electrons and therefore strong correlations, which may assist in the explanation of the large Seebeck coefficient observed in this system.

Chapter 6

Physical Properties

6.1 Abstract

The thermoelectric properties of $Na_{0.8}CoO_2$, $Na_{0.57}Ca_{0.14}CoO_2$ *and* $Na_{0.7}Sr_{0.1}CoO_2$ *were measured using the PPMS at Royal Holloway. A particularly high thermopower was obtained for the pure compound, possibly due to the channelling of electrons along stripes. The calcium doped sample has an ideal composition for its superstructure and, as a consequence, it is found to have a very high thermal conductivity. Magnetic susceptibility measurements reveal antiferromagnetic order at low temperatures for each system. There appear to be additional transitions at lower temperatures for the doped systems. The magnetic ordering is studied using polarised neutron diffraction for the pure compound. An A-type antiferromagnet structure is observed but no modulation within the plane is detected.*

6.2 Background

The discovery of low electrical resistivity and remarkably large thermopower for single crystals of $Na_{0.5}CoO_2$ by Terasaki *et al.* has generated intense interest in this family of transition-metal oxides as candidates for thermoelectric applications [11]. The Seebeck coefficient of about $100\mu V/K$ at room temperature is an order of magnitude larger than that of typical metals. It was subsequently found that significantly enhanced thermoelectric performance could be achieved for Na_xCoO_2 at high x [7]. Figure 6.1 shows the current state-of-the-art for thermoelectric properties for pure Sodium Cobaltate. The power factor, S^2/ρ, for Na_xCoO_2 increases as x increases and the concentration of holes in the cobalt-oxide layers decreases, until $x \approx 0.85$, where phase separation into the insulating $x = 1$ phase occurs, as described in figure 4.3.

The substitution of a divalent ion for sodium decreases by one the number of holes in the cobalt-oxide layer. This offers the possibility to lower the concentration of holes beyond what is possible for the pure compound, and to further enhance thermoelectric performance. There are already promising results on polycrystalline samples doped with calcium and strontium, with an increase of the power factor by 50% over the comparable pure compound, as previously described in figure 4.5.

The aim here is to measure the thermoelectric properties of pure and doped compounds with well characterised superstructures.

The strong interplay between the magnetic and superconducting properties of hydrated Sodium Cobaltate has led to close comparison with the physics of the superconducting copper oxides [5]. The character of the cuprates can be altered by subtle changes in composition. For example, superconductivity in $La_{2-x}Ba_xCuO_4$ reaches a maximum transition temperature, T_c, of 30K at $x = 0.10$ and 0.15, but it is almost completely suppressed at $x = 0.125$. This effect is due to a static superstructure of spin and charge stripes which forms on the copper-oxide layers commensurate with the crystal lattice [94].

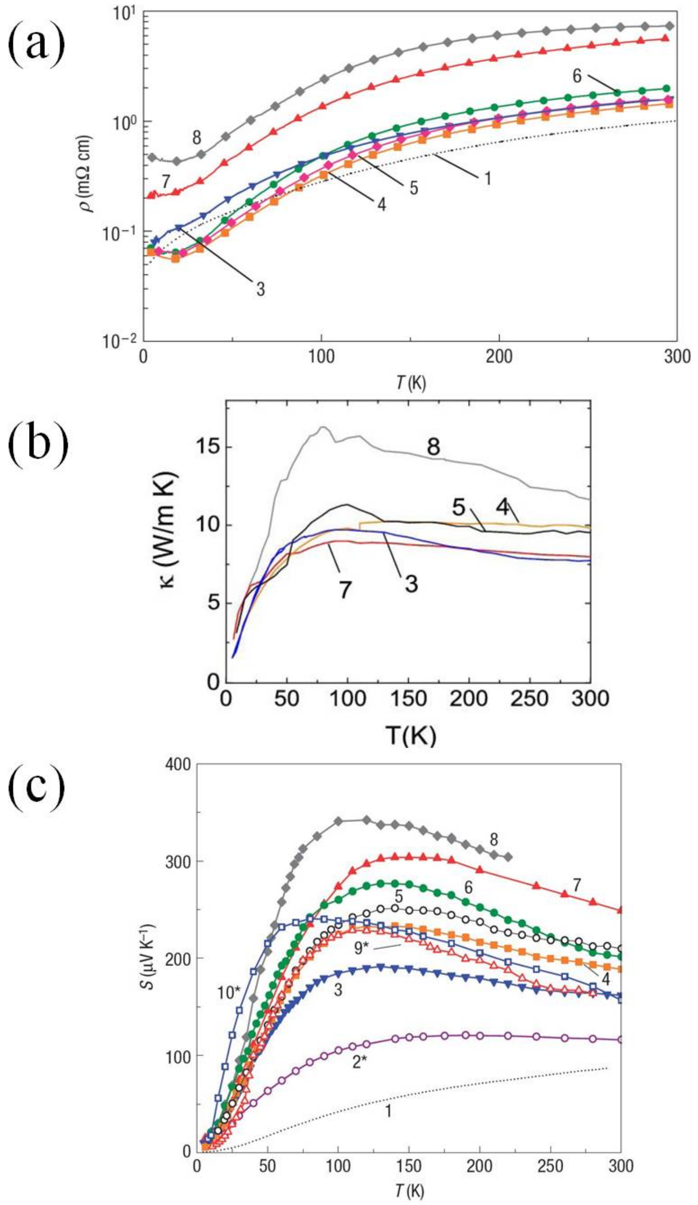

Figure 6.1: State-of-the-art thermoelectric properties for Sodium Cobaltate, from figures 1, 2 and S2, ref. [7]. **(a)** In-plane resistivity versus temperature in log-linear scale. **(b)** Curves of the in-plane thermal conductivity. **(c)** The in-plane thermopower. Each line represents a different concentration, numbered in order of increasing x: 1 ($x \approx 0.71$), 2* ($x \approx 0.75$), 3 ($x \approx 0.80$), 4 ($x \approx 0.85$), 5 ($x \approx 0.88$), 6 ($x \approx 0.89$), 7 ($x \approx 0.96$), 8 ($x \approx 0.97$), 9* ($x \approx 0.99$), 10* ($x \approx 1.0$). The asterisks indicate the three-layer crystals.

The magnetic ordering in pure Sodium Cobaltate has been studied using neutron diffraction, but the experiments are challenging since the magnetic intensity occurs on top of structural scattering. Figure 6.2 shows the magnetic scattering obtained for a single crystal of $Na_{0.5}CoO_2$ using unpolarised neutron diffraction [95]. The proposed magnetic structure comprises antiferromagnetic stripes of large in-plane moments interleaved with stripes of much weaker moments parallel to the c-axis. This magnetic ordering is superimposed on the Coulomb landscape calculated from the sodium superstructure in figure 6.3. Although some details of the magnetic structure could not be resolved in this experiment, it is clear that the sodium superstructure plays a decisive role.

Bulk magnetic susceptibility measurements indicate that Na_xCoO_2 orders antiferromagnetically over a wide composition range at high-x, with a Néel temperature $T_N \approx 22K$ [96, 97, 98]. Determining the magnetic structure at high-x using neutron diffraction proved difficult to the extent that details of the magnetic excitations emerged before it was possible to say anything about the magnetic order [99]. In fact, the magnon dispersion is very surprising, since it indicates that the interlayer exchange interaction is comparable to the in-plane exchange constant [100, 8]. The solution of the magnetic structure required the use of polarised neutrons, and an A-type antiferromagnetic order was proposed, with ferromagnetic sheets of moments pointing along the c-direction [8], as described in figure 6.4.

Thus, in this chapter, in addition to the bulk thermoelectric properties, I shall describe bulk magnetic susceptibility studies of pure and doped Sodium Cobaltate. The pure compound is in a well-defined superstructure, the ordered stripe phase. In this case the magnetic ordering was investigated further using polarised neutron diffraction.

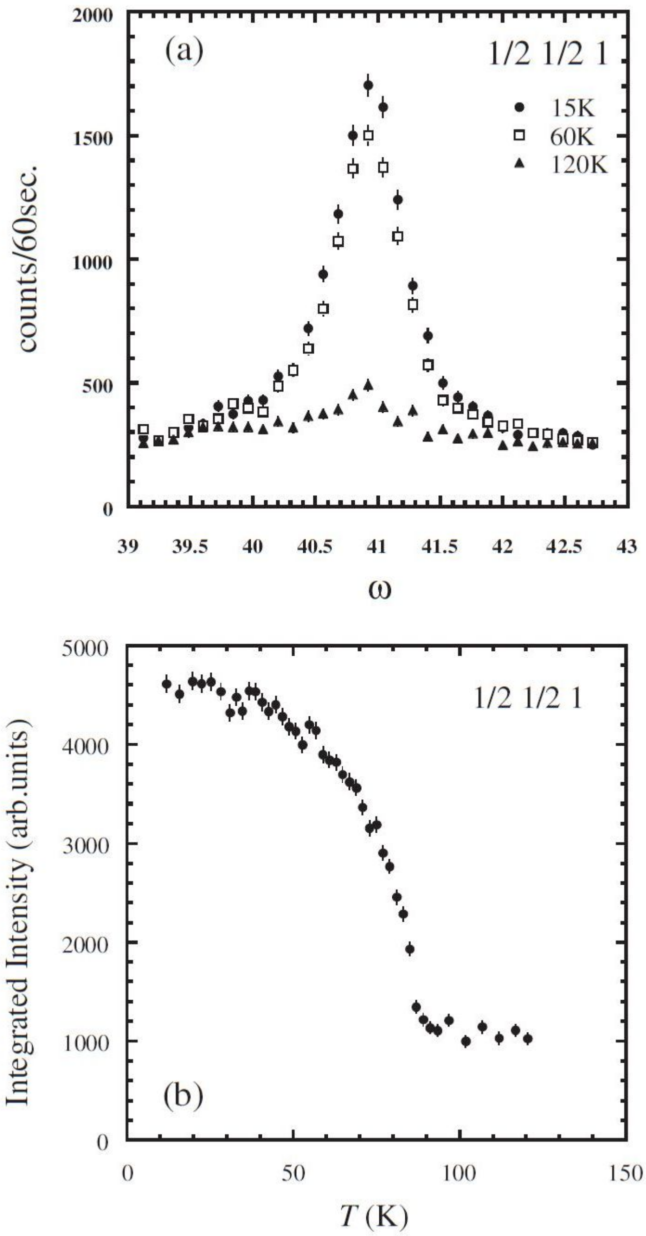

Figure 6.2: Unpolarised neutron scattering measurements of $Na_{0.5}CoO_2$ at the superlattice $(\frac{1}{2}\frac{1}{2}1)$ position from figure 11, ref. [95]. **(a)** Profiles of ω (θ) scans. **(b)** Temperature dependence of integrated intensity. Temperature dependence and comparison of intensities to a magnetic model infer that this superlattice peak is magnetic.

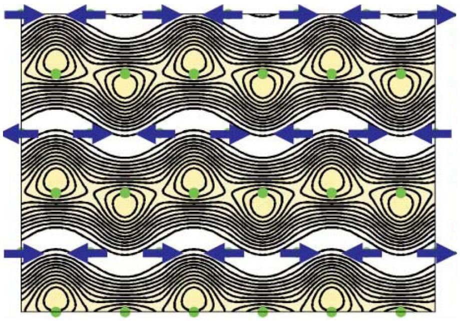

Figure 6.3: Coulomb potential in the cobalt plane calculated using ordered superstructure of $Na_{0.5}CoO_2$, from figure 4(a), ref. [70]. Green dots show the positions of cobalt ions and the proposed magnetic order is shown as blue arrows.

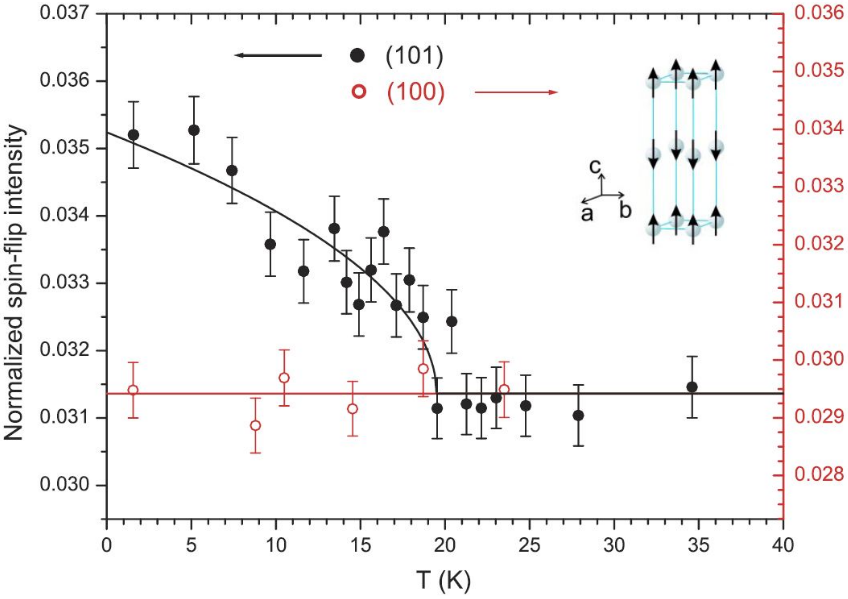

Figure 6.4: Polarised neutron measurements of $Na_{0.82}CoO_2$ from figure 1, ref. [8]. Normalised SF intensity at (101) and (100) as a function of temperature, showing a clear transition at $T \approx 20K$. Inset is the proposed A-type antiferromagnetic model.

6.3 Experiment Procedure

6.3.1 Thermoelectric properties

Transport measurements were performed using a Quantum Design PPMS at Royal Holloway. Long and thin samples of $Na_{0.8}CoO_2$ and $Na_{0.57}Ca_{0.14}CoO_2$ were mounted on a purpose built puck using copper contacts and silver epoxy glue, as shown in figure 6.5. The puck allowed simultaneous measurements of resistivity, thermal conductivity and the Seebeck coefficient from 300K to 2K, and from these three measurements, the thermoelectric figure of merit could be calculated. The puck was calibrated using a nickel sample and the results obtained were consistent with standard nickel measurements.

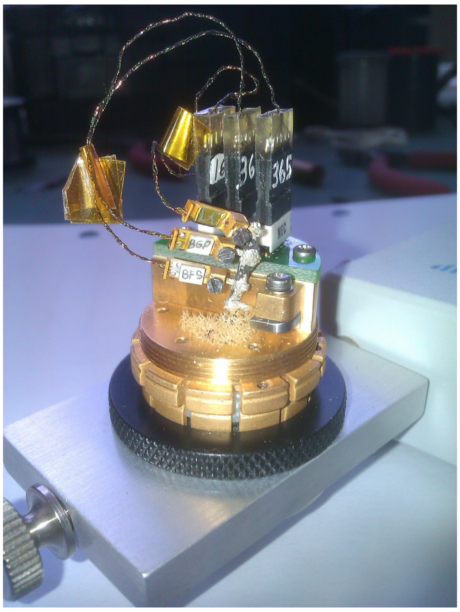

Figure 6.5: Thermal transport puck with $Na_{0.8}CoO_2$ sample mounted. Four sample leads are connected using silver glue, allowing simultaneous measurement of resistivity, thermal conductivity and the Seebeck coefficient.

The smaller $Na_{0.7}Sr_{0.1}CoO_2$ sample, studied on SXD, was measured with similar apparatus by Dr Florence Albenque-Ruillier in CEA Sacleay.

6.3.2 Magnetic properties

Using a Quantum Design SQuID VSM (Superconducting Quantum Interference Device, Vibrating Sample Magnetometer) magnetic properties measurement system at Diamond, we were able to measure the magnetic properties of three single crystal samples of Sodium Cobaltate. These were a standard sample of $Na_{0.8}CoO_2$ (unscreened but from a high quality boule) and the two doped samples previously measured with neutrons on SXD, $Na_{0.7}Sr_{0.1}CoO_2$ and $Na_{0.7}Ca_{0.1}CoO_2$. Each sample was measured with the field parallel and perpendicular to the c-axis, and in each orientation the sample was cooled with (FC) and without (ZFC) an external field of 200Oe. A magnetic field hysteresis loop of each sample was also performed below the magnetic transition.

6.3.3 Magnetic structure

Large $\approx 1g$ single crystals of $Na_{0.8}CoO_2$ were studied by elastic magnetic scattering using polarised neutron diffraction on IN20. All of the magnetic peaks are expected to coincide with structural reflections and, therefore, polarisation analysis was required to separate the magnetic signal. The full three-dimensional polarisation analysis of CRYOPAD (Cryogenic Polarisation Analysis Device) was employed, see section 2.2.5 for a description of CRYOPAD. By measuring a combination of diagonal spin-flip intensities it is possible to isolate the magnetic signal. Because the magnetic order and the structure are expected to have the same periodicity it may be possible to obtain enhanced sensitivity to the magnetism via magnetic-nuclear cross terms that appear in off-diagonal terms. Measurement of the full polarisation matrix potentially gives additional information on the magnetic order, for non-collinear structures.

It is not possible to tilt the sample when it is mounted on CRYOPAD. The sample was, therefore, pre-aligned with an $(h0l)$ horizontal scattering plane on IN3, before transfer to CRYOPAD. The sample was cooled to $T \approx 2K$, where the polarisation matrix was measured. Selected reflections were studied as a function of temperature to see how the intensity varies through the ordering temperature T_N.

Previous studies have focused on the magnetic scattering at hexagonal reflections [8] and, therefore, they were not sensitive to the possibility of magnetic modulations in the plane. Thus, in addition to studying the magnetic scattering at hexagonal reflections for a sample with a known superstructure, we also measure the signal at superlattice peaks in an attempt to study the in-plane magnetic ordering.

6.4 Results & Discussion

6.4.1 Thermoelectric properties

The results of the electrical and thermal transport measurements at Royal Holloway were found to vary substantially for different samples of the same nominal composition, taken from the same boule. Measurements of the Seebeck coefficient were found to be more reproducible. In some cases there were problems in mounting small samples, due to the poor quality of the crystal surface and weak bonding of the silver glue. The main source of variation is believed to be crystal quality, as several mounting techniques were attempted and all exhibited the same variation in results. It is difficult to obtain pristine crystals of Sodium Cobaltate and, therefore, scattering at grain boundaries is likely to be a problem. We decided to focus on the best electrical and thermal conductivity measurements that showed consistent behaviour on cooling and heating and no anomalous readings or jumps in the data, since these are most likely to reflect intrinsic physical properties. The independent measurements of the strontium doped sample are broadly comparable, and this suggests that the results reported here are at least qualitatively reliable.

Figure 6.6 compares the electrical resistivity, thermal conductivity and Seebeck coefficient for $Na_{0.8}CoO_2$, $Na_{0.57}Ca_{0.14}CoO_2$ and $Na_{0.7}Sr_{0.1}CoO_2$ over the temperature range $T = 2 - 300K$.

The electrical resistivity is an order of magnitude worse than the values reported by Lee *et al.* for pure Sodium Cobaltate [7] and Li *et al.* for calcium and strontium doped systems [82]. The pure crystals of Lee *et al.* were less than $1mm$ in size and, therefore they may have been higher quality than our much larger crystals of size a few mm. Our residual resistance ratio is considerably less than the value of $RRR \approx 20$, reported by Lee *et al.* This explanation would not appear to be appropriate for the doped systems, since the samples investigated by Li *et al.* were

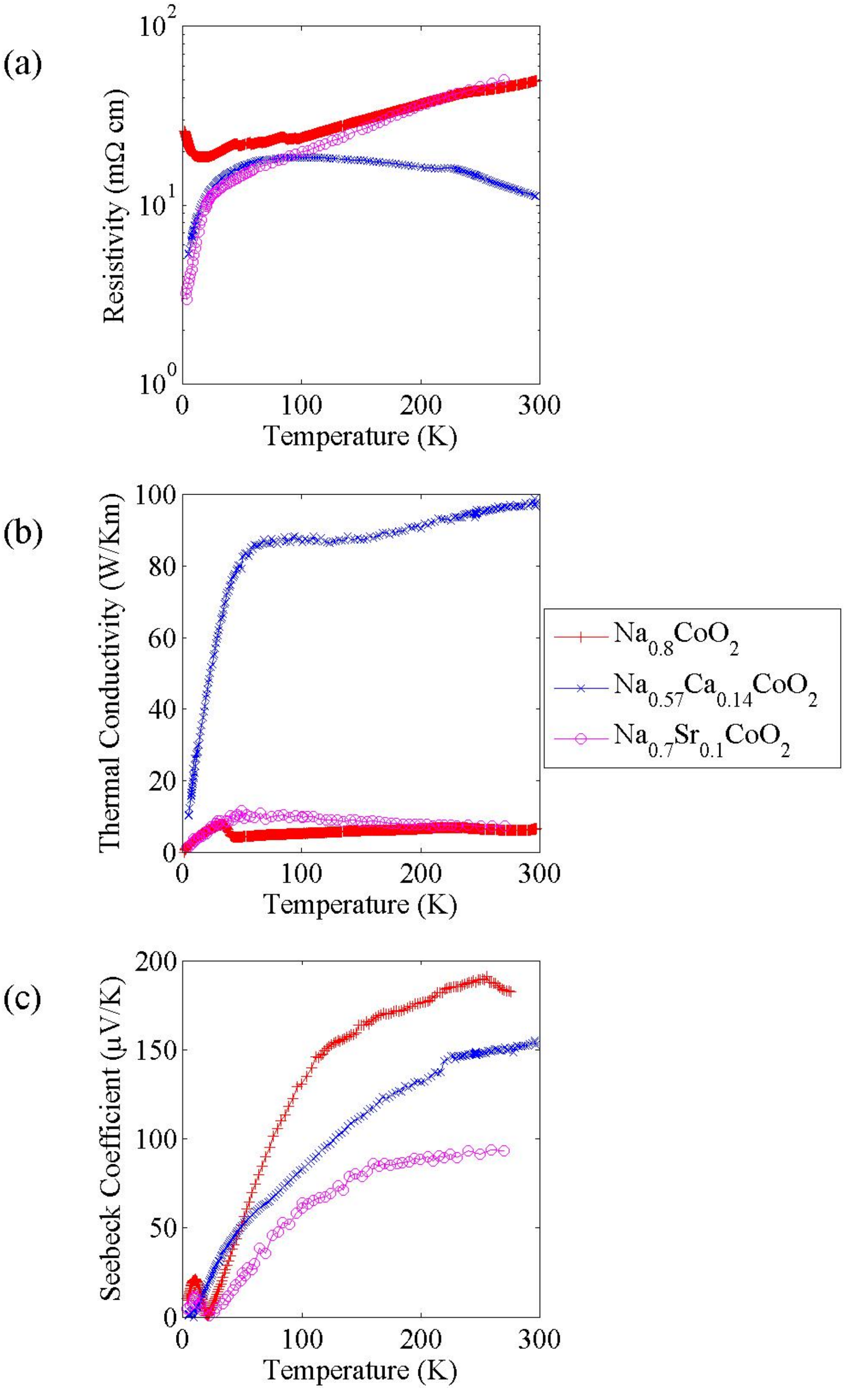

Figure 6.6: Thermal transport measurement results for different systems.

sintered powders rather than single crystals!

The thermal conductivity of $Na_{0.8}CoO_2$ and $Na_{0.7}Sr_{0.1}CoO_2$ are comparable to those reported for the pure system at high-x by Foo *et al.* and Lee *et al*, see figure 6.1 [6, 7]. However, the thermal conductivity of $Na_{0.57}Ca_{0.14}CoO_2$, $\approx 100W/mK$, is exceptionally large. This is the ideal composition for the particular di-vacancy superstructure observed in this system. Furthermore, the structural determination described in chapter 4 indicates that this sample is of very high crystal quality. Since it is single phase, the lack of disorder from the ideal superstructure may lead to long phonon mean free paths and, therefore, a high thermal conductivity. This is detrimental for the thermoelectric performance. Thermal conductivity measurements of a sample with increased calcium content indicated that moving away from the ideal composition lowers the thermal conductivity.

The Seebeck coefficients in figure 6.6 are comparable to the best achieved previously for both pure and doped system. The trend, with the pure system best, then calcium doped followed by the strontium doped is the opposite to that reported by Li *et al.* However, the precise compositions used by Li *et al.* were different, and the superstructures are also very likely to be different. One remarkable feature of our data is that the Seebeck coefficient dips to zero at low temperature for $Na_{0.8}CoO_2$ and $Na_{0.7}Sr_{0.1}CoO_2$, shown clearly in figure 6.7. We do not currently have an explanation for this behaviour. However, we note that both samples have similar striped superstructures.

The overall figure-of-merit, $ZT = TS^2/\rho\kappa$, is summarised for the three systems in figure 6.8. The highest value obtained is $\approx 2 \times 10^{-3}$, which is much lower than expected in these systems, given their large Seebeck coefficients and lower than the value of $ZT = 1$ that was hoped for. However, the worse electrical conductivity of our samples entirely accounts for the difference between these results and the

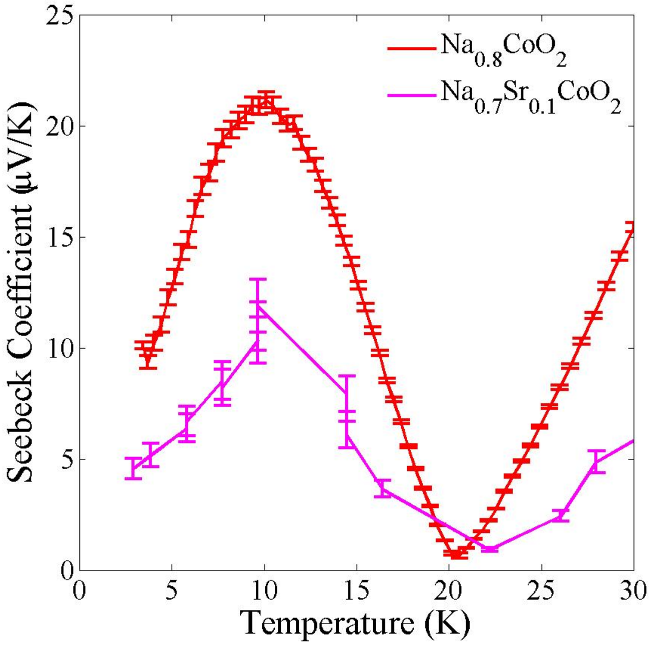

Figure 6.7: Low temperature behaviour of the Seebeck coefficient in the pure and strontium doped systems, demonstrating a remarkable dip at approximately 20K

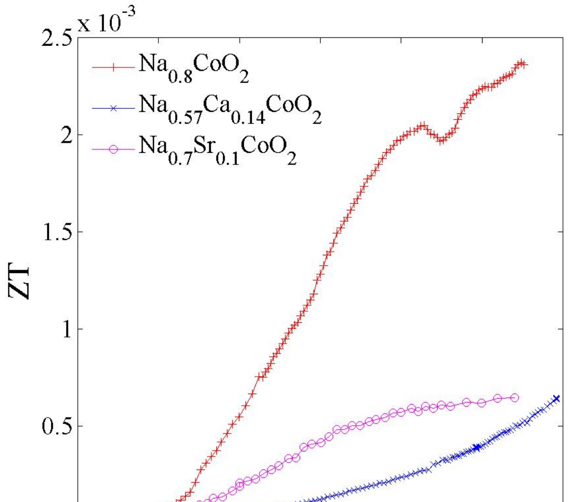

Figure 6.8: Calculated thermoelectric figure of merit, $ZT = TS^2/\rho\kappa$, for the three systems.

previously reported best thermoelectric performance.

The difficulties found in measuring these properties could be reduced in the future by using additional techniques. The lack of reliability in the resistivity measurements could be due to an insulating surface layer, where de-intercalation by exposure to the atmosphere has changed the surface composition to the insulating $x = 0.5$ phase. By depositing gold contacts onto a freshly cleaved surface and attaching the resistivity leads to these, better measurements could be made. The use of smaller, pre-screened samples would also ensure the best quality crystals, although smaller samples will make thermal conductivity measurements less reliable. This would constitute a substantial research program outside the scope of this thesis.

6.4.2 Magnetic properties

Figure 6.9 presents the magnetisation measurements for single crystal samples of $Na_{0.8}CoO_2$, $Na_{0.7}Ca_{0.1}CoO_2$ and $Na_{0.7}Sr_{0.1}CoO_2$ for field directions parallel and perpendicular to the c-direction. Antiferromagnetic ordering occurs below a temperature $T_N \approx 22K$ for $Na_{0.8}CoO_2$ and $Na_{0.7}Sr_{0.1}CoO_2$ and $T_N \approx 26K$ for $Na_{0.7}Ca_{0.1}CoO_2$. In each case there is an indication of paramagnetic impurities that leads to a sharp increase in magnetisation below $T \approx 10K$. For the pure compound there are no further transitions at lower temperature, and the data resemble those reported previously for $Na_{0.82}CoO_2$ [97]. For the calcium doped sample the out-of-plane data suggest a further transition at $T \approx 20K$, and the in-plane data for the strontium doped sample indicates another transition below $T \approx 16K$.

The hysteresis loops for each of these samples obtained at $T \approx 2K$ confirm the antiferromagnetic nature of the magnetic interaction, see figure 6.10. No further magnetic phase transitions are found at this temperature up to a maximum field $B \approx 7T$.

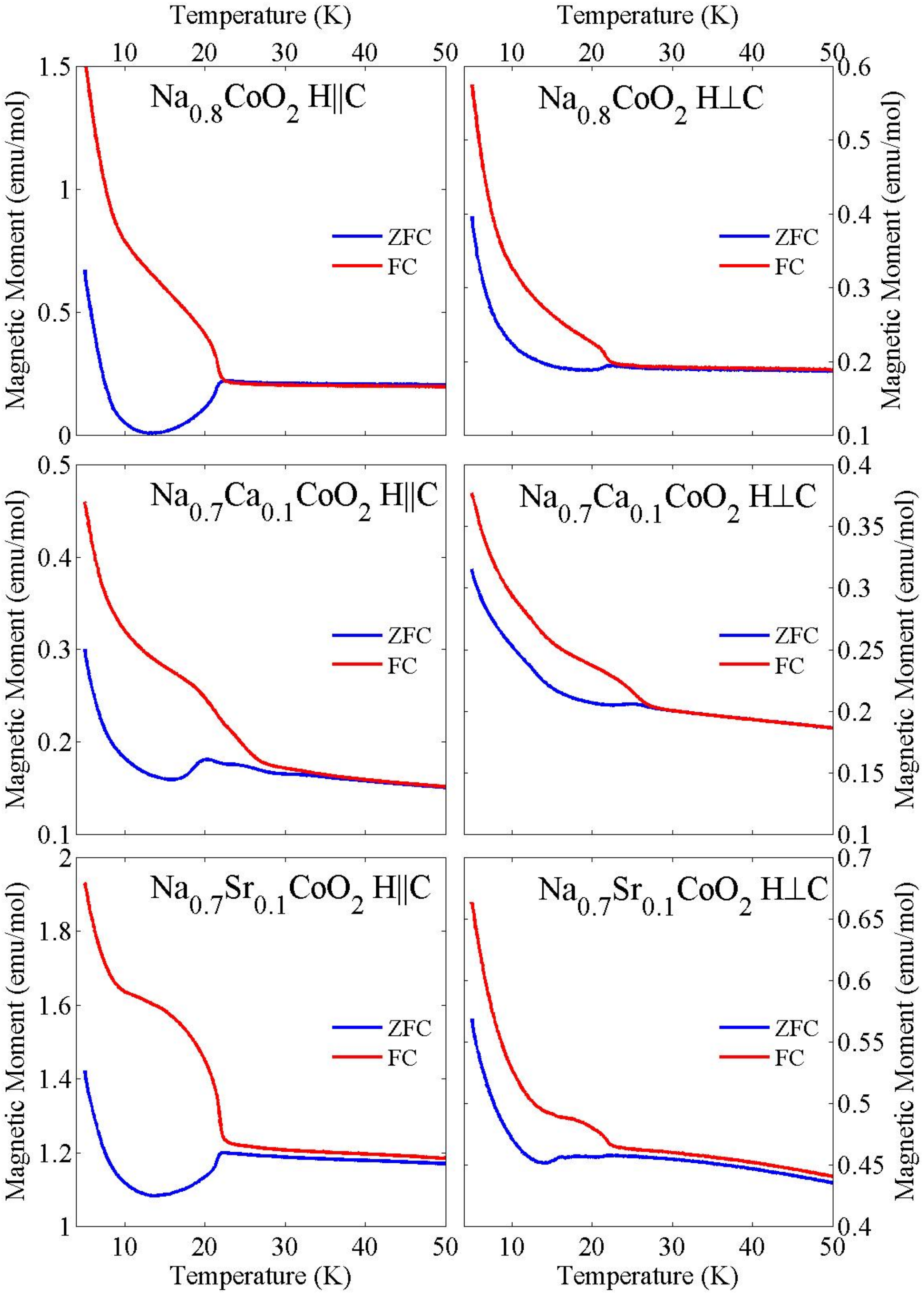

Figure 6.9: Magnetic moments of three samples, each measured with c-axis parallel and perpendicular to the field H. Each sample is measured after cooling without applied field (ZFC) and with applied field (FC).

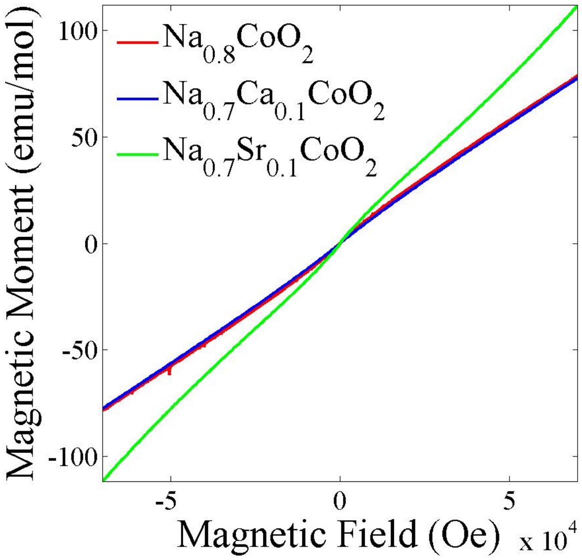

Figure 6.10: Magnetic moments of three samples with varying external magnetic field, each measured with c-axis perpendicular to the field.

The inverse susceptibility data for each sample is plotted as a function of temperature in figure 6.11. The high temperature data are clearly non-linear in each case and, therefore, it is not possible to estimate magnetic moments or the Curie-Weiss temperature using the Curie-Weiss law. Non-linear behaviour was also reported by Carretta *et al.* for $Na_{0.75}CoO_2$, who proposed that metallic regions exhibiting non-Fermi liquid behaviour lead to a linear relationship between inverse susceptibility and T^{α}, where $\alpha = 0.7$ over a range of compositions at high x [75]. Attempts to obtain straight line fits did not reproduce the data for a range of values of α.

In summary, doping with divalent ions clearly changes the magnetic properties of this system. Magnetic properties measurements are an indirect measurement of the electronic structure of this system and the link between the magnetic and electronic structure will likely explain the observed changes in thermoelectric properties. Indeed, the Seebeck coefficient in the pure and strontium doped samples shows a dip at the magnetic transition temperature, clearly demonstrating the importance

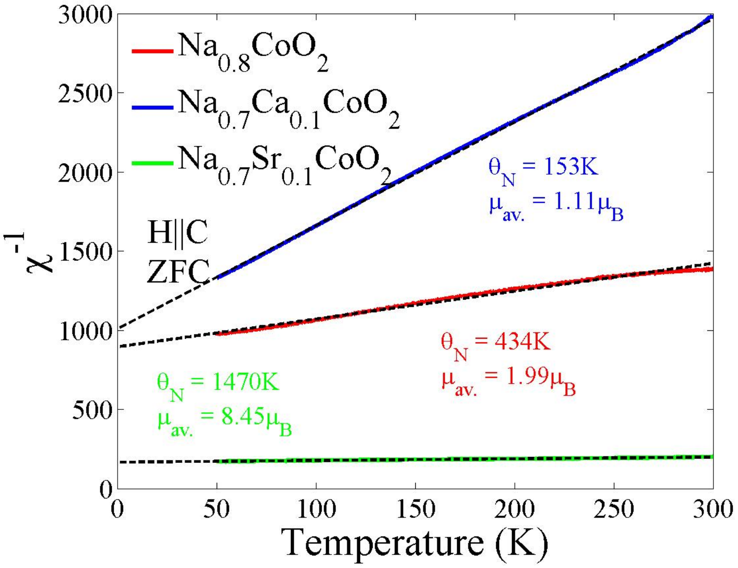

Figure 6.11: Inverse-susceptibility data for the three samples. Dotted lines represent the linear fits to the data, which can be used to determine the Néel temperature, θ_N, and the average magnetic moment, $\mu_{av.}$ using the methods described in ref. [101]. At this scale the fit looks reasonable however close inspection of each lines shows deviations from linearity, which explains why the Néel temperatures determined for these fits fall so far from the observed magnetic ordering temperatures (around 22K).

of this link. There are also additional complexities arising as a result of doping, as additional transitions are observed that could be a result of additional magnetic ordering. Strongly correlated behaviour will often change the linear dependence of the high temperature inverse susceptibility, and this has been observed here in all three systems.

6.4.3 Magnetic Structure

In the first attempt to study $Na_{0.8}CoO_2$ we aligned the sample in CRYOPAD at room temperature and measured superlattice reflections in the horizontal scattering plane. While cooling the sample slowly (at the normal rate for CRYOPAD on IN20) we found that the $(0.8, 0, 0)$ reflection from the stripe phase almost disappeared by $T \approx 220K$. It was not possible to recover a large fraction of the intensity by heating to room temperature. Furthermore, with access to only the $(h0l)$ scattering plane it was not possible to measure superlattice reflections from some of the other possible superstructures of pure Sodium Cobaltate. We therefore aligned another large single crystal of $Na_{0.8}CoO_2$ on IN3, noting the ratio of superlattice peak to Bragg reflection. We found that by quenching the sample directly to $T \approx 200K$ in CRYOPAD it was possible to preserve a large fraction of the intensity in the superlattice reflections.

The polarisation matrices were measured for several reflections in the $(h0l)$ plane at $T \approx 2K$, and typical data is listed in tables 6.1 for the (100), (001), (101) and $(0.8, 0, 1)$ reflections. The magnetic cross sections are given in section 2.2.2.

	T = 2K				T = 30K
Channel	(100)	(001)	$(0.8, 0, 1)$	(101)	(101)
$M_\perp^*.M_\perp$	0.4(3)	0.0(2)	0.00(8)	2.9(1)	1.7(1)
$M_\perp^{y*}.M_\perp^y$	0.00(6)	0.00(3)	0.00(1)	1.84(6)	0.68(6)
$M_\perp^{z*}.M_\perp^z$	0.47(6)	0.04(3)	0.002(7)	1.06(7)	0.99(6)
$i\hat{x}(M_\perp^* \times M_\perp)$	-	-	-	-2.91(9)	-3.03(8)
$N^* \cdot M_\perp^y + N \cdot M_\perp^{y*}$	-	-	-	0.9(1)	0.8(1)
$N^* \cdot M_\perp^z + N \cdot M_\perp^{z*}$	-	-	-	-0.2(1)	-0.1(1)

Table 6.1: Diagonal cross sections from CRYOPAD measurements. Cross sections are normalised by the counting time at each reflection.

Magnetic scattering is detected for moments perpendicular to $\underset{\sim}{\mathbf{Q}}$ for the (101) reflection. However, no signal is detected at the (100) or (001) reciprocal lattice points of the hexagonal lattice, or the superlattice reflection $(0.8, 0, 1)$. Some signal is apparent in the off-diagonal channels, however this does not change above the magnetic transition temperature.

Figure 6.12 shows a scan of Q through the (101) reflection at $T \approx 2K$. All of these plots are peaked in Q, as expected for magnetic Bragg peaks. However, the scattering intensities are very weak and there is possibly leakage of the strong structural scattering in other channels. It is instructive to examine the temperature dependence of these cross sections. Figure 6.13 shows the temperature dependence of magnetic cross sections for the (101) reflection. Over the temperature range 2-30K the cross section perpendicular to the scattering plane is independent of temperature. In contrast, the in-plane cross section has a similar order parameter to that of $Na_{0.82}CoO_2$ in figure 6.4. The fact that all of the magnetic scattering corresponds to components in the horizontal scattering plane, and the lack of magnetic signal at (001) or (100) is consistent with A-type antiferromagnetism with ferromagnetic sheets in the cobalt-oxide layers and moments pointing along the c-direction with opposite senses in successive layers. The magnitude of the moment in the c-direction is estimated to be about $0.16\mu_B$ at base temperature, this is consistent with the value of $0.13\mu_B$ obtained by Bayrakci *et al.* [8] but much smaller than the average magnetic moment determined from straight line fits to the inverse susceptibility, further emphasising the poor agreement of those fits due to a lack of linearity.

Figure 6.14 compares spin-flip with non spin-flip intensity for a polarisation direction parallel to $\underline{\mathbf{Q}}$ for a scan of Q through the superlattice reflection $(0.8, 0, 1)$ at $T = 2K$. The non spin-flip scattering is peaked in Q and this arises from structural scattering from the superstructure. The fact that the spin-flip scattering is flat, as well as the magnetic cross section above, suggests that there is no magnetic scattering within experimental error.

On the basis of the ordered stripe phase superstructure, it is possible to postulate models of the spin density in the cobalt layers. The models illustrated in figure 6.15 locate the magnetic spin-half Co^{4+} ions at either the minima of the Coulomb landscape proposed for this model [50], or at the position of greatest charge from FDMNES calculations in chapter 5. Table 6.2 shows that the magnetic superlattice peak intensity for these models are similar to the hexagonal Bragg peaks, indicating that our measurements should have been sensitive to these magnetic modulations.

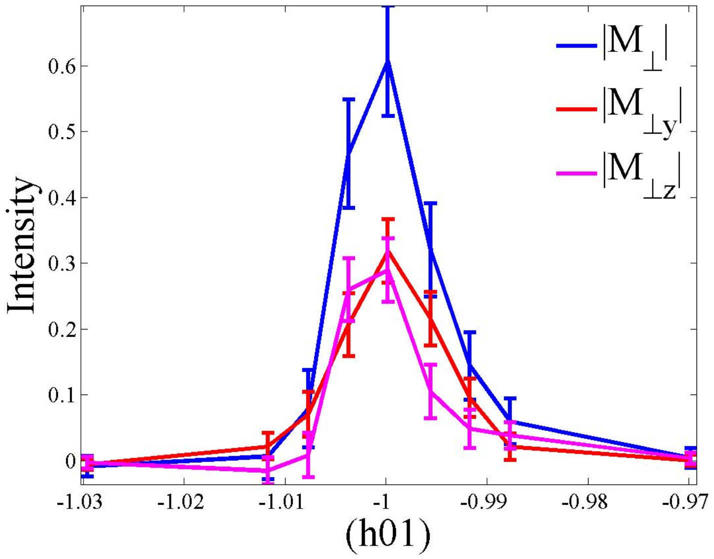

Figure 6.12: Scans though $(h01)$ of the magnetic components, showing a clear magnetic signal above the background. $|M_{\perp y}|$ gives the magnetic component in the $(h0l)$ plane and $|M_{\perp z}|$ gives the component perpendicular to this plane. $|M_{\perp}|$ is a combination of these components.

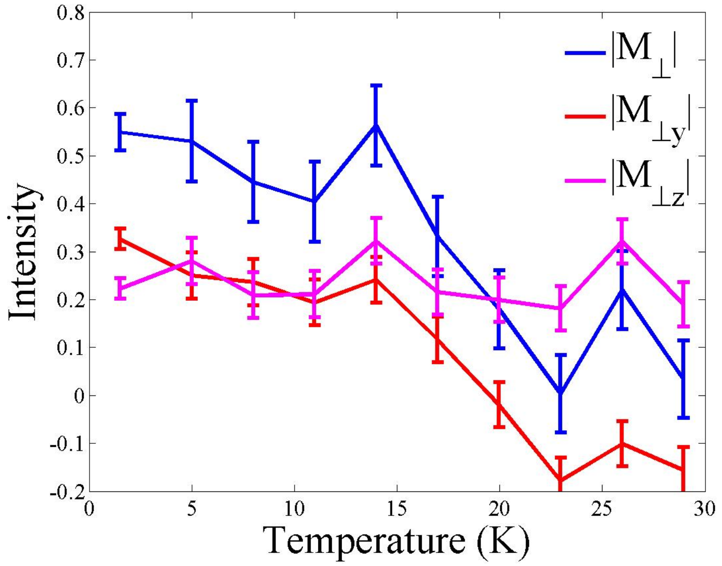

Figure 6.13: Temperature dependence of the magnetic (101) peak. The magnetic component in the $(h0l)$ plane disappears at $T \approx 22K$.

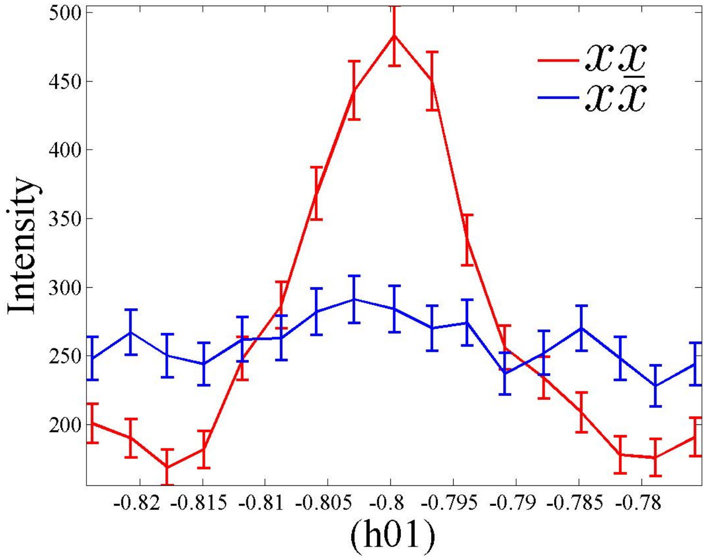

Figure 6.14: Q scans of the $(0.8, 0, 1)$ superlattice reflection. The non-spin-flip (xx) channel shows a structural peak at this position but the spin-flip $(x\bar{x})$ channel shows no evidence of magnetic scattering.

	I(101)	I(0.8,0,1)	I(0.8,0,1)/I(101)
Model (a)	15.85	15.90	1.00
Model (b)	15.85	10.41	0.66

Table 6.2: Calculated magnetic intensities for postulated magnetic structures in figure 6.15.

We can therefore rule out the magnetic modulations of there models, where Co^{4+} ions are localised in specific positions. The results found in chapter 5 indicate that the modulation of valence in the cobalt plane does not lead to such a stark contrast of Co^{3+}/Co^{4+} ordering as modelled above, indeed the change in valence is much smaller and varies in a smoother fashion. This type of modulation will lead to a smearing of intensity, lowering the superlattice peak intensity with respect to the hexagonal peak. Such modulations, given the weak nature of the magnetic scattering and requirement of polarisation analysis, are likely to be difficult to observe with this technique due to the long counting times required. However, if model (b) is correct,

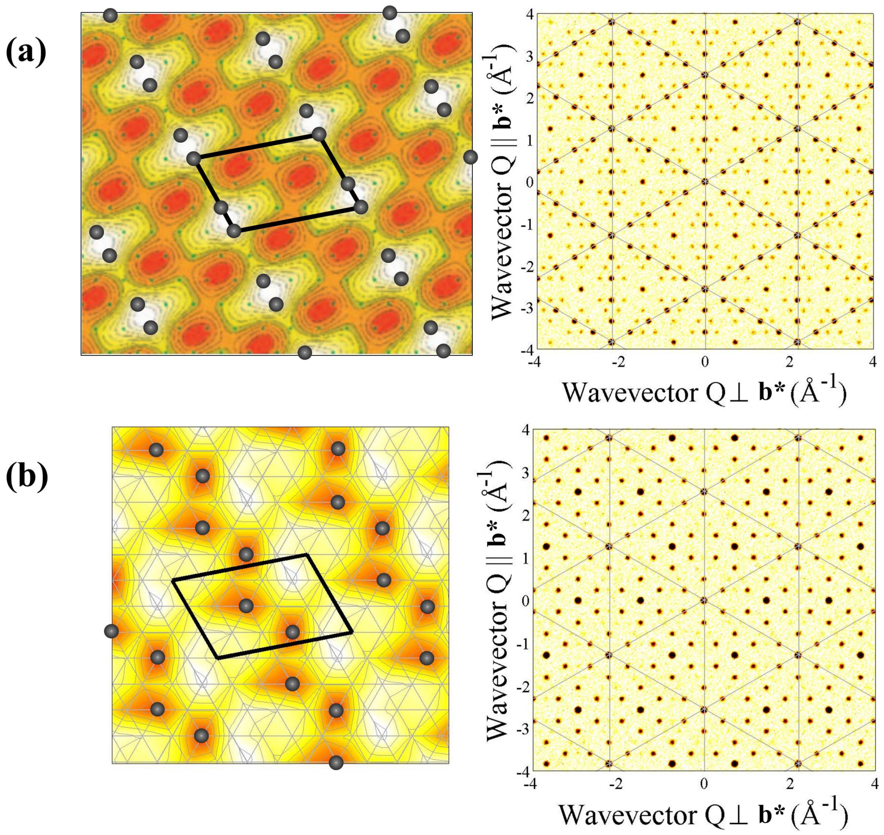

Figure 6.15: Postulated modulation of spin density in the cobalt planes with a magnetic intensity calculation of the $(hk1)$ plane. Black balls show the position of magnetic spin-half Co^{4+} ions, all other positions are non-magnetic Co^{3+} ions. **(a)** Spins are localised at the minima of the Coulomb landscape from ref. [50]. **(b)** Spins are located at the positions of highest charge in the predicted charge layer from FDMNES, see chapter 5. Both models predict magnetic intensity at the $(0.8, 0, 1)$ position with a similar intensity to the (101) position.

it would be more promising to search for magnetic scattering at $(\frac{1}{3}, \frac{1}{3}, 1)$ since this is a stronger magnetic reflections and the structural background is smaller.

Doping with calcium or strontium leads to changes in the magnetic properties of these systems, and these will be caused by changes in the magnetic structure. Using the superstructures proposed in chapter 4, it will be possible to perform further polarised neutron measurements on these doped samples and measure their magnetic structures.

6.5 Conclusions

The electrical and thermal transport measurements for $Na_{0.8}CoO_2$, $Na_{0.57}Ca_{0.14}CoO_2$ and $Na_{0.7}Sr_{0.1}CoO_2$ demonstrate their potential as useful thermoelectric materials, with high Seebeck coefficients of around or greater than $100\mu V/K$. The trend in thermoelectric performance is different to that previously published, possibly due to the dependence on the precise superstructure. The results in this chapter establish links between the details of the superstructure and the thermoelectric properties. For example, $Na_{0.8}CoO_2$ has a very high Seebeck coefficient. The stripe phase was shown to lead to the channelling of holes along one-dimensional path ways in the CoO_2 layers in chapter 5. Such a confinement of holes is expected to lead to strong correlations and, according to the arguments outlined in chapter 1, this gives a natural explanation for the high value of S. It is striking that for both samples with stripe phases, $Na_{0.8}CoO_2$ and $Na_{0.7}Sr_{0.1}CoO_2$, S drops dramatically to zero at the Néel temperature. The thermal conductivity of $Na_{0.57}Ca_{0.14}CoO_2$ is exceptionally high. Since this sample has the ideal composition for its superstructure, it highlights the role of defects in reducing the thermal conductivity.

The magnetic ordering in the $Na_{0.8}CoO_2$ sample was found to be an A-type antiferromagnet with moments pointing along the c-direction in opposite senses in successive planes. We were unable to detect any magnetic modulation within the plane, within experimental uncertainty. Magnetic susceptibility measurements showed that none of the samples obeyed the Curie-Weiss law, as expected for these strongly correlated systems. Additional magnetic phase transitions were identified for the doped compounds.

Chapter 7

Summary & Conclusions

Sodium Cobaltate is a material of enormous interest both scientifically and technologically, as understanding the fundamental physics behind this material could lead to significant advances in environmentally friendly technology. Increasing the number of electronic holes in the material leads to improvements in the thermoelectric properties and these holes can be increased by decreasing the sodium concentration. Above a certain concentration, however, the thermoelectricity decreases due to the coexistence of insulating phases. The number of holes can be increased by doping with di-valent ions such as calcium or strontium, and these have been reported to increase the system's thermoelectric properties further.

As the concentration of sodium varies, a kaleidoscope of diffraction patterns emerges as the superstructure of sodium ions changes. The ordering of sodium patterns the Coulomb landscape in the cobalt-oxygen layers, where the depth of potential wells is greater than the electron hopping energy. NMR studies have revealed a number of distinct valences for cobalt, although no spacial technique has previously been used to asses the ordering of these valences.

Neutron and x-ray diffraction has been combined with resonant x-ray and magnetic measurement techniques to study single crystals of Na_xCoO_2, $Na_xCa_yCoO_2$

and $Na_xSr_yCoO_2$, allowing us to study the atomic, electronic and magnetic structures in these systems.

7.1 Crystal Structures

Single crystal diffraction was performed using neutrons on SXD at ISIS and with x-rays at Royal Holloway. Samples of $Na_{0.8}CoO_2$, $Na_xCa_yCoO_2$ and $Na_xSr_yCoO_2$ all exhibited new diffraction patterns, owing to superstructures in the sodium-dopant layers. Refinement techniques, Reverse Monte Carlo (RMC) and some manual simulations were used to determine the long range ordering of sodium and dopant ions within these materials. The combination of RMC and simulated annealing was found to perform well on these systems, providing structural models that could accurately generate the observed diffraction pattern and be reliably reproduced irrespective of the initial sodium configuration. Providing the experimental data was adequate, the code was able to provide the ordering of not just the sodium and dopant ions, but also the cobalt and oxygen distortions. Experimental and calculated diffraction data are illustrated with the ordering patterns in figure 7.1.

The superlattice formed in $Na_{0.8}CoO_2$ at low temperature was explained by an ordering of tri-vacancy clusters, arranged in 1D stripes, where the relationship between successive stripes is fixed. At high temperature, the relationship between successive stripes becomes random, and this leads to a smearing effect on off-axis superlattice peaks. RMC showed that the cobalt-oxygen layer contains distortions that follow to sodium pattern, and are equivalent to the buckling predicted from the Coulomb landscape.

Doping Sodium Cobaltate with calcium leads to a single dominant phase throughout the temperature and composition range. The RMC code was able to determine the superstructure, which consisted of di-vacancy clusters in the sodium-calcium

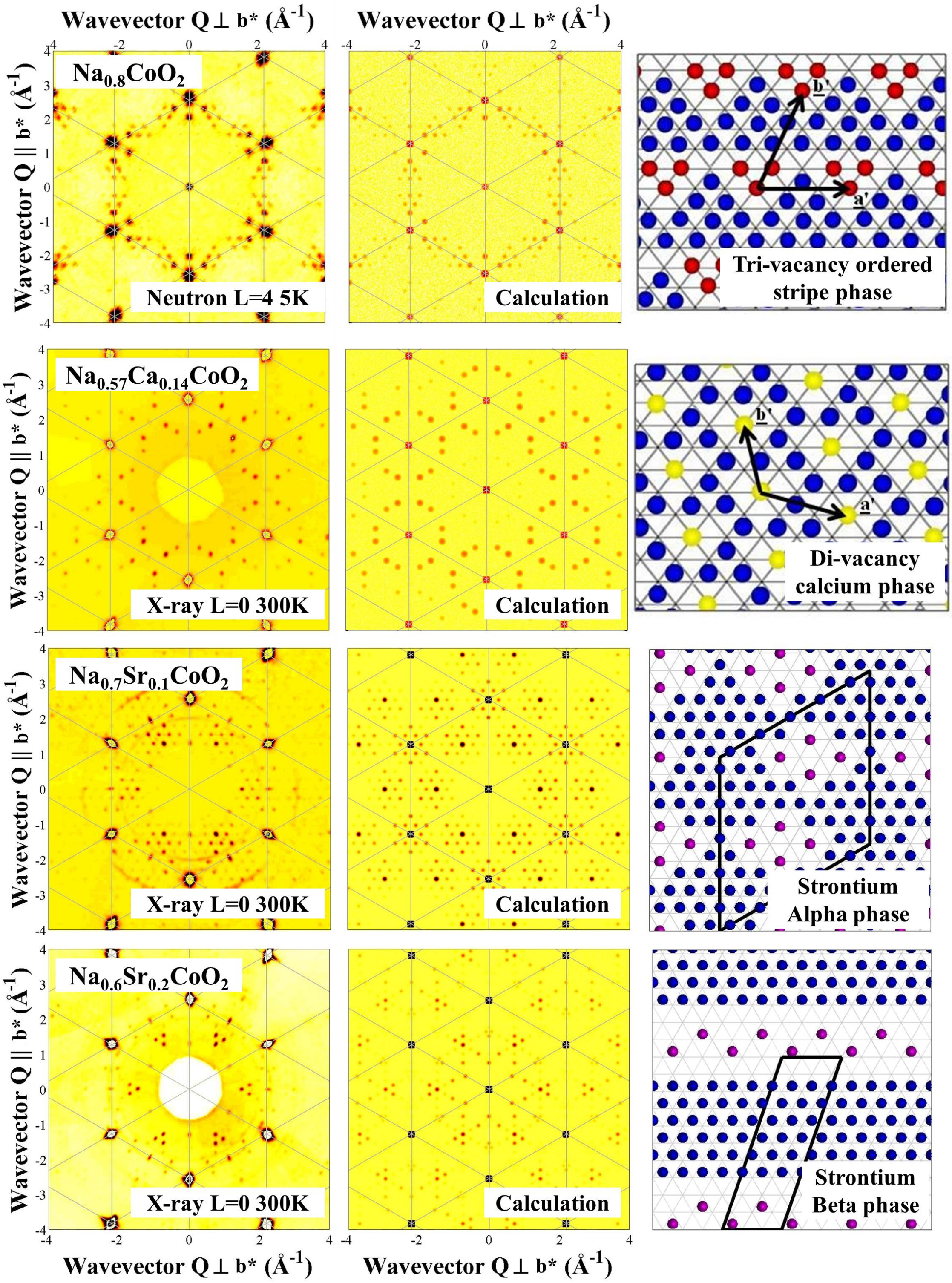

Figure 7.1: Diffraction patterns observed and structural solutions.

layer, where calcium ions sit at the central di-vacancy site. Distortions in the cobalt-oxygen layer were also observed, though these were much smaller than in the pure system. Increasing the concentration of calcium lead to a coexistence with the insulating $Na_{0.5}CoO_2$ phase, explaining the reduction in thermoelectric properties observed at higher concentrations.

X-ray diffraction of $Na_xSr_yCoO_2$ revealed two separate diffraction patterns, both significantly more complex than previous systems due to their satellite peak intensities appearing away from the principle hexagonal reflections. A combination of RMC and manual modelling was used to determine the superstructures for both systems. The alpha phase, observed in $Na_{0.7}Sr_{0.1}CoO_2$, consisted of a large supercell, where each sodium-strontium layer comprised of two multi-vacancy clusters with four strontium ions sitting on Na1 sites. The beta phase, observed in $Na_{0.6}Sr_{0.2}CoO_2$, was explained by stripes of separated strontium ions sitting on Na2 sites, surrounded by vacancies, where each strontium stripe is separated by regions of closely packed sodium ions.

7.2 Electronic Ordering

Resonant x-ray scattering was performed on I16 at Diamond using samples of $Na_{0.8}CoO_2$ and $Na_{0.7}Ca_{0.1}CoO_2$. Resonant behaviour was observed in both systems in the rotated polarisation channel. Energy, azimuthal and spatial scans were combined with temperature and polarisation dependences to measure the attributes of the resonances. The first-principles calculation FDMNES was used to model the resonant behaviour of these systems and was able to produce qualitative agreement with the experimental data.

The electronic ordering proposed by FDMNES consisted of an ordering of valences in the cobalt-oxygen layers that clearly follows the ordering of ions in the sodium layer. The largest distortions in valence however were not found in the cobalt ions, as expected, but in the surrounding oxygen ions.

7.3 Physical Properties

Thermal transport measurements were performed on $Na_{0.8}CoO_2$, $Na_{0.57}Ca_{0.14}CoO_2$ and $Na_{0.7}Sr_{0.1}CoO_2$. All three samples exhibited excellent thermoelectric behaviour with higher Seebeck coefficients compared to competing bulk thermoelectric materials that do not contain toxic or sparse ingredients. The link between their thermoelectric properties and superstructure has also been established for the first time. The change in thermoelectric properties between the different systems was different to that previously observed, however structural differences are likely to be the cause of this. The excellent thermoelectric performance of $Na_{0.8}CoO_2$ can be attributed to its ideal structure, due to confinement of electrons in the 1D conduction pathways caused by stripe ordering of sodium ions and the phonon suppression from rattling cage ions in tri-vacancy clusters. The high thermal conductivity in $Na_{0.57}Ca_{0.14}CoO_2$ demonstrated the importance of thermal conductivity in thermoelectric materials, as this had a detrimental effect on the thermoelectric figure of merit.

Magnetic properties measurements were performed using a SQUID VSM at Diamond on single crystal samples of $Na_{0.8}CoO_2$, $Na_{0.7}Ca_{0.1}CoO_2$ and $Na_{0.7}Sr_{0.1}CoO_2$. The antiferromagnetic transition temperature was determined for all three compounds, and additional unexplained transitions were observed in the calcium and strontium doped systems. These measurements demonstrate the change in magnetic and electronic structure in this system when doped with divalent ions.

Magnetic scattering experiments were performed on crystals of $Na_{0.8}CoO_2$ using neutrons on IN20 at ILL. The antiferromagnetic transition was observed at the principal hexagonal reflections with polarised neutrons, however we were not able to observe any satellite peaks from magnetic modulations in the cobalt layer.

7.4 Final Conclusion

The superstructures of $Na_{0.8}CoO_2$, $Na_xCa_yCoO_2$ and $Na_xSr_yCoO_2$ have been solved and the relationship with their thermoelectric properties has been determined. The effect of ordering in the sodium-dopant layer has been clearly observed in the distortions found in the cobalt-oxygen layer using RMC.

The electronic and magnetic structure measurements lead us to an important discovery about the nature of charge ordering within Sodium Cobaltate, as resonant x-ray experiments and modelling have determined that the largest distortions in charge are found in ordered stripes within the oxygen layers. This result has been backed up by magnetic scattering measurements that were not able to observe any long range magnetic ordering from Co^{4+} ions.

Further investigation into these materials is absolutely essential. The charge ordering in the system can be further measured with more in-depth resonant x-ray studies, allowing greater constraints on the FDMNES model. It would also be worth calculating the electronic structure with other codes that include periodic boundary conditions, as this may lead to a better understanding of the locations of charges in the system. Doping with other ions such as trivalent lanthanum may lead to new superlattice patterns and may provide further enhancement to the thermopower. The materials studied here can also be developed further by growing thin films rather than single crystals, which can lead to a significant increase in the thermoelectric properties.

Bibliography

[1] J. G. Bednorz and K. A. Müller, Zeitschrift fur Physik B Condensed Matter **64**, 189 (1986).

[2] W. Eerenstein, N. D. Mathur, and J. F. Scott, Nature **442**, 759 (2006).

[3] R. J. Zeches *et al.*, Science **326**, 977 (2009).

[4] V. V. Nikita, Physics-Uspekhi **55**, 250 (2012).

[5] K. Takada *et al.*, Nature **422**, 53 (2003).

[6] M. L. Foo *et al.*, Phys. Rev. Lett. **92**, 247001 (2004).

[7] M. Lee *et al.*, Nat. Mater. **5**, 537 (2006).

[8] S. P. Bayrakci *et al.*, Phys. Rev. Lett. **94**, 157205 (2005).

[9] J. O. Haerter, M. R. Peterson, and B. S. Shastry, Phys.Rev.Lett. **97**, 226402 (2006).

[10] J. Wooldridge, Superconductivity and magnetism in sodium cobaltate oxyhydrate, 2006, Ph.D. thesis, University of Warwick.

[11] I. Terasaki, Phys. Rev. B **56**, 12685 (1997).

[12] M. Roger, private communication.

[13] J. M. Ziman, *Electrons and Phonons: The Theory of Transport Phenomena in Solids* (Oxford University Press, 2001).

[14] J. R. Hook and H. E. Hall, *Solid State Physics*, 2nd ed. (Wiley, Chichester, 1991).

[15] H. M. Rosenberg, *The solid state: an introduction to the physics of crystals for students of physics, materials science, and engineering*, 2nd ed. (Clarendon Press, Oxford, 1978).

[16] *International Tables for Crystallography* Vol. A, 5th ed. (Springer, 2005).

[17] G. Burns and A. M. Glazer, *Space groups for solid state scientists* (London:Academic Press, New York, 1978).

[18] R. M. Martin, *Electronic Structure: Basic Theory and Practical Methods* (Cambridge University Press, 2004), 2009285532.

[19] J. Singleton, *Band Theory and Electronic Properties of Solids* (Oxford University Press, USA, 2001), 20010328.

[20] I. R. Mukhamedshin, H. Alloul, G. Collin, and N. Blanchard, Phys. Rev. Lett. **94**, 247602 (2005).

[21] W. Friedrich, P. Knipping, and M. von Laue, Sitzungsberichte der Mathematisch-Physikalischen Classe der Kniglich-Bayerischen Akademie der Wissenschaften zu München , 303 (1912).

[22] W. H. Bragg and W. L. Bragg, Proceedings of the Royal Society of London.Series A **88**, pp. 428 (1913).

[23] J. Als-Nielsen and D. McMorrow, *Elements of Modern X-Ray Physics* (John Wiley, 2011).

[24] G. L. Squires, *Introduction to the Theory of Thermal Neutron Scattering* (Cambridge University Press, 1997).

[25] T. Janssen, A. Janner, A. Looijenga-Vos, and P. M. D. Wolff, *Incommensurate and commensurate modulated structures*, International tables for Crystallography Vol. C, 3rd ed. (, 2006), chap. 9.8, pp. 907–955.

[26] A. J. Blake, W. Clegg, and J. M. Cole, *Crystal structure analysis: principles and practice* (Oxford University Press, 2009), 2009011644.

[27] M. J. Gutmann, Sxd2001 user's guide, 2004.

[28] Neutron scattering lengths and cross sections, `http://www.ncnr.nist.gov/resources/n-lengths/`, Accessed 1 October 2008.

[29] F. Tasset *et al.*, Physica B: Condensed Matter **267268**, 69 (1999).

[30] O. Schärpf and H. Capellmann, Physica Status Solidi (a) **135**, 359 (1993).

[31] M. Blume, Phys. Rev. **130**, 1670 (1963).

[32] How isis works, `http://www.isis.stfc.ac.uk/about-isis/how-isis-works---in-depth4371.html`, Accessed 1 March 2012.

[33] Ill reactor characteristics, `http://www.ill.eu/reactor-environment-safety/high-flux-reactor/technical-characteristics/`, Accessed 1 March 2012.

[34] D. A. Keen, M. J. Gutmann, and C. C. Wilson, Journal of Applied Crystallography **39**, 714 (2006).

[35] R. M. Moon, T. Riste, and W. C. Koehler, Phys. Rev. **181**, 920 (1969).

[36] P. J. Brown, J. B. Forsyth, and F. Tasset, Proceedings: Mathematical and Physical Sciences **442**, pp. 147 (1993).

[37] P. J. Brown, T. Chattopadhyay, J. B. Forsyth, and V. Nunez, Journal of Physics: Condensed Matter **3**, 4281 (1991).

[38] P. J. Brown, A. G. Fox, E. N. Maslen, M. A. O'Keefe, and B. T. M. Willis, *Intensity of diffracted intensities*, International tables for Crystallography Vol. C, 3rd ed. (, 2006), chap. 6.1, pp. 554–595.

[39] D. H. Templeton and L. K. Templeton, Acta Crystallographica Section A **38**, 62 (1982).

[40] Y. Murakami *et al.*, Phys. Rev. Lett. **81**, 582 (1998).

[41] K. Namikawa, M. Ando, T. Nakajima, and H. Kawata, Journal of the Physical Society of Japan **54**, 4099 (1985).

[42] D. Gibbs *et al.*, Phys. Rev. Lett. **61**, 1241 (1988).

[43] J. P. Hill and D. F. McMorrow, Acta Crystallographica Section A **52**, 236 (1996).

[44] U. Staub *et al.*, Phys. Rev. Lett. **88**, 126402 (2002).

[45] L. Paolasini *et al.*, Phys. Rev. Lett. **90**, 057201 (2003).

[46] S. P. Collins *et al.*, AIP Conference Proceedings **1234**, 303 (2010).

[47] D. Prabhakaran, A. T. Boothroyd, R. Coldea, and N. R. Charnley, Journal of Crystal Growth **271**, 74 (2004).

[48] R. L. McGreevy, Journal of Physics: Condensed Matter **13**, R877 (2001).

[49] D. A. Keen and R. L. McGreevy, Nature **344**, 423 (1990).

[50] D. J. P. Morris *et al.*, Phys. Rev. B **79**, 100103 (2009).

[51] R. L. McGreevy and L. Pusztai, Molecular Simulation **1**, 359 (1988).

[52] J. R. Stewart and R. Cywinski, Journal of Physics: Condensed Matter **21**, 124216 (2009).

[53] R. L. McGreevy and P. Zetterstrm, Current Opinion in Solid State and Materials Science **7**, 41 (2003).

[54] R. Evans, Molecular Simulation **4**, 409 (1990).

[55] R. L. McGreevy and M. A. Howe, Physics and Chemistry of Liquids **24**, 1 (1991).

[56] N. Metropolis, A. W. Rosenbluth, M. N. Rosenbluth, A. H. Teller, and E. Teller, The Journal of Chemical Physics **21**, 1087 (1953).

[57] G. Cowan, *Statistical Data Analysis* (Oxford University Press, USA, 1998), 98014554.

[58] Y. Joly, Phys. Rev. B **63**, 125120 (2001).

[59] Fdmnes home page, `http://neel.cnrs.fr/spip.php?rubrique1007&lang=en`, Accessed 16 May 2012.

[60] L. H. Thomas, Mathematical Proceedings of the Cambridge Philosophical Society **23**, 542 (1927).

[61] E. Fermi, Rend. Accad. Naz. Lincei **6**, 602 (1927).

[62] P. Hohenberg and W. Kohn, Phys. Rev. **136**, B864 (1964).

[63] W. Kohn and L. J. Sham, Phys. Rev. **140**, A1133 (1965).

[64] Wikipedia, Density functional theory, `http://en.wikipedia.org/w/index.php?title=Density_functional_theory&oldid=491297366`, Accessed 16 May 2012.

[65] J. Kohanoff, *Electronic Structure Calculations For Solids And Molecules: Theory And Computational Methods* (Cambridge University Press, 2006).

[66] S. Boseggia *et al.*, eprint arXiv:cond-mat/1201.1452 (2012).

[67] M. Benfatto, Y. Joly, and C. R. Natoli, Phys. Rev. Lett. **83**, 636 (1999).

[68] H. W. Zandbergen, M. Foo, Q. Xu, V. Kumar, and R. J. Cava, Phys. Rev. B **70**, 024101 (2004).

[69] D. J. P. Morris, Sodium ordering and the control of properties in sodium cobaltate, 2007, Ph.D. thesis, University of Liverpool.

[70] M. Roger *et al.*, Nature **445**, 631 (2007).

[71] Q. Huang *et al.*, Journal of Physics: Condensed Matter **16**, 5803 (2004).

[72] F. T. Huang *et al.*, Phys. Rev. B **80**, 144113 (2009).

[73] F. C. Chou *et al.*, Phys. Rev. Lett. **101**, 127404 (2008).

[74] C. de Vaulx *et al.*, Phys. Rev. Lett. **95**, 186405 (2005).

[75] P. Carretta *et al.*, Phys. Rev. B **70**, 024409 (2004).

[76] D. J. P. Morris *et al.*, Journal of Magnetism and Magnetic Materials **310**, 810 (2007).

[77] T. A. Platova, I. R. Mukhamedshin, H. Alloul, A. V. Dooglav, and G. Collin, Phys. Rev. B **80** (2009).

[78] Y. Hinuma, Y. S. Meng, and G. Ceder, Phys. Rev. B **77**, 224111 (2008).

[79] P. Zhang, R. B. Capaz, M. L. Cohen, and S. G. Louie, Phys.Rev.B **71**, 153102 (2005).

[80] J. Geck *et al.*, Phys.Rev.Lett. **97**, 106403 (2006).

[81] T. Kawata, Y. Iguchi, T. Itoh, K. Takahata, and I. Terasaki, Phys. Rev. B **60**, 10584 (1999).

[82] Y. Li, G. Xu, and M. Jiang, Journal of Materials Science and Technology **22**, 526 (2006).

[83] D. Prabhakaran and A. T. Boothroyd, Journal of Crystal Growth **318**, 924 (2011).

[84] R. J. Balsys and R. L. Davis, Refinement of the structure of na0.74coo2 using neutron powder diffraction, 1997.

[85] L. Palatinus and G. Chapuis, Journal of Applied Crystallography **40**, 786 (2007).

[86] M. Dusek, V. Petrícek, M. Wunschel, R. E. Dinnebier, and S. van Smaalen, Journal of Applied Crystallography **34**, 398 (2001).

[87] M. Valkeapää *et al.*, Journal of Solid State Chemistry **180**, 1608 (2007).

[88] D. J. Singh, Phys.Rev.B **61**, 13397 (2000).

[89] F. Rivadulla, J. S. Zhou, and J. B. Goodenough, Phys.Rev.B **68**, 075108 (2003).

[90] N. P. Ong and R. J. Cava, Science **305**, 52 (2004).

[91] H. A. Jahn and E. Teller, Proceedings of the Royal Society of London.Series A, Mathematical and Physical Sciences **161**, pp. 220 (1937).

[92] Y. Uchimoto, H. Sawada, and T. Yao, Journal of Power Sources **97-98**, 326 (2001).

[93] J. Matsuno *et al.*, Phys.Rev.B **60**, 4605 (1999).

[94] J. M. Tranquada, B. J. Sternlieb, J. D. Axe, Y. Nakamura, and S. Uchida, Nature **375**, 561 (1995).

[95] M. Yokoi *et al.*, Journal of the Physical Society of Japan **74**, 3046 (2005).

[96] D. Prabhakaran, A. Boothroyd, R. Coldea, L. Helme, and D. Tennant, eprint arXiv:cond-mat/0312493 (2003).

[97] S. P. Bayrakci *et al.*, Phys. Rev. B **69**, 100410 (2004).

[98] B. C. Sales *et al.*, Phys. Rev. B **70**, 174419 (2004).

[99] A. T. Boothroyd *et al.*, Phys. Rev. Lett. **92**, 197201 (2004).

[100] L. M. Helme *et al.*, Phys. Rev. Lett. **94**, 157206 (2005).

[101] S. Blundell, *Units in electromagnetism,*Magnetism in Condenced Matter (Oxford University Press, 2004), chap. Appendix A, p. 196.

Appendix A

Reverse Monte Carlo Program

```
function thesisRMC
% Reverse Monte Carlo Program with simulated annealing
% For neutron diffraction experiments on Sodium Cobaltate
% Written in MATLAB/Octave code, uses only inbuilt functions.
% Calculation variables are altered at the start of the file.
%
% V4.1
% By Daniel Porter MPhys
% Royal Holloway
% 2012

%--------------------------Define Program Parameters-----------------------
% Experimental data file name + directory
% Data must be in the form: h k l I error
filename = 'filename.dat';

% Basis vectors for superstructure
% THIS MUST BE THE SAME FOR EXPERIMENTAL DATA
% Ordered Stripe Supercell
UV = [ 8.55         0          0;
       4.275       12.341      0;
       0            0         10.8];

% Concentration of Sodium
concNa = 0.7;

% Concentration of Dopant
concDp = 0.1;

% Dopant Neutron Scattering length (fm)
% scatDp = 4.70; % Ca
scatDp = 7.02; % Sr

% Thermal Paramater (0 for off, 1 for on)
UISO = 1;

% Displacement parameters
pmove  = 1; % single displacemet, % of inter—Co distance
pthres = 5; % maximum displacement, % of inter—Co distance
```

```

% Number of Monte−Carlo repetitions
MCrep = 20000;

% Initial Temperature
Binit = 0.00001;

% Number of Temperature loops
Temploop = 200;

% Temperature increase factor, BETA = Tinc*BETA
% Temperature = 0.01*Tinc^n
Tinc = 1.1;


%−−−−−−−−−−−−−−−−−−−−−−−−−Initialise variables−−−−−−−−−−−−−−−−−−−−−−−−−−−−−
% Coordinate systems − Reciprical basis vectors
UVstar = 2*pi*eye(3)/UV';

% Average hexagonal unit cell
HEX = 2.85*[1 0 0; −0.5 sqrt(3)/2 0; 0 0 10.8/2.85];

% Various paramaters
latpar_a = 2.85;
latpar_c = 10.8;
nalay1 = round(100*0.25*latpar_c)/100;
nalay2 = round(100*0.75*latpar_c)/100;

% Scattering lengths
scatNa = 3.63;
scatCo = 2.49;
scatOx = 5.803;

% Difference in Na/Dopant scattering lengths (for Na/dopant switching)
scatdif=scatNa−scatDp;

% Thermal Uiso parameters (A^2)
uCo = 0.003; % Co Isotropic thermal paramater
uOx = 0.005; % O  Isotropic thermal paramater
uNa = 0.015; % Na Isotropic thermal paramater

% Nearest Neighbour Distance
NNdist = 1.66^2; % approx (a/sqrt(3))^2

% Displacement options
move = latpar_a*pmove/100; %A, single displacemet, % of inter−Co distance
thres = latpar_a*pthres/100; %A, maximum displacement, % of inter−Co

% Initail temperature
BETA = Binit;

% Seed − set default
if ~exist('seed','var'), seed = randi(100); end

% Random number generation, sets the starting seed so data can be
% reproduced
if ~nargin, seed=0; end % set default for seed
stream = RandStream('mt19937ar','Seed',seed);
RandStream.setDefaultStream(stream);



```

```
%-----------------------Load Experimental Data-----------------------------
% Load data file
DATA = load(filename);

HKL = DATA(:,1:3);
Iexp = DATA(:,4);
error = DATA(:,5);

% Find Q vectors of these peaks using basis vectors
Q = HKL*UVstar;

% Number of experimental reflections
Npeaks = length(Iexp);

% Normalise the Intensities
normF = sqrt( sum(Iexp.^2)/Npeaks ); % Normalising factor

% Calculate the weights
wi = 1./(error.^2);

%---------------------Generate Symmetrial Domains---------------------------
% Experimental intensities are formed from a single super cell that can
% form upto 12 different domains following the hexagonal symmetry of the
% system. The correct intensity pattern can be calculated by finding the
% equivalent (hkl) indexes for every position in Q and summing over all
% these equivalent positions.

% Symmetry operations
R=[0.5 -0.8660254 0; 0.8660254 0.5 0; 0 0 1]; % Rotation of pi/3
R2=[-0.5 -0.8660254 0; 0.8660254 -0.5 0; 0 0 1]; % Rotation of 2*pi/3

% Generate symetrical versions of unit cell
domUV{1}=UVstar;
domUV{2}=(R*UVstar')';
domUV{3}=(R2*UVstar')';
domUV{4}=[UVstar(:,1) -UVstar(:,2) UVstar(:,3)];
domUV{5}=[UVstar(:,1) -UVstar(:,2) UVstar(:,3)]; domUV{5}=(R*domUV{5}')';
domUV{6}=[UVstar(:,1) -UVstar(:,2) UVstar(:,3)]; domUV{6}=(R2*domUV{6}')';
domUV{7}=[-UVstar(:,1) UVstar(:,2) UVstar(:,3)];
domUV{8}=[-UVstar(:,1) UVstar(:,2) UVstar(:,3)]; domUV{8}=(R*domUV{8}')';
domUV{9}=[-UVstar(:,1) UVstar(:,2) UVstar(:,3)]; domUV{9}=(R2*domUV{9}')';
domUV{10}=[-UVstar(:,1) -UVstar(:,2) UVstar(:,3)];
domUV{11}=[-UVstar(:,1) -UVstar(:,2) UVstar(:,3)]; domUV{11}=(R*domUV{11}')';
domUV{12}=[-UVstar(:,1) -UVstar(:,2) UVstar(:,3)]; domUV{12}=(R2*domUV{12}')';

% Index Q coordinates with the 12 different unit cells
allref=zeros(Npeaks*12,3); isindx=zeros(Npeaks,12);
for n=1:12
    domIDX=(domUV{n}'\Q')'; % index the reflections with current UV
    domHKL=round(domIDX); % round coordinates
    isindx(:,n)=sum(abs(domIDX-domHKL),2)<0.1; % find non-integer indexation
    domHKL(~isindx(:,n),:)=0; % Replace non-integer indexations by 0 position
    allref(((1:Npeaks) + (n-1)*Npeaks),:) = domHKL;
end

% Find the unique reflections
[uniref,NaN,refno] = unique(allref,'rows');
Qcal = uniref*UVstar;

% change shape of refno so that the intensities can be summed along the
% rows later
refno = reshape(refno,size(Q,1),12);
```

```

% Qcal, refno and isindx
% Intensities will be calculated at the positions Qcal and the experimental
% intensity at each Q will be compared to the sum over calculated
% intensities defined by refno. isindx will be used to define 0
% intensities.

%--------------------Generate Initial Model-------------------------
% Fill the cell defined by the basis vectors with an integer number of pure
% nacoo2 unit cells

% Create a lattice of unit cells (15 should be enough for most lattices)
[U,V]=meshgrid(1:15);
UVW = [U(:) V(:) zeros(length(U(:)),1)];
purecells = UVW*HEX;

% index this lattice with the supercell
UVWlat = (UV'\purecells')';

% Determine which lattice points are within the supercell
purecells = UVWlat(UVWlat(:,1) < 1 & UVWlat(:,1) >= 0 & ...
                   UVWlat(:,2) < 1 & UVWlat(:,2) >= 0,:)*UV;

% Define atomic positions in a single unit cell
Co = [0 0 0; 0 0 0.5]*HEX;
Ox = [1/3 2/3 0.0908; 1/3 2/3 0.4092; 2/3 1/3 0.5908; 2/3 1/3 0.9092]*HEX;
Na1= [0 0 0.25; 0 0 0.75]*HEX;
Na2= [2/3 1/3 0.25; 1/3 2/3 0.75]*HEX;

% Fill the supercell with atomic positions
Copos=[]; Oxpos=[]; Na1pos=[]; Na2pos=[];
for P = 1:size(purecells,1)
    Copos(end+1:end+size(Co,1),:) = Co + repmat(purecells(P,:),size(Co,1),1);
    Oxpos(end+1:end+size(Ox,1),:) = Ox + repmat(purecells(P,:),size(Ox,1),1);
    Na1pos(end+1:end+size(Na1,1),:) = Na1 + repmat(purecells(P,:),size(Na1,1),1);
    Na2pos(end+1:end+size(Na2,1),:) = Na2 + repmat(purecells(P,:),size(Na2,1),1);
end

% Number of pure NaCoO2 cells in the supercell
Ncell = size(purecells,1);

% Combine Na2 and Na1 positions
Napos = [Na2pos; Na1pos];

% Define Displacements arrays
CoDpos = zeros(size(Copos));
OxDpos = zeros(size(Oxpos));
NaDpos = zeros(size(Napos));

%----Fill Na/Dopant layers----
type = zeros(size(Napos(:,1)));
% define number of atoms in each layer
Nafill = round(concNa*Ncell);
Dpfill = round(concDp*Ncell);
if Nafill + Dpfill > Ncell, disp('Occupancy too high'); return; end

% layer 1 fill
lay1 = find(abs(Napos(:,3)-nalay1)<0.001); % indexes of positions in layer 1 (Ncell positions)
RR = randperm(Ncell); % only place on Na2 positions
type(lay1(RR(1:Nafill))) = scatNa;
type(lay1(RR(Nafill+1:Nafill+Dpfill))) = scatDp;
% Layer 2 fill
```

```
lay2 = find(abs(Napos(:,3)-nalay2)<0.001); % indexes of positions in layer 2 (Ncell positions)
RR = randperm(Ncell); % only place on Na2 positions
type(lay2(RR(1:Nafill))) = scatNa;
type(lay2(RR(Nafill+1:Nafill+Dpfill))) = scatDp;

% Basis Model:
% Currently defined in several parts for each atom, the positions, the
% scattering lengths and the displacements.
% Co                      Ox                      Na
%   Copos  = [nx3]          Oxpos  = [2nx3]         Napos   = [2nx3]
%   Coscat = [1]            Oxscat = [1]            type    = [2nx3]
%   CoDpos = [nx3]          CoDpos = [2nx3]         NaDpos  = [2nx3]


%--------------------Calculate Initial Intensities-------------------------
% Calculate the atomic isotropic gaussian debye waller factors
Q2 = sum(Qcal.*Qcal,2); % Magnitude of the scattering vector squared
% Debye Waller factor for different elements (assume Na and dopeant are
% same). UISO is either 1 or 0.
DWFCo = exp(-(UISO*uCo*Q2)/2); % Co
DWFOx = exp(-(UISO*uOx*Q2)/2); % O
DWFNa = exp(-(UISO*uNa*Q2)/2); % Na/ Dopant

% Calculate the structure factor from the atomic positions, their
% displacements and their scattering factors.
typesf = repmat(type',size(Qcal,1),1); % prepare array of scattering factors.
DWFCosf = repmat(DWFCo,1,size(Copos,1)); % Prepare array of DWF
DWFOxsf = repmat(DWFOx,1,size(Oxpos,1)); % Prepare array of DWF
DWFNasf = repmat(DWFNa,1,size(Napos,1)); % Prepare array of DWF
% Structure Factor
SF = sum(scatCo*DWFCosf.*exp(1i*Qcal*(Copos+CoDpos)'),2) + ... Cobalts
     sum(scatOx*DWFOxsf.*exp(1i*Qcal*(Oxpos+OxDpos)'),2) + ... Oxygens
     sum(typesf.*DWFNasf.*exp(1i*Qcal*(Napos+NaDpos)'),2); %   Sodium + Dopants

% Calculate Intensity
Ical = SF.*conj(SF);

% Apply domain summation
domI = Ical(refno); % define 12 intensities per position in Q
domI(~isindx)=0;    % Remove non-indexed intensities
Ical = sum(domI,2); % Sum all intensities at each point

 % Normalise Intensity
Ical = normF.*Ical./sqrt(sum(Ical.^2)/Npeaks);

%-------------------------Calculate initial Fit----------------------------
% Calculate and display maximum number of configurations for this system
conf = (nchoosek(Ncell-Dpfill,Nafill)*nchoosek(Ncell,Dpfill))^2;
disp(['Maximum configurations = ' num2str(conf)]);

% Calculate Chi^2 value (without experimental weighting for now...)
CHI = sum( wi.*(Iexp-Ical).^2 );

%------------------------Create Output Files-------------------------------
% Create output file
fid = fopen('output.txt','wt');

% Write introductory data
fprintf(fid,['Reverse Monte Carlo Run, ' datestr(now,0) '\n']);
fprintf(fid,'Experimental data set: %s \n',filename);
fprintf(fid,'Initial Chi^2 = %8.5f \n\n',CHI);

```

```
%----------------------------------------------------------------------------
%---------------------------Start Reverse Monte Carlo------------------------
%----------------------------------------------------------------------------
anneal=0;
for Tn = 1:Temploop
    changes = [0 0];
    BETA = Tinc*BETA; % Reduce the temperature
for MCn = 1:MCrep
    %-----------------------Sodium/Dopant Hopping-----------------------
    % Select a filled and empty site on the same layer
    full = find(type>0); % find filled sites
    fsite = full(randi(length(full))); % select random filled site
    empt = find(Napos(:,3)==Napos(fsite,3) & type == 0); % find empty sites
    esite = empt(randi(length(empt))); % select random empty site
    % fsite is the index of a filled site
    % esite is the index of an empty site

    % check if the selected position is further than the nearest neighbour
    % distance of any other positions. Because the nearest position may be
    % outside the supercell, we generate all positions around the cell.
    fpos = find(Napos(:,3)==Napos(fsite,3) & type>0); % select filled positions
    fpos(fpos==fsite)=[]; % remove current site (allowing move to NN)
    fpos=Napos(fpos,:); % return position coordinates
    a=repmat(UV(1,:),size(fpos,1),1); % repeated versions of basis vectors
    b=repmat(UV(2,:),size(fpos,1),1);
    pos = [fpos; fpos+a; fpos-a; fpos+b; fpos-b; fpos+a+b; fpos+a-b; fpos-a+b; fpos-a-b];

    % Calculate the distance from the empty site to the filled positions
    site = Napos(esite,:);
    mg = (site(1)-pos(:,1)).^2 + (site(2)-pos(:,2)).^2;

    % Only fill the site if the selected site is not within the nearest
    % neighbour distance from another filled position.
    if ~any(mg<=NNdist)
        % Calculate new structure factors
        NSF = SF + type(fsite)*DWFNa.*exp(1i*Qcal*(Napos(esite,:)+NaDpos(fsite,:))') ...
                 - type(fsite)*DWFNa.*exp(1i*Qcal*(Napos(fsite,:)+NaDpos(fsite,:))');
        % Calculate Intensity
        Ical = NSF.*conj(NSF);

        % Apply domain summation
        domI = Ical(refno); % define 12 intensities per position in Q
        domI(~isindx)=0;    % Remove non-indexed intensities
        Ical = sum(domI,2); % Sum all intensities at each point

         % Normalise Intensity
        Ical = normF.*Ical./sqrt(sum(Ical.^2)/Npeaks);

        % Calculate Chi^2 value
        NCHI = sum( wi.*(Iexp-Ical).^2 );

        % Calculate the difference between old and new chi
        DIF = NCHI - CHI;

        %---Metropolis Algorithm---
        accept = 1;
        if DIF>0
            % if new move has a higher chi (worse) than previously, then
            % accept the move with probability P(T)=exp(-DIF/kT). So reject
            % the move if P(T) is less than a random number.
            if exp(-BETA*DIF) < rand, accept=0; end
        end
```

```
        if accept
            % Swap scattering lengths
            type(esite) = type(fsite);
            type(fsite) = 0;
            % Swap displacements (not sure about this)
            NaDpos(esite,:) = NaDpos(fsite,:);
            NaDpos(fsite,:) = [0 0 0];
            % Save the new structure factor and CHI
            SF = NSF;
            CHI = NCHI;
            changes(1) = changes(1) + 1;
        end
    end
    %--------------------------Sodium/Dopant Switching---------------------
    % Select a filled and empty site on the same layer
    sod = find(type==scatNa); % find Na sites
    nsite = sod(randi(length(sod))); % select random Na site
    dop = find(Napos(:,3)==Napos(nsite,3) & type == scatDp); % find dopant sites on same layer
    dsite = dop(randi(length(dop))); % select random dopant site
    % nsite is the index of a Na site
    % dsite is the index of an dopant site on the same layer

    % Try switching the scattering positions
    % Calculate new structure factors
    NSF = SF + scatdif*DWFNa.*exp(1i*Qcal*(Napos(dsite,:)+NaDpos(dsite,:))') ...
             - scatdif*DWFNa.*exp(1i*Qcal*(Napos(nsite,:)+NaDpos(nsite,:))');
    % Calculate Intensity
    Ical = NSF.*conj(NSF);

    % Apply domain summation
    domI = Ical(refno); % define 12 intensities per position in Q
    domI(~isindx)=0;    % Remove non-indexed intensities
    Ical = sum(domI,2); % Sum all intensities at each point

     % Normalise Intensity
    Ical = normF.*Ical./sqrt(sum(Ical.^2)/Npeaks);

    % Calculate Chi^2 value
    NCHI = sum( wi.*(Iexp-Ical).^2 );

    % Calculate the difference between old and new chi
    DIF = NCHI - CHI;

    %---Metropolis Algorithm---
    accept = 1;
    if DIF>0
        % if new move has a higher chi (worse) than previously, then
        % accept the move with probability P(T)=exp(-DIF/kT). So reject
        % the move if P(T) is less than a random number.
        if exp(-BETA*DIF) < rand, accept=0; end
    end
    if accept
        % Swap scattering lengths
        type(nsite) = scatDp;
        type(dsite) = scatNa;
        % Save the new structure factor and CHI
        SF = NSF;
        CHI = NCHI;
        changes(1) = changes(1) + 1;
    end


```

```
%---------------------------Na Displacements----------------------------
% Select two different filled sites on the same layer
atm = find(type>0); % find filled sites
site1 = atm(randi(length(atm))); % select random filled site
% find other filled sites on same layer
atm = find(~(Napos(:,1)==Napos(site1,1) & Napos(:,2)==Napos(site1,2)) ...
           & Napos(:,3)==Napos(site1,3) & type >0);
site2 = atm(randi(length(atm))); % select different random filled site
% site1 is the index of a filled site
% site2 is the index of a different filled site on the same layer

% Generate the displacements
Dx = move*(2*rand-1);
Dy = move*(2*rand-1);
Dz=0; % Displacement only in the plane

% Move the sites by this amount
Dpos1 = [NaDpos(site1,1)+Dx NaDpos(site1,2)+Dy NaDpos(site1,3)+Dz];
Dpos2 = [NaDpos(site2,1)-Dx NaDpos(site2,2)-Dy NaDpos(site2,3)-Dz];

% Only try the moves if the movement is less than the threshold
if norm(Dpos1)<thres && norm(Dpos2)<thres
    % Calculate new structure factors
    NSF = SF - type(site1)*DWFNa.*exp(1i*Qcal*(Napos(site1,:)+NaDpos(site1,:))') ...
             - type(site2)*DWFNa.*exp(1i*Qcal*(Napos(site2,:)+NaDpos(site2,:))') ...
             + type(site1)*DWFNa.*exp(1i*Qcal*(Napos(site1,:)+Dpos1)') ...
             + type(site2)*DWFNa.*exp(1i*Qcal*(Napos(site2,:)+Dpos2)');
    % Calculate Intensity
    Ical = NSF.*conj(NSF);

    % Apply domain summation
    domI = Ical(refno); % define 12 intensities per position in Q
    domI(~isindx)=0;    % Remove non-indexed intensities
    Ical = sum(domI,2); % Sum all intensities at each point

     % Normalise Intensity
    Ical = normF.*Ical./sqrt(sum(Ical.^2)/Npeaks);

    % Calculate Chi^2 value
    NCHI = sum( wi.*(Iexp-Ical).^2 );

    % Calculate the difference between old and new chi
    DIF = NCHI - CHI;

    %---Metropolis Algorithm---
    accept = 1;
    if DIF>0
        % if new move has a higher chi (worse) than previously, then
        % accept the move with probability P(T)=exp(-DIF/kT). So reject
        % the move if P(T) is less than a random number.
        if exp(-BETA*DIF) < rand, accept=0; end
    end
    if accept
        % Change displacements
        NaDpos(site1,:) = Dpos1;
        NaDpos(site2,:) = Dpos2;
        % Save the new structure factor and CHI
        SF = NSF;
        CHI = NCHI;
        changes(2) = changes(2) + 1;
    end
end
```

```
%--------------------------Co Displacements----------------------------
% Select two different sites on the same layer
site1 = randi(length(Copos)); % select random site
% find other sites on same layer
atm = find(~(Copos(:,1)==Copos(site1,1) & Copos(:,2)==Copos(site1,2)) ...
           & Copos(:,3)==Copos(site1,3));
site2 = atm(randi(length(atm))); % select different random site
% site1 is the index of a Co site
% site2 is the index of a different Co site on the same layer

% Generate the displacements
Dx = move*(2*rand-1);
Dy = move*(2*rand-1);
Dz = move*(2*rand-1);

% Move the sites by this amount
Dpos1 = [CoDpos(site1,1)+Dx CoDpos(site1,2)+Dy CoDpos(site1,3)+Dz];
Dpos2 = [CoDpos(site2,1)-Dx CoDpos(site2,2)-Dy CoDpos(site2,3)-Dz];

% Only try the moves if the movement is less than the threshold
if norm(Dpos1)<thres && norm(Dpos2)<thres
    % Calculate new structure factors
    NSF = SF - scatCo*DWFCo.*exp(1i*Qcal*(Copos(site1,:)+CoDpos(site1,:))') ...
             - scatCo*DWFCo.*exp(1i*Qcal*(Copos(site2,:)+CoDpos(site2,:))') ...
             + scatCo*DWFCo.*exp(1i*Qcal*(Copos(site1,:)+Dpos1)') ...
             + scatCo*DWFCo.*exp(1i*Qcal*(Copos(site2,:)+Dpos2)');
    % Calculate Intensity
    Ical = NSF.*conj(NSF);

    % Apply domain summation
    domI = Ical(refno); % define 12 intensities per position in Q
    domI(~isindx)=0;    % Remove non-indexed intensities
    Ical = sum(domI,2); % Sum all intensities at each point

     % Normalise Intensity
    Ical = normF.*Ical./sqrt(sum(Ical.^2)/Npeaks);

    % Calculate Chi^2 value
    NCHI = sum( wi.*(Iexp-Ical).^2 );

    % Calculate the difference between old and new chi
    DIF = NCHI - CHI;

    %---Metropolis Algorithm---
    accept = 1;
    if DIF>0
        % if new move has a higher chi (worse) than previously, then
        % accept the move with probability P(T)=exp(-DIF/kT). So reject
        % the move if P(T) is less than a random number.
        if exp(-BETA*DIF) < rand, accept=0; end
    end
    if accept
        % Change displacements
        CoDpos(site1,:) = Dpos1;
        CoDpos(site2,:) = Dpos2;
        % Save the new structure factor and CHI
        SF = NSF;
        CHI = NCHI;
        changes(2) = changes(2) + 1;
    end
end
```

```
    %--------------------------Ox Displacements----------------------------
    % Select two different sites on the same layer
    site1 = randi(length(Oxpos)); % select random site
    % find other sites on same layer
    atm = find(~(Oxpos(:,1)==Oxpos(site1,1) & Oxpos(:,2)==Oxpos(site1,2)) ...
               & Oxpos(:,3)==Oxpos(site1,3));
    site2 = atm(randi(length(atm))); % select different random site
    % site1 is the index of a Ox site
    % site2 is the index of a different Ox site on the same layer

    % Generate the displacements
    Dx = move*(2*rand-1);
    Dy = move*(2*rand-1);
    Dz = move*(2*rand-1);

    % Move the sites by this amount
    Dpos1 = [OxDpos(site1,1)+Dx OxDpos(site1,2)+Dy OxDpos(site1,3)+Dz];
    Dpos2 = [OxDpos(site2,1)-Dx OxDpos(site2,2)-Dy OxDpos(site2,3)-Dz];

    % Only try the moves if the movement is less than the threshold
    if norm(Dpos1)<thres && norm(Dpos2)<thres
        % Calculate new structure factors
        NSF = SF - scatOx*DWFOx.*exp(1i*Qcal*(Oxpos(site1,:)+OxDpos(site1,:))') ...
                 - scatOx*DWFOx.*exp(1i*Qcal*(Oxpos(site2,:)+OxDpos(site2,:))') ...
                 + scatOx*DWFOx.*exp(1i*Qcal*(Oxpos(site1,:)+Dpos1)') ...
                 + scatOx*DWFOx.*exp(1i*Qcal*(Oxpos(site2,:)+Dpos2)');
        % Calculate Intensity
        Ical = NSF.*conj(NSF);

        % Apply domain summation
        domI = Ical(refno); % define 12 intensities per position in Q
        domI(~isindx)=0;    % Remove non-indexed intensities
        Ical = sum(domI,2); % Sum all intensities at each point

        % Normalise Intensity
        Ical = normF.*Ical./sqrt(sum(Ical.^2)/Npeaks);

        % Calculate Chi^2 value
        NCHI = sum( wi.*(Iexp-Ical).^2 );

        % Calculate the difference between old and new chi
        DIF = NCHI - CHI;

        %---Metropolis Algorithm---
        accept = 1;
        if DIF>0
            % if new move has a higher chi (worse) than previously, then
            % accept the move with probability P(T)=exp(-DIF/kT). So reject
            % the move if P(T) is less than a random number.
            if exp(-BETA*DIF) < rand, accept=0; end
        end
        if accept
            % Change displacements
            OxDpos(site1,:) = Dpos1;
            OxDpos(site2,:) = Dpos2;
            % Save the new structure factor and CHI
            SF = NSF;
            CHI = NCHI;
            changes(2) = changes(2) + 1;
        end
    end
end % End of Monte-Carlo iterations
```

```
% Recalculate the Structure
typesf = repmat(type',size(Qcal,1),1); % prepare array of scatterin factors.
SF = sum(scatCo*DWFCosf.*exp(1i*Qcal*(Copos+CoDpos)'),2) + ... Cobalts
     sum(scatOx*DWFOxsf.*exp(1i*Qcal*(Oxpos+OxDpos)'),2) + ... Oxygens
     sum(typesf.*DWFNasf.*exp(1i*Qcal*(Napos+NaDpos)'),2); %   Sodium + Dopants
Ical = SF.*conj(SF);
domI = Ical(refno); % define 12 intensities per position in Q
domI(~isindx)=0;    % Remove non-indexed intensities
Ical = sum(domI,2); % Sum all intensities at each point
Ical = normF.*Ical./sqrt(sum(Ical.^2)/Npeaks);% Normalise Intensity
% Calculate Chi^2 value
NCHI = sum( wi.*(Iexp-Ical).^2 );


% Save the data at the end of the current temperature
fprintf(fid,'Beta: %4.2E\tCHI^2: %6.3f \tNCHI^2: %6.3f \tChanges: %6.0f %6.0f\n',...
    BETA,CHI,NCHI,changes);

% Check for annealed solution (no changes)
if changes(1)==0 && changes(2)<10, anneal = anneal + 1; end
% If solution is annealed, end the run
if anneal >= 10, break; end
end % End of temperature loop
%--------------------------------------------------------------------------
%----------------------------End Reverse Monte Carlo-----------------------
%--------------------------------------------------------------------------

% Calculate R factor
CHI = sum( wi.*(Iexp-Ical).^2 );
R =  sum( abs(Iexp-Ical) ) / sum( Iexp );
Rw = sqrt( sum( abs(abs(Iexp-Ical).^2 ./error) ) / sum( abs((Iexp.^2)./error) ) );

%----------------------------Write Report----------------------------------
fprintf(fid,'\n-----------Program Finished-----------\n');
fprintf(fid,'Best CHI^2 = %6.6f\n',CHI);
fprintf(fid,'R = %4.2f%% \t Rw = %4.2f%% \n',100*R,100*Rw);
fclose(fid);
```

Appendix B

FDMNES Input File

```
! Fdmnes indata file
! Calculation for the Na0.57Ca0.14CoO2 Divacancy phase

 Filout
  NaCa

 Range          ! Energy range of calculation (eV).
 -19. 0.5 31.   ! 109 steps, same as Diamond

 Radius         ! Radius of the cluster where final state
   7.0          ! calculation is performed

 SCF            ! Self Consistant solution
 Green          ! Muffin tin potential - faster
 R_self         ! Self-consitent radius for SCF
 7.35

 N_self         ! Iterations to get self-consistency
 200

 Delta_E_conv   ! change in energy to get self-consistency
 1

 Rpotmax        ! radius of the cluster for superposition
 7.35

 Quadrupole     ! Quadrupolar transitions modelled
 Density        ! Calculate the density of states about each atom
```

```
! Resonant x-ray scattering at various peaks: h k l sigma pi azimuth.
 rxs
  0 1 8 2 2                   ! (0.143 0.286 8) pi-pi
  0 1 8 2 1                   ! (0.143 0.286 8) pi-sigma
  0 2 8 2 2                   ! (0.286 0.571 8) pi-pi
  0 2 8 2 1                   ! (0.286 0.571 8) pi-sigma
  0 0 9 2 2                   ! (0 0 9) pi-pi
  0 0 9 2 1                   ! (0 0 9) pi-sigma

 Zero_azim                    ! Define basis vector for zero psi angle
 0.36836 0.29469 0.           ! (1 0 0) hexagonal position

 Crystal                      ! Periodic material description (unit cell)
7.5404 7.5404 10.8 90 90 120  ! a, b, c, alpha, beta, gamma
27 0.0000 0.0000 0.0000
27 0.0000 0.0000 0.5000
27 0.1430 0.7140 0.0000
27 0.1430 0.7140 0.5000
27 0.2860 0.4290 0.0000
27 0.2860 0.4290 0.5000
27 0.4290 0.1430 0.0000
27 0.4290 0.1430 0.5000
27 0.5710 0.8570 0.0000
27 0.5710 0.8570 0.5000
27 0.7140 0.5710 0.0000
27 0.7140 0.5710 0.5000
27 0.8570 0.2860 0.0000
27 0.8570 0.2860 0.5000
 8 0.0476 0.2381 0.0908
 8 0.0476 0.2381 0.4092
 8 0.2381 0.1905 0.5908
 8 0.2381 0.1905 0.9092
 8 0.1906 0.9521 0.0908
 8 0.1906 0.9521 0.4092
 8 0.3811 0.9045 0.5908
 8 0.3811 0.9045 0.9092
 8 0.3336 0.6671 0.0908
 8 0.3336 0.6671 0.4092
 8 0.5241 0.6195 0.5908
 8 0.5241 0.6195 0.9092
 8 0.4766 0.3811 0.0908
 8 0.4766 0.3811 0.4092
 8 0.6671 0.3335 0.5908
```

```
 8 0.6671 0.3335 0.9092
 8 0.6186 0.0951 0.0908
 8 0.6186 0.0951 0.4092
 8 0.8091 0.0475 0.5908
 8 0.8091 0.0475 0.9092
 8 0.7616 0.8091 0.0908
 8 0.7616 0.8091 0.4092
 8 0.9521 0.7615 0.5908
 8 0.9521 0.7615 0.9092
 8 0.9046 0.5241 0.0908
 8 0.9046 0.5241 0.4092
 8 0.0951 0.4765 0.5908
 8 0.0951 0.4765 0.9092
11 0.0476 0.2381 0.7500
11 0.2381 0.1905 0.2500
11 0.3811 0.9045 0.2500
11 0.5241 0.6195 0.2500
11 0.4766 0.3811 0.7500
11 0.6186 0.0951 0.7500
11 0.7616 0.8091 0.7500
11 0.9521 0.7615 0.2500
20 0.8571 0.2857 0.2500
20 0.1429 0.7143 0.7500

 Convolution   ! Convolution step

 Scan          ! Azimuthal scans for each Co
NaCa_scan_1.txt
NaCa_scan_2.txt
NaCa_scan_3.txt
NaCa_scan_4.txt
NaCa_scan_5.txt
NaCa_scan_6.txt
NaCa_scan_7.txt

 Scan_conv     ! Convolve azimuthal scans
NaCa_scan_conv.txt

 End
```